Single-Atom Catalysts: Syntheses, Characterization, and Catalytic Evaluation in Selective Oxidation and Hydrogenation Reactions

A Thesis Submitted to the
College of Graduate and Postdoctoral Studies
In Partial Fulfillment of the Requirements
For the Degree of Master
In the Department of Chemistry
University of Saskatchewan
Saskatoon

By

Brandon Chivers

Permission to Use

In presenting this thesis/dissertation in partial fulfillment of the requirements for a Postgraduate degree from the University of Saskatchewan, I agree that the Libraries of this University may make it freely available for inspection. I further agree that permission for copying of this thesis/dissertation in any manner, in whole or in part, for scholarly purposes may be granted by the professor or professors who supervised my thesis/dissertation work or, in their absence, by the Head of the Department or the Dean of the College in which my thesis work was done. It is understood that any copying or publication or use of this thesis/dissertation or parts thereof for financial gain shall not be allowed without my written permission. It is also understood that due recognition shall be given to me and to the University of Saskatchewan in any scholarly use, which may be made of any material in my thesis/dissertation.

Requests for permission to copy or to make other uses of materials in this thesis/dissertation in whole or part should be addressed to:

Dean
College of Graduate and Postdoctoral Studies
University of Saskatchewan
116 Thorvaldson Building, 110 Science Place
Saskatoon, Saskatchewan S7N 5C9
Canada

Or

Head of the Department of Chemistry
University of Saskatchewan
Thorvaldson Building, 110 Science Place
Saskatoon, Saskatchewan S7N 5C9
Canada

Abstract

The focus of this thesis is on the synthesis, characterization, and application of Pd-based single-atom catalysts (SACs). An emphasis will be placed on the characterization of these materials through X-ray Absorption Spectroscopy (XAS) and use as selective catalysts in oxidation and hydrogenation reactions.

The first project discusses the characterization of quasi-homogeneous AuPd catalysts and their use in the selective oxidation of crotyl alcohol. The quasi-homogeneous catalysts were synthesized via two reduction routes, co- and sequential reduction, with varying Au/Pd ratios from 4/1 to 1/1. Transmission Electron Microscopy (TEM) and X-ray Photoelectron Spectroscopy (XPS) analyses were performed to confirm the bimetallic nature of these catalysts. X-ray Absorption Near-Edge Structure (XANES) was used to probe the local atomic structure of Au and Pd in these systems, while Extended X-ray Absorption Fine Structure (EXAFS) data was modelled to quantitatively discuss the surrounding environment of Au and Pd in terms of coordination numbers (CN) and bond distances between neighbouring atoms and the metal center. An oxidation reaction of crotyl alcohol into three products, crotonaldehyde, 1-butanol, and 3-buten-1-ol, was performed to quantify the selectivity of each catalyst to crotonaldehyde. As the ratio of Au/Pd decreased towards unity, the selectivity decreased in both catalyst systems (i.e., co- and sequentially reduced Au_xPd).

The second project consists of the characterization of a heterogeneous Pd catalyst supported on graphitic carbon nitride ($Pd/g\text{-}C_3N_4$) and its use in the selective hydrogenation of an alkyne, 2-methyl-3-butyn-2-ol (MBY) to 2-methyl-3-buten-2-ol (MBE), an alkene. XANES and EXAFS analyses were performed to determine structural information with varying weight

percentages of Pd (0.1%, 0.5%, and 2.0%). These Pd/gC_3N_4 catalysts were compared in the hydrogenation of MBY to see if selectivity towards MBE was affected. There was no semblance of selectivity, though as the amount of Pd in g-C_3N_4 was increased, the activity of the catalyst increased. A comparison was then performed between a 0.5% Pd/g-C_3N_4, Pd NP and co-Au_4Pd catalyst in the hydrogenation of MBY. Results show that the supported Pd catalyst was most active, though none of the catalysts were selective for this reaction, suggesting there is no structure-sensitivity present. The loading of Pd in the heterogeneous catalyst was much lower than the co-Au_4Pd, showing that metal loading can be decreased without sacrificing activity.

Acknowledgements

I would like to thank all my friends and family for their continuous support and encouragement throughout my master's project. Most importantly, my parents: Sherry Atwell and Randy Chivers, along with their respective partners, Bob Mulligan and Sue Faul.

I would like to thank Dr. Robert W.J. Scott not only for taking me on as a master's student but also as an undergraduate researcher for two years. Dr. Scott has been a tremendous leader for me and taught me many valuable lessons in research and in life. Thank you for all the support you have given me over the many years of supervision.

I would like to thank all the Scott group members over the years, particularly William Barrett. Will and I started out in the Scott group as undergraduate summer students at the same time and continued under Dr. Scott, for the duration of both our master's programs. Will has been a support throughout the many years of work, and I'm glad to have gone through it all with him.

I would like to thank all the faculty and staff at the University of Saskatchewan and Canadian Light Source, including Larhonda Sobchishin, Ning Chen, Weifeng Chen, Danielle Covelli, Jianfeng Zhu, Alexandra Bartole-Scott, and Adrian Clark.

Lastly, I would like to thank my partner of 8 years, Aidan Mowat, for keeping me level-headed throughout this process and providing endless encouragement. I truly have no idea where I would be without her. She has been with me throughout my entire education, and I cannot thank her enough.

To Aidan Mowat, my family, and friends

Thank-you for all your support

Table of Contents

List of Tables

List of Figures

List of Schemes

List of Abbreviations

AC-STEM	Aberration Corrected Scanning Transmission Electron Microscopy
ALD	Atomic Layer Deposition
ATR-IR	Attenuated Total Reflectance Infrared Spectroscopy
EG	Ethylene Glycol
EXAFS	Extended X-ray Absorption Fine Structure
GC-FID	Gas Chromatography with Flame Ionization Detector
HAADF	High Angle Annular Dark Field
HAP	Hydroxyapatite
HHDMA	Hexadecyl-2-hydroxyethyl-dimethylammonium Dihydrogen Phosphate
MO	Metal oxide
NC	Nanocluster or Nanocrystal
NP	Nanoparticle
OLAC	Oleic Acid
OLAM	Oleylamine
$Pd(hfac)_2$	Palladium Hexafluoroacetylacetate
PVP	Polyvinylpyrrolidone
SAA	Single-Atom Alloy
SAC	Single-Atom Catalyst
SPR	Surface Plasmon Resonance
STEM	Scanning Transmission Electron Microscopy
TBAB	*Tert*-Butylamine
TEM	Transmission Electron Microscopy

TOF	Turnover Frequency
TON	Turnover Number
VA	Vinyl Acetate
XAFS	X-ray Absorption Fine Structure
XANES	X-ray Absorption Near-Edge Structure
XAS	X-ray Absorption Spectroscopy
XPS	X-ray Photoelectron Spectroscopy

Chapter 1: Introduction

1. Introduction

The scientific literature in the catalysis field contains studies on a multitude of different types of catalysts, with the goal of showing how well they perform in terms of activity or selectivity for a particular chemical reaction. In general, a catalyst is a chemical species/element that increases the rate of the reaction but is not consumed during the reaction. The activity of a catalyst is measured in terms of conversion of the substrate to products, or by turnover number (TON) and turnover frequency (TOF). Conversion is simply the percentage of product that is produced relative to the amount of starting material. A TON is a number that indicates, on average, how many molecules of a substrate can be converted by one atom of the catalyst. Selectivity is measured by how well a catalyst can allow the synthesis of a specific product over another from the starting material. An example reaction is shown in Scheme 1.1, where A is converted into two products, B and C. If the catalyst could solely produce B, that would be a highly selective catalyst.

Scheme 1.1. A model reaction of some substrate A converting to two products, B and C.

There are many different types of catalysts in the scientific literature. Some of these catalysts include biocatalysts, organometallic catalysts, electrocatalysts, and the broad field of nanomaterial catalysts.[1] Biocatalysts are natural catalysts known as enzymes, which are used in numerous chemical transformation reactions to produce industrially relevant pharmaceuticals or chemical products that are used in everyday life.[2] An organometallic catalyst is a catalyst that contains at least one bond between a metal species and a carbon molecule, such as ferrocene or titanocene.[3] Electrocatalysts are increasingly popular catalysts that are used in energy and fuel

production. These catalysts incorporate transition metals into electrode-based frameworks to produce batteries and fuel cells, among many other electrochemical technologies.[4] Lastly, the area of nanomaterial catalysis is vast, incorporating numerous types of metals into catalysts for lab-scale and industrial-scale processes. Within this area of catalysis, three main morphologies will be discussed. Those three are the nanoparticle catalyst (NP), nanocluster catalyst (NC), and most pertinent to this work, the single-atom catalyst (SAC).

The focus of this thesis will be on comparing bimetallic AuPd NP catalysts, AuPd SACs, and supported Pd/g-C_3N_4 catalysts in selective oxidation and hydrogenation reactions, with a particular emphasis on the characterization of these catalysts.

1.1 Nanomaterial Catalysis

Nanomaterials have been in use, although unknowingly, for centuries; for example, the red and purple pigments seen in the Rose Window of the Cathedral of Notre Dame are Au NPs.[5] Two centuries later, the first nanomaterials used for catalysis were Ag NPs in the field of photography and Pt NPs for the decomposition of hydrogen peroxide.[6] Now in the 21st century, nanomaterials are used in numerous ways, such as quantum dots,[7,8] carbon nanotubes,[9,10] monometallic and bimetallic NPs,[11–14] monometallic and bimetallic NCs,[15–18] and SACs, with the latter being discussed throughout the body of this work. All of these catalysts are synthesized using a variety of elements, like C,[10] Fe,[19–21] Ti,[22,23] Cu,[24,25] Pd,[26–29] Ag,[30–32] and Au,[33–35] to name a few of the more common ones. The popularity of nanomaterial catalysis is due to their ability to efficiently catalyze numerous reactions, such as oxidations,[36–41] hydrogenations,[13,42–46] and C-C coupling reactions.[6,47,48] A major parameter that dictates the activity of these catalysts is size, and a detailed discussion on this attribute is found below.

1.1.1 How Catalyst Size Dictates Activity

Nanomaterials have specific size ranges that have been defined in the literature. For NPs, it is generally accepted that their size regime is between 2 and 100 nm,[49–51] while NCs are considered to be any nanomaterial with an average size < 2 nm.[49–51] The size of nanomaterials decreases all the way to the single-atom limit,[52–54] where the catalyst cannot be made smaller. A single-atom catalyst is a system in which individual catalytic atoms are discrete units that are separated in space by either a catalytic support or a second inactive metal matrix. This change in size causes a change in the surface area of the catalyst, which has an effect on the activity and selectivity of chemical reactions happening on the surface. A decrease in particle size from an NP to NC regime coincides with an increase in the surface area[55] and therefore is economically less costly in terms of the amount of metal needed for catalysis. In a review on SACs, Liang *et al.*[56] compared the difference between using an Au brick versus a brick coated in a layer of Au for some arbitrary catalytic reaction. For this arbitrary system, only the metal on the surface matters for the reaction. The Au brick has a dimension of 20 x 10 x 5 cm and is made entirely of pure Au. At the time of writing, the price of Au was $38.1 per gram, which would make the pure Au brick worth ~ $736, 000, while the Au coated brick would be worth 21 cents. If only the surface of the material matters, that would mean a large portion of that cost is not being used efficiently by the catalyst, it is simply in the core of the catalyst. Comparatively, the brick with the same dimensions and a layer of Au only on the surface will behave similarly as a catalyst, though the core of the catalyst is made from inexpensive inert material. This brick coated in Au is analogous to NC catalysts, where similar activity is observed relative to NP catalysts, but the NCs are economically more viable compared to the NP system. At the single-atom limit of a nanomaterial, the brick would have single atomic sites of Au coating the surface. At the single-atom limit, the surface area is at

a maximum as no metal sites are wasted, that is, they are all active sites that can be targeted by the substrate in the cycle. This is deemed as an increase in the specific activity per metal atom of the catalyst.[53,55]

Not only does catalyst size affect activity, but it can also play a role in the selectivity in producing desirable products. The work from Liu *et al.*[42] compares the selectivity of Pd catalysts of varying sizes towards the production of 1-hexene from 1-hexyne. 1-Hexene is the partially hydrogenated product, where 1-hexyne can also be hydrogenated to its alkane form, 1-hexane. Their work compares larger Pd NPs supported on activated carbon (Pd/C) to a single-atom bimetallic PdAu single atom alloy supported on silica (Pd-Au-SAA/SiO_2), where single Pd atoms were deposited on an Au/SiO_2 support. Both catalysts were used in the same hydrogenation setup using a stainless-steel Parr reactor at 25 ^oC with 5 bar $H_{2(g)}$ flowing through the reactor. The Pd/C catalyst contained 10% by weight Pd, while the Pd-Au-SAA/SiO_2 catalyst contained 0.008% Pd and 3.8% by weight Au/SiO_2, as determined by ICP-AES. Results show that after full conversion of 1-hexyne, the selectivity to the alkene, 1-hexene, is 85% and < 10% for the Pd-Au-SAA/SiO_2 and Pd/C catalysts, respectively. These results conclude that introducing isolated Pd atoms onto some support surface can greatly enhance the selectivity in catalytic reactions relative to larger NP catalysts made of the same metal. It is noted that the Au/SiO_2 system is inert without Pd adsorbed onto the surface for this reaction.

Work from Liu *et al.*[42] noted above indicates the usage of Pd in a nanomaterial catalyst. The usage of Pd in nanomaterials is a popular area of research in the nanocatalyst field, with a detailed discussion on the use of these Pd nanomaterials given below.

1.1.2 The Usage of Palladium in Nanomaterial Catalysis

An influx of Pd nanomaterial research occurred in the mid-1990s when Pd NPs were used by Reetz for Heck carbon-carbon coupling reactions.[6] The usage of Pd in nanomaterial catalysis since then has been prominent in numerous chemical reactions, either as a monometallic species in solution or supported on an inert surface.[57–59] Alternatively, Pd can be combined with other transition metals to make bimetallic NPs, which can also be used in solution or supported on a substrate.[14,28,39,42] Bimetallic catalysts are useful as they can promote different electronic and geometric effects[60–62] compared to monometallic catalysts that greatly enhance the catalytic activity of the bimetallic catalyst. An example of an electronic effect is seen in many AuPd bimetallic catalysts, where Au withdraws electron density from Pd, increasing the activity of the catalyst relative to monometallic Au and Pd counterparts.[61,63] An example of a geometric effect would be changing Pd-Pd and Pd-Au bond lengths to make a catalyst more effective, or such as the work in this thesis, dispersing single atoms of Pd on a metal surface to enhance or manipulate the activity of the catalyst.[52,60,62] Pd is known to be a highly efficient metal for numerous catalytic systems such as oxidation[14,26,27,39,64–66] and hydrogenation[42–44,46,67,68] reactions, though it can become quite expensive if used in large quantities. Numerous types of Pd nanomaterials have been used as efficient catalysts, ranging from large NPs to NCs, all the way down to the single-atom limit of Pd.

A great example of bimetallic Pd NP catalysis was shown by Agarwal *et al.*[39] in the selective oxidation of methane gas (CH_4) using PdAu colloid catalysts. In this work, an AuPd NP catalyst was synthesized and compared to monometallic Pd and Au NP catalysts for the oxidation of CH_4 in the presence of O_2 and hydrogen peroxide (H_2O_2). The catalytic reaction was carried out in a Parr autoclave reactor under high stirring (1500 rpm) and moderate temperatures (50 ^oC). The

desired product of this oxidation was methylhydroperoxide (CH_3OOH) and methanol (CH_3OH), which were deemed "primary oxygenates," with formic acid (HCOOH) and CO_2 as undesired products. They found high primary oxygenate selectivities of ~ 90% for the Au-Pd colloid catalyst, while the monometallic Pd and Au NPs showed selectivities of 0% for primary oxygenates at similar conditions. This is a prime example of modifying the existing Pd NP morphology by incorporating a second transition metal into the Pd matrix, promoting electronic effects that increase the activity of the bimetallic catalyst relative to the monometallic catalysts.

Pd NCs, although less popular than Pd NPs in the literature, have also been shown to be effective catalysts. Ueno *et al.* studied Pd NCs that were encapsulated in an apo-ferritin cavity.[69] This was done by treating apo-ferritin with 500 equivalents of K_2PdCl_4 and adjusting the pH to 8.5 using 0.1 M NaOH. Pd was reduced from an oxidation state of +2 to 0 via $NaBH_4$ reduction. Then, the Pd apo-ferritin composite (Pd/ferritin) was isolated from solution using size-exclusion chromatography. Once isolated, the size of Pd NCs in the ferritin complex was determined to be 2.0 ± 0.3 nm via TEM analysis. Pd/ferritin was analyzed catalytically in the hydrogenation of olefins, and the results were compared to bare Pd NPs without the ferritin complex. Catalytic results show that Pd/ferritin was stable throughout the reaction and did not produce side-products, whereas other Pd NP systems are not as stable. In addition to the stability of Pd/ferritin, it was shown that the TOFs obtained were similar to those achieved with Pd NPs or better in the case of certain substrates. Structural changes to the Pd/ferritin complex relative to bare Pd NPs showed an enhancement in stability, and in some cases, the activity of the Pd NCs.

Single-atom Pd catalysts are a new avenue of catalyst being explored in the nanomaterial field, showing higher efficiencies and better performance than typical Pd NP and NC catalysts. Multiple examples from the literature will be discussed in great detail below, with a particular

interest in bimetallic and supported Pd SACs, as well as other unique SACs that are prominent in the literature.

1.2 Synthesis of Single-Atom Catalysts

Monometallic SACs can be synthesized and used as quasi-homogeneous catalysts (with bimetallic SACs dispersed in liquids) or as heterogeneous catalysts, where metal is deposited on some substrate material. Bimetallic SACs can be synthesized in similar ways for both quasi-homogeneous and heterogeneous systems. As discussed in Section 1.2, heterogeneous catalysis is becoming a popular area in single-atom catalysis, with quasi-homogeneous systems discussed far less frequently.[53,55,56,70–73] In Section 1.2, numerous types of SACs made out of different metal precursors are discussed, though Section 1.3 will mainly focus on Pd-based SACs in quasi-homogeneous and heterogeneous morphologies. Typical strategies towards synthesizing quasi-homogeneous Pd-based SACs are co-reduction and sequential reduction of a Pd precursor with an Au precursor to design bimetallic catalysts.[74–77] Heterogeneous Pd-based SACs are often synthesized in the very simple metal-deposition approach, where Pd precursors are reduced onto the surface of an inert support material made out of g-C_3N_4, metal oxide (MO), or graphene.[43,46,78–80]

The work in Chapter 3 and 4 involves the use of bimetallic AuPd SACs that are quasi-homogeneous and Pd/g-C_3N_4 SACs that are heterogeneous, for selective catalytic reactions. The precise syntheses of these catalysts are given in Chapter 2, though the theory behind each will be discussed in the subsequent subsections.

1.2.1 Co-reduction Strategies Towards Bimetallic Single-Atom Catalysts

A typical method for making bimetallic NP catalysts is the co-reduction method. As the name implies, two metal precursors are mixed in some solvent together and reduced at the same time by some reducing agent to create a bimetallic material consisting of both reduced metals. If the metals are reduced at similar rates, an alloy can be produced. An example of co-reduction being used to make bimetallic AuPd NP catalysts is shown by work from our group by Balcha *et al.*[75] In this work, AuPd NPs were synthesized with an Au/Pd ratio of 1/3 by mixing $HAuCl_4 \cdot 3H_2O$ (Au precursor) with K_2PdCl_4 (Pd precursor) in deionized water. After sufficient mixing, excess sodium borohydride ($NaBH_4$) was added to reduce both Au and Pd precursors into an AuNP matrix.

Co-reduction of metal precursors to form bimetallic NPs can be applied to SACs as well, though very few examples exist in the literature. One approach towards synthesizing bimetallic AuPd SACs via co-reduction is performed using a microfluidic mixing apparatus.[76] In microfluidic mixing, two reagents can be added together at some programmed rate. This can be applied to co-reduction in the sense that precursor Au and Pd metals dissolved in a solution can be reduced at a programmed rate to form AuPd SACs, as shown by the work of Hayashi *et al.*[76] Hayashi and co-workers took a microfluidic mixing approach to dope single Pd atoms in an Au NP core. To do this, $HAuCl_4$ and $PdCl_2$ were mixed in polyvinylpyrrolidone (PVP) and HCl in an ice bath at 273 K. Another solution containing $NaBH_4$ and PVP was prepared. Both solutions were placed into a microfluidic mixer in an ice bath and mixed by injecting both solutions from automatically actuated syringes at a rate of 200 mL/h. They showed that the catalyst contained single Pd atoms in an Au matrix by numerous characterization techniques such as MALDI mass spectrometry and X-Ray Absorption Fine Structure (XAFS). The alloy structure for these AuPd SACs is shown in

Figure 1.1, where the Au NPs are populated with single Pd atoms throughout the structure and on the surface.

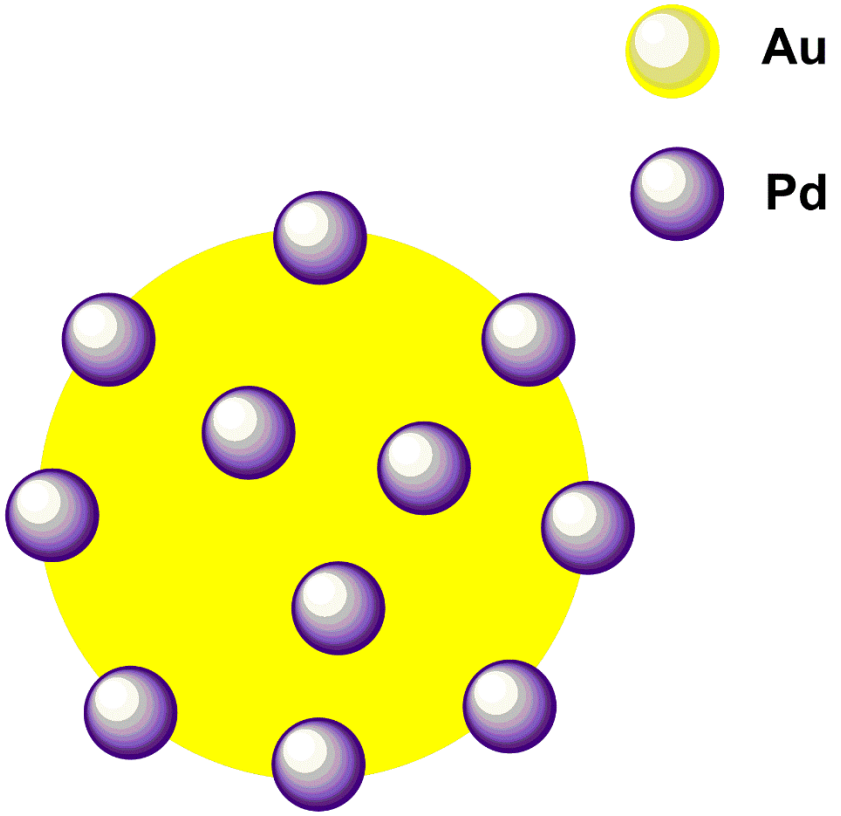

Figure 1.1. A depiction of an AuPd SAC, with isolated Pd atoms in a larger matrix of Au atoms.

1.2.2 Sequential Reduction Strategies Towards Bimetallic Single-Atom Catalysts

Another commonly employed method to develop bimetallic catalysts is through sequential reduction. In a sequential reduction approach, one metal is first reduced by some reducing agent to create a precursor metal NP solution. To this, the second metal of choice can be mixed in the solution and reduced again to form what is generally called core-shell nanoparticles.[75,77,81] An example of a sequential reduction synthesis was shown by Chen *et al.*,[77] who made a Ni@Pt core-shell NPs via sequential reduction. First, Ni core NPs were prepared by mixing Ni (II) acetate,

NaOH, and oleic acid in 1,2-propanediol. The temperature was then increased to 138 ^{o}C, and $N_{2(g)}$ was introduced. KBH_4 in 1,2-propanediol was slowly added to the reaction under $N_{2(g)}$ to reduce the Ni particles. At this point, Ni core NPs were obtained. Small amounts of H_2PtCl_6 were then added dropwise to the Ni NPs in the presence of 1,2-propanediol at 138 ^{o}C to create a shell of Pt around the Ni NPs. Therefore, a core of Ni was first synthesized in solution, then a precursor of Pt was introduced into the system and reduced onto the Ni to form a shell. This is an example of a sequential reduction of metals to form a bimetallic catalyst.

A sequential reduction strategy towards synthesizing an AuPd SAC was shown by Liu *et al.*,[42] where an Au-Pd single atom alloy (AuPd-SAA) is synthesized. First, Au NPs were synthesized by mixing $HAuCl_4 \cdot 3H_2O$ with PVP in ethylene glycol (EG) under N_2 for one hour. $NaHCO_3$ was then introduced, and the solution was heated to 90 ^{o}C at 5 ^{o}C min^{-1} under $N_{2(g)}$ flow. The solution was stirred at 90 ^{o}C for 30 minutes before cooling to room temperature, which produced Au NPs through glycerol reduction at high temperatures. Then, $Pd(NO_3)_2$ in EG was added to the Au NPs under $N_{2(g)}$ and vigorous stirring. The solution was again heated to 90 ^{o}C at 5 ^{o}C min^{-1} and stirred for 8 hours under these conditions to reduce Pd onto the Au NPs. This AuPd-SAA NP catalyst that was synthesized is not a core-shell nanoparticle in the traditional sense. The core of the catalyst is indeed made of Au NPs, but the Pd:Au ratio was chosen such that only single sites on the Au NP core contain Pd atoms, rather than a continuous shell of Pd. This was supported by TEM imaging and IR-adsorption studies using CO.

In conclusion, a general sequential reduction approach to synthesize bimetallic NPs or SACs will include first reducing some metal species to make the core NP. Then, a second metal species can be added to the core and reduced to create a shell or isolated site of that second metal

species. A typical core-shell structure for both an AuPd SAC and AuPd core-shell NP is shown in Figure 1.2.

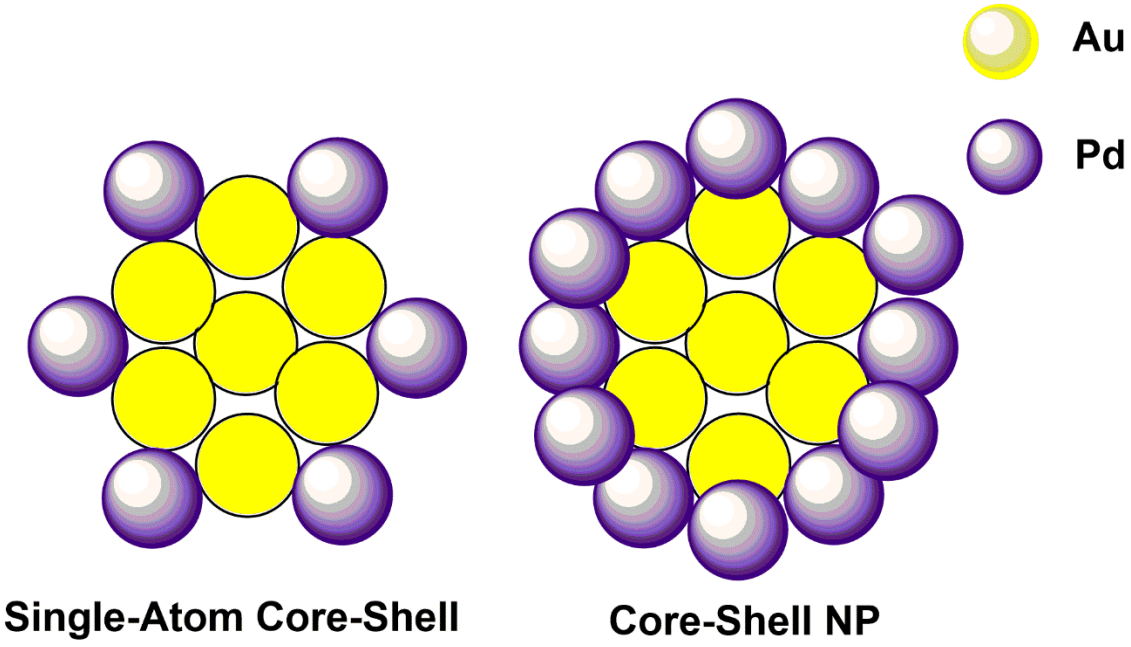

Figure 1.2. Core-shell morphology of an AuPd SAC and NP.

1.2.3 Metal Deposition Approach towards Heterogeneous Single-Atom Catalysts

As mentioned in Section 1.2, the synthesis and use of heterogeneous SACs dominate the field of single-atom catalysis. This is due to the inexpensive and facile approach towards designing these catalysts, as will be shown by a few literature examples. The focus in this section will be on monometallic Pd-supported SACs, though it is possible to make bimetallic supported SACs as well.[18,82–84] Metal deposition is generally performed by mixing a metal precursor in solution with the support material and then reducing that metal precursor onto the support. Common support materials include g-C_3N_4, MO, and graphene, with g-C_3N_4 being the focal point of this section.

Graphitic carbon nitride (g-C_3N_4) is a common substrate for metal deposition syntheses because it provides a large surface area for deposition, is very stable, promotes strong metal binding at the N sites, and is simple to synthesize.[72,78,85] Chen *et al.*[78] have been able to show that Pd, Ag, Ir, Pt, and Au can all be deposited on g-C_3N_4 to produce heterogeneous SACs. In general, this is done by first synthesizing g-C_3N_4 by calcining dicyandiamide at 823 K under N_2 flow for 4 hours. Then, the metal precursor for any of the five metals mentioned is dispersed in water by sonication and mixed with the g-C_3N_4 support, and often followed by reduction with $NaBH_4$. The solid is then collected and washed with a water/ethanol mixture and dried in an oven at 323 K to produce M/g-C_3N_4 (M = Pd, Ag, Ir, Pt, or Au). A similar metal deposition method towards creating heterogeneous Pd-based SACs is found in many papers.[53,57,73,86]

Predicting where the reduced metal resides in the g-C_3N_4 matrix is a little challenging. It has been reported by He *et al.*[87] that Pd is doped into five possible sites on the g-C_3N_4 matrix, as shown in Figure 1.3. The five possible sites are the center of the cavity (1), at the corner of the cavity (1), on top of the nitrogen ring (3), at the edge of the cavity (4), or on top of g-C_3N_4 (5). It is noted that the center of the six-fold cavity, indicated by 1 in Figure 1.3, is the most stable site for an isolated Pd atom to reside in this matrix.[88,89]

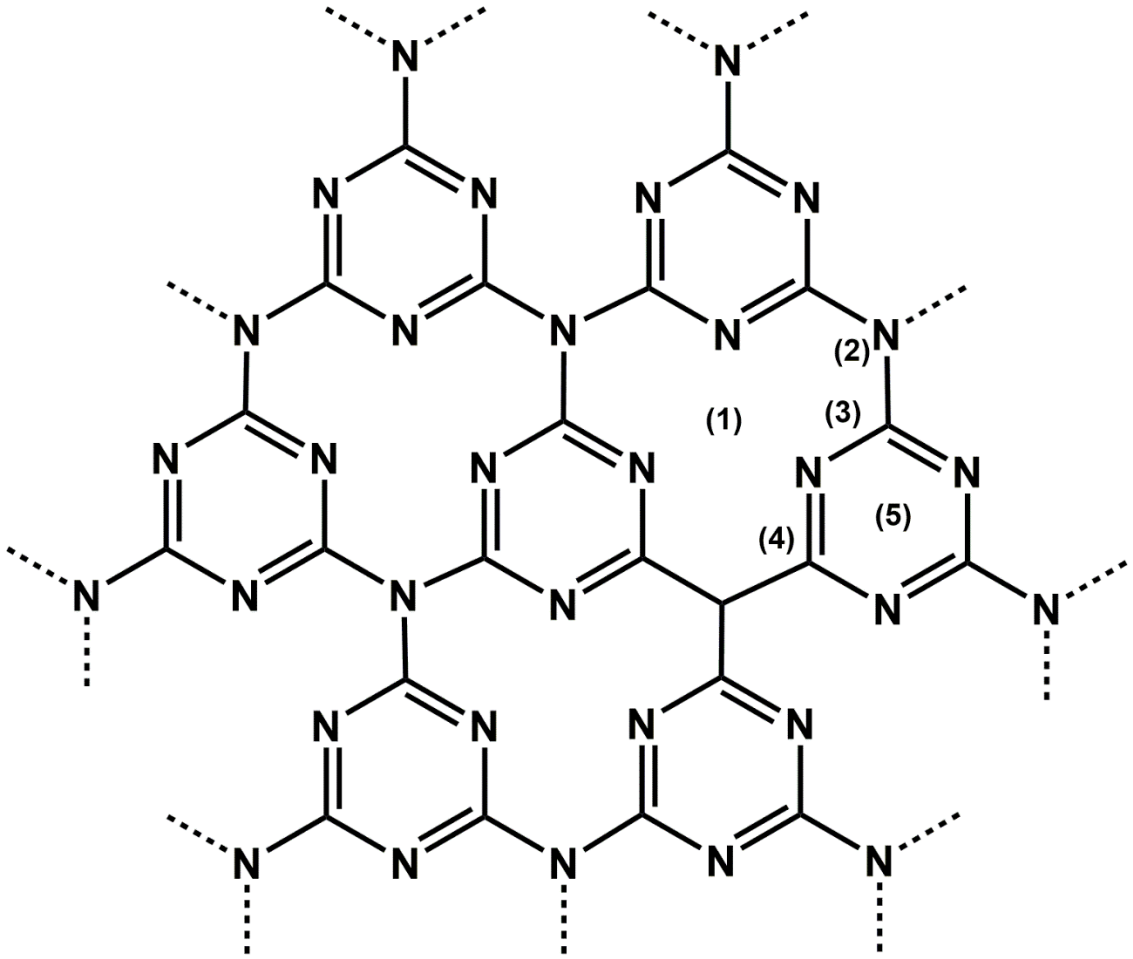

Figure 1.3. A theoretical depiction of where Pd (the numbers in brackets) can be located when reduced on g-C_3N_4, as reported by He *et al.*[87] Reproduced from reference [86], Copyright (2017), with permission from Elsevier.

1.2.4 Other Synthesis Methods Towards Designing Single-Atom Catalysts

The most prevalent synthesis methods pertaining to the work in this thesis have been discussed in sections 1.2.1, 1.2.2, and 1.2.3. There are, however, numerous ways to synthesize SACs, though a majority of the literature discusses heterogeneous SACs rather than quasi-

homogeneous systems, as reported in these reviews.[53,55,71,73] Therefore, other methods to produce heterogeneous SACs include co-precipitation, atomic layer deposition (ALD), galvanic replacement, high-temperature pyrolysis, and high-temperature atomic migration as reported by Li *et al.*[90] and Zhang *et al.*[53] An in-depth discussion on these methods is not pertinent to the work in this thesis, though it should be noted that other synthesis methods beyond the scope of this work exist in the SAC literature.

1.3 Single-Atom Catalysts (SACs)

A continual decrease in metal catalyst sizes has been evident over the past decade, moving from larger NPs down to the single-atom limit of metals on different support materials.[53,55,56,71–73,91] The benefit of this size reduction down to the atomic scale is an increase in the economic efficiency of the catalyst – that is, less metal is being used in the synthesis of these catalysts, and thus higher activities and selectivities are being achieved relative to their NP and NC counterparts as will be discussed in detail in subsequent subsections. A SAC can come in many forms, though all definitions come to the same conclusion – a SAC contains single-sites of some metal supported on a surface. The support surface can vary drastically, though the single-site morphology of the catalyst does not vary, that is, the metal does not agglomerate and only occupies a single site on or in the support matrix. A nice example of this distinction is shown in Figure 1.4 from work by Yang *et al.*[55]

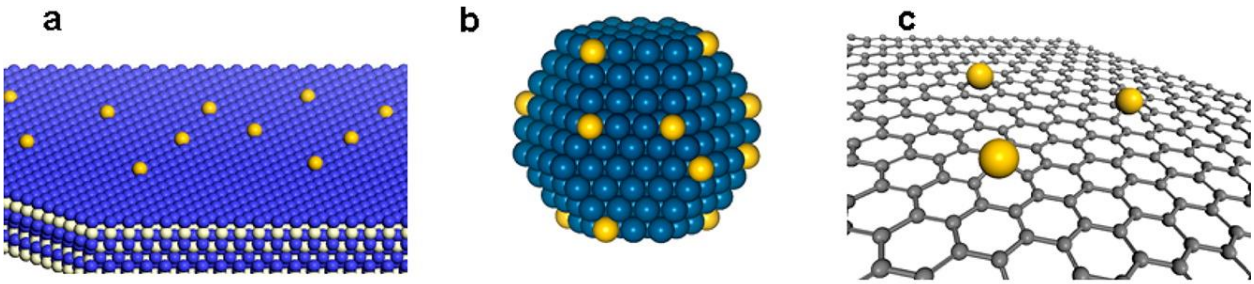

Figure 1.4. Representations of different SAC morphologies with a single-site metal atom (yellow) on a) metal oxide, b) metal nanoparticle, and c) graphene support surfaces. Reprinted with permission from reference [55]. Copyright (2013) American Chemical Society.

A challenge in the field of SACs is whether homogeneous or heterogeneous catalysts are desirable. Literature results would suggest there is a stark difference between the two morphologies, with heterogeneous catalysis becoming increasingly popular.[53,55,56,70–73] The heavy interest in heterogeneous catalysis directly relates to the stability and recoverability relative to homogeneous systems, though homogeneous catalysts often have shown higher activities.[53,56,73]

The work in this thesis will compare a bimetallic quasi-homogeneous AuPd SAC to a heterogeneous Pd SAC supported on graphitic carbon nitride (Pd/g-C_3N_4) towards oxidation and hydrogenation reactions, though numerous examples in the literature exist using different metals to make bimetallic or monometallic SACs for a multitude of catalytic systems[92–96] including precious metals like Pt,[89,97] Au,[98] Ir,[99] and Rh[100] and other metals like Fe[101] and Co.[102] Specific examples from the literature will be discussed in subsequent sections below in greater detail.

1.3.1 Quasi-Homogeneous Bimetallic AuPd Catalysts

The term quasi-homogeneous indicates that the system is not truly homogeneous; that is, not all reactants are in the same phase. For bimetallic AuPd NP SACs, the term quasi-

homogeneous is more appropriate as the synthesis generally involves dissolving some metal precursor species in solution in the presence of organic stabilizer and reducing it to create the NP catalysts dispersed in solution. While the solution itself appears homogeneous, it has very small solid NPs dispersed in it. Therefore, these bimetallic SACs should be called quasi-homogeneous catalysts rather than homogeneous catalysts, though this distinction is not always made in the literature. A general structure of a quasi-homogeneous AuPd NP SAC is shown in Figure 1.1, where isolated Pd atoms reside in a matrix of Au atoms. This is a depiction of the surface of an AuPd SAC, where larger amounts of Au will be present in the core with most of the isolated Pd atoms on the surface of that Au core.

Bimetallic AuPd catalysts have been studied extensively in the nanomaterial catalysis field, whether these are bimetallic AuPd NPs,[39,82,103] NCs,[104–106] or most recently, SACs.[42,57,76,107] While AuPd is the most popular combination in the literature, PdCu is an alternative bimetallic SAC that is studied in dehydrogenation reactions.[108,109] The combination of Pd and Au metals has been shown to create an alloy, where the catalytic activity is increased relative to the monometallic substituents.[110–112] An example of this alloy effect can be seen by the work of Mertens *et al.*[112] In this work, a monometallic Au NP was doped with Pd to make an AuPd NP and used for the room temperature oxidation of benzyl alcohol to benzaldehyde. Monometallic Au and Pd NPs showed conversions to benzaldehyde of 35% and 40%, respectively. The Au/Pd ratio in AuPd NPs was varied between pure Pd and pure Au, with an 8/2 ratio of Au:Pd showing near 100% conversion using the same overall metal loading and conditions. It should be noted that all ratios of Au/Pd showed increased conversions relative to their monometallic counterparts, with the lowest conversion of ~ 45% seen for the bimetallic system at an Au/Pd ratio of 1/9.

Numerous studies on bimetallic AuPd NPs vs monometallic Pd and Au NPs have been performed by our group in alcohol oxidation reactions.[26,27,74,75] Work by Maclennan *et al.*[27] evaluated the oxidation of unsaturated alcohols using monometallic Au and Pd NPs and a bimetallic PVP-stabilized AuPd system with an Au:Pd ratio of 1:3. PVP-stabilized AuPd NPs were synthesized via a sequential reduction approach. First, Au NPs were synthesized by reducing $HAuCl_4 \cdot 3H_2O$ in a PVP/water mixture at 0 ^oC and 1200 rpm stirring using $NaBH_4$. After dialyzing the Au NPs overnight, the Au NP solution was mixed with a Pd precursor, K_2PdCl_4 and ascorbic acid and stirred at 800 rpm for 1 hour. The ascorbic acid reduced Pd under these conditions over the 1 hour stirring. Pd NPs were synthesized similar to the Au NPs, but K_2PdCl_4 was used instead of $HAuCl_4 \cdot 3H_2O$. TEM images were collected, and particle sizes for Au and Pd NP catalysts of 2.9 ± 1.4 nm and 2.7 ± 1.0 nm were seen, while the 1:3 AuPd catalysts had average particle sizes of 3.9 ± 1.7 nm. These catalysts were then evaluated in the oxidation of five different alcohols in water in terms of conversion and selectivity to the aldehyde or ketone that is produced under the oxidation conditions. All oxidation reactions were carried out at 60 ^oC with a substrate:catalyst ratio of 500:1. For all five alcohols, Au NPs showed almost no activity. Likewise, the Pd NPs showed very little activity for each system, whereas the AuPd catalyst showed greater activity in all oxidation reactions relative to its monometallic counterparts. The presented work shows how incorporating two metals into a catalyst can increase activity for the oxidation of numerous alcohol systems. It has been shown by previous work[26,27,74,75] that electron density is withdrawn from Pd by Au in these bimetallic NP systems, subsequently showing higher activities in alcohol oxidation reactions relative to monometallic NP catalysts. It should be noted that the Pd/Au ratios in previous group work were typically quite high.

More recent research by other groups has been conducted on AuPd SACs with low Pd loadings, in which Pd atoms are isolated and dispersed on an Au nanomaterial surface. Recent work by Wrasman *et al.*[14] describes the synthesis of a bimetallic Pd/Au single-atom alloy system (Pd/Au SAA) with varying Pd loadings supported on TiO_2. While this catalyst is not truly quasi-homogeneous, it shows the effects of bimetallic catalysts compared to its monometallic counterparts. First, Au NCs were synthesized by reducing $HAuCl_4 \cdot 3H_2O$ in oleylamine (OLAM) and tetralin under stirring at 40 ^oC. To make the Pd/Au SAA catalyst, previously made Au NCs were dissolved in a mixture of hexanes, OLAM, and oleic acid. To this mixture, a Pd precursor, $Pd(NO_3)_2 \cdot 3H_2O$ was added, followed by heating to 140 ^oC. The Pd/Au ratio was controlled by adding stoichiometric amounts of $Pd(NO_3)_2 \cdot 3H_2O$ to 30 mg of dissolved Au NCs. The Pd/Au NCs were then supported on TiO_2 by mixing TiO_2 in hexanes and mixing with the Pd/Au NC solution in hexanes to give a weight percentage of 0.5% Pd/Au on TiO_2, followed by heating at 700 ^oC for 30 seconds in the air to remove all organic ligands on the catalyst. The activity of these $Pd/Au/TiO_2$ catalysts with varying Pd loadings was evaluated in the oxidation and hydro-oxidation (hydrogen was co-fed into the reaction) of 2-propanol to acetone. This reaction was run from 0 ^oC to 200 ^oC under both conditions, and the yield to acetone was quantified. Under oxidation conditions (without hydrogen), the monometallic Pd/TiO_2 catalysts were most active, with activity beginning at 75 ^oC, while the Au/TiO_2 catalyst was not active until 125 ^oC. The $Pd/Au/TiO_2$ catalysts showed activity in between these two temperatures, with higher Pd loadings becoming active at lower temperatures. The activity of the catalysts was then evaluated under hydro-oxidation conditions using the same temperature range, and large improvement under hydro-oxidation conditions was seen by comparing the activity of the catalyst under oxidation and hydro-oxidation conditions at 75 ^oC and 125 ^oC. The results of this work show that the hydro-oxidation of 2-propanol to acetone

is improved by the inclusion of single atoms of Pd over an Au surface, whereas monometallic Pd catalysts show minimal improvement under these conditions. The authors state that this improvement using a bimetallic Pd/Au system is possible due to the ability of isolated Pd atoms to split hydrogen while avoiding oxidative dissociation and, therefore, complete combustion reactions, which is observed for the pure Pd catalyst.

It would be pertinent to this discussion to compare AuPd and Au NP systems in oxidation reactions to evaluate the effect of doping single Pd atoms onto an Au NP or NC surface. Chapter 3 will compare bimetallic Au_xPd NPs (where x = 4, 3, 2, and 1), Pd NP, and Au NP catalysts in the selective oxidation of crotyl alcohol. In particular, X-ray absorption spectroscopy will be used to study the effect of doping Pd into an Au matrix in order to understand which AuPd NP systems are truly SACs with singly-dispersed Pd atoms on the surface.

1.3.2 Heterogeneous Supported Pd Catalysts

The area of heterogeneous catalysis is increasingly popular, owing to the ability to recover the catalyst and work with it in harsher conditions compared to homogeneous catalysts.[53,73,86] A common metal deposited on different substrates is Pd, owing to its high activity in oxidation and hydrogenation reactions. Common substrates that Pd can be deposited on include graphitic carbon nitride (g-C_3N_4),[57,72,78] MOs,[43,44,79] and graphene.[46,68,80] These three substrates are highly studied as they provide large surface areas for Pd to deposit on and are all relatively inexpensive. In some particular literature examples, Pd can be combined with other metals and then supported on the aforementioned substrates to either enhance the catalytic ability of Pd or reduce the cost of the catalyst.[71,113,114] Research on supported Pd SACs is incredibly popular as the cost of the catalyst is drastically reduced relative to previously mentioned quasi-homogeneous Pd SACs, while

performance can be maintained or even improved. Au is an expensive material to support Pd on, so researchers have begun using cheap materials like g-C_3N_4, MOs, and graphene to support Pd onto and achieve similar reactivity for some oxidation reactions,[40,79,115–117] but most prominently in hydrogenation reactions.[28,42–44,118]

An example of these supported Pd SACs in hydrogenation reactions can be seen in the work of Huang *et al.*[80] In this work, a g-C_3N_4 support was first synthesized by thermal treatment of urea and solvothermal treatment in a solution of isopropanol and water. A graphene support was made from pristine graphene nanosheets by the Hummer method and then reduced at 1050 ^oC via thermal deoxygenation. Pd was then singly dispersed onto either the g-C_3N_4 (Pd/g-C_3N_4) or graphene (Pd/graphene) support via atomic layer deposition at 150 ^oC using Pd hexafluoroacetylacetate ($Pd(hfac)_2$) and formalin under $N_{2(g)}$. Catalytic activity was evaluated for the hydrogenation of both acetylene and 1,3-butadiene in a fixed-bed quartz reactor for gas-phase reactions with varying temperatures. 50 mg of Pd/graphene was used, and the weight of Pd/g-C_3N_4 was adjusted in each reaction to keep a comparative amount of Pd relative to the Pd/graphene sample. In the hydrogenation of acetylene, the Pd/graphene catalyst showed higher activity than Pd/g-C_3N_4, with 100% acetylene conversion at 60 ^oC compared to 80 ^oC, respectively. The two main products of this hydrogenation were ethylene and ethane. Interestingly, Pd/g-C_3N_4 showed higher selectivity to the ethylene product compared to the Pd/graphene catalyst, with 90% and 78% selectivity to ethylene, respectively. For the hydrogenation of 1,3-butadiene, it was shown that Pd/graphene showed higher activity than Pd/g-C_3N_4 again, with 100% conversion occurring at 47 and 75 ^oC, respectively. The main products of this reaction were butene and butane, though three possible butane species could be made: 1-butene, trans-2-butene, and cis-2-butene. Both

catalysts showed 100% selectivity to butene at 100% conversion, though the distribution of butene products differed.

A catalytic study comparing heterogeneous Pd catalysts was performed by Vilé *et al.*[88] In this work, a single-site Pd catalyst was synthesized via Pd deposition on a mesoporous graphitic carbon nitride support to make Pd/m-C_3N_4. This catalyst was compared to benchmark catalysts for the hydrogenation of 1-hexyne at varying temperatures and reaction times. The benchmark catalysts that were purchased and evaluated were Pd-HHDMA/TiS (HHDMA = hexadecyl-2-hydroxyethyl-dimethylammonium dihydrogen phosphate), Pd-Pb/$CaCO_3$, and Pd/Al_2O_3. ICP-OES was used to evaluate the weight percentage of Pd in each catalyst, with results showing that the Pd weight percentage was 0.5% for both Pd/m-C_3N_4 and Pd-HHDMA/TiS, 4.5% for Pd-Pd/$CaCO_3$, and 1.0% for Pd/Al_2O_3. Aberration-corrected scanning transmission electron microscopy (AC-STEM) was employed to evaluate the surface coverage of Pd on the support material, with 100% metal dispersion being reported for Pd/m-C_3N_4. The benchmark catalysts all had metal dispersions below 40%. The catalysts were evaluated in terms of selectivity to 1-hexene. At 303 K and 1 bar of $H_{2(g)}$, the reaction rates in terms of TOF (in 10^3 $mol_{product}$ mol_{Pd}^{-1} h^{-1}) using Pd/m-C_3N_4 was reported to be three orders of magnitude larger than other hydrogenation catalysts reported in the literature. When the hydrogenation was performed at 343 K and 5 bar of $H_{2(g)}$, similar activities of 1.41 x 10^3 and 1.38 x 10^3 $mol_{product}$ $mol_{Pd}^{-1}h^{-1}$ were achieved for Pd/m-C_3N_4 and Pd-HHDMA/TiS, respectively. High selectivities to 1-hexene were also observed for both catalysts (90%). Pd-Pb/$CaCO_3$ showed similar selectivity at these conditions (90%), but activity was tremendously reduced (0.34 x 10^3 $mol_{product}$ $mol_{Pd}^{-1}h^{-1}$) relative to the single-site catalyst. Pd/Al_2O_3 showed lower activity (0.96 x 10^3 $mol_{product}$ $mol_{Pd}^{-1}h^{-1}$) and selectivity (69%) than the single-site catalyst. Though Pd/m-C_3N_4 and Pd-HHDMA/TiS both perform well, the single-site

catalyst has complete metal dispersion on the surface, while the reference catalyst has poor metal dispersion (16%) and very large Pd NPs on the surface at approximately 8 nm in size. It should be noted that the authors claim a particle size of 0.3 – 0.4 nm is observed for the single-site Pd/m-C_3N_4 catalyst and that this matches the van der Waals diameter of a single Pd atom, though it could be argued that these are in fact NCs of Pd rather than single-atoms of Pd. The authors indicate that the entire surface of Pd/m-C_3N_4 is in use, while only a small portion of the benchmark catalyst is active, with most of the activity being blocked by ligands.

Work in Chapter 4 will evaluate the performance of a near single-atom Pd/g-C_3N_4 catalyst in the hydrogenation of an alkyne, 2-methyl-3-butyn-2-ol. These results will be compared to quasi-homogeneous AuPd catalysts to show how it is possible to reduce the cost of the catalytic material yet maintain high activities. The stability of these Pd/g-C_3N_4 catalysts under the hydrogenation conditions will also be evaluated as it is not evident from the literature that these catalysts retain their single-atom character post-hydrogenation.

1.3.3 Other Types of Single-Atom Catalysts

As mentioned in Section 1.2, Pd is not the only metal employed in single-atom catalysis, with various other catalysts being used throughout the literature, including unique systems like Zn zeolites used as a nanoenzyme[94] and Fe SACs in Li-based batteries.[95] These unique SACs represent this new technology being used in biocatalysis (nanoenzymes) and electrocatalysis (batteries and fuel cells) fields[58,93,95,119] as well as the nanomaterial catalysis field. Perhaps the most common metal used in single-atom catalysis other than Pd is Pt,[78,97,120,121] with a lot of work coming out of the Flytzani-Stephanopoulos group[84,86,120–123] on Pt SACs as well as Pd SACs.

An example of a SAC being used for electrocatalytic applications is shown by Sun *et al.*[95] In this work, a single-atom Fe catalyst, supported on nitrogen-doped carbon (Fe-N_xC), is used as a lithiophilic site in Li-ion batteries to minimize Li nucleation overpotential and dendrimer growth. Electrocatalytic properties were evaluated using a CR2025-type coin cell, designed with Cu foils, with Fe_{SA}-N-C as the anode (Fe_{SA}-N-C@Cu), and Li foil as the cathode. First, the overpotential metallic Li plating on the anode was evaluated for bare Cu, C@Cu, and the sample of interest, Fe_{SA}-N-C@Cu. For the bare and C-coated Cu foils, an overpotential of 62.7 and 18.6 mV was determined, while a value of 0.8 mV was determined for the single-atom material. The authors attribute this much lower overpotential to the single-atom Fe, as the affinity between Li and the carbon-based matrix is improved. At 1 mA/cm^2, Fe_{SA}-N-C@Cu had a stable coulombic efficiency (CE) of 98.8% for 200 cycles, while the other two anode materials showed unstable CE due to likely dendrite growth. The authors concluded that CE was significantly enhanced for the single-atom material due to limiting of dendrite formation, which was characterized via SEM imaging.

As mentioned, Pt is another highly popular metal used in SACs, as shown by the work of out of Flytzani-Stephanopolous' group.[84,86,120–123] Work by Lucci *et al.*[120] discusses how single-atom alloy (SAA) catalysts made of Pt and Cu were evaluated for the selective hydrogenation of 1,3-butadiene to butene. The catalysts evaluated in this reaction were Pt_xCu_y SAA materials supported on Al_2O_3 and a Cu_{15}/Al_2O_3 control. 1,3-butadiene selectivity and activity as a function of temperature were analyzed for the three catalysts, with both SAA materials showing much lower hydrogenation onset temperatures of around 40 ^oC, 35 ^oC lower than the bare Cu catalyst. Comparing different Pt_xCu_y materials, $Pt_{0.2}Cu_{12}/Al_2O_3$ shows greater activity and similar selectivity to $Pt_{0.1}Cu_{14}/Al_2O_3$ due to increased Pt on the surface of the catalyst, though both show single-atom Pt. Both of the SAA catalysts showed full hydrogenation conversion (100%) at

temperatures below 80 ^{o}C, with selectivity to butene at 90%. The bare Cu_{15}/Al_2O_3 catalyst did not show 100% conversion until ~120 ^{o}C, with selectivity only reaching ~75 %. They concluded that as long as Pt atoms are singly dispersed on a surface, increasing concentration of Pt results in higher activities for the selective hydrogenation of 1,3-butadiene to butene, while a non-single atom catalyst of bare Cu shows poorer activity and selectivity.

Lastly, it is important to point out there is tremendous literature on Pd-based organometallic catalysts.[124–126] While not termed as "single-atom catalysts", these species can consist of molecular Pd(0) surrounded by organic ligands. Such Pd(0) organometallic catalysts are famous for their strong activity for C-C coupling in Heck, Suzuki, and Negishi reactions, and are studied thoroughly in the literature. However, such catalysts often possess a stability issue at higher reaction temperatures as the organometallic compound begins to decompose and begins to form larger Pd particles.[127]

1.4 Characterization of Single-Atom Catalysts

Characterization is one of the most important facets of research with many instruments and techniques available to characterize nanoscale materials. The importance of good characterization techniques is especially true for SACs, as characterizing individual atoms on top of a support surface is not simple. Luckily, numerous techniques exist for the characterization of SACs such as electron microscopy (EM), X-ray photoelectron spectroscopy (XPS), infrared spectroscopy (IR), and perhaps most importantly synchrotron-based techniques such as X-ray absorption spectroscopy (XAS).[53,55] Before discussing XAS in detail, it would be pertinent to evaluate a few

characterization techniques that are popular in the SAC literature but were not used for the work in this thesis.

Imaging SACs is crucial to the characterization of their structure. In this thesis, transmission electron microscopy (TEM) was used to image the catalysts and calculate particle sizes, though it could not be used to determine if single-atoms are located on the support surface. A more powerful, high-resolution TEM imaging technique could be employed to analyze the single-atom nature of a catalyst. The most common EM imaging technique used in the literature of SACs is high-angle annular dark-field imaging (HAADF), which is a scanning transmission electron microscopy (STEM) technique that allows the user to discern slight differences in atomic number in terms of contrast in the image, which is often called Z-contrast imaging[53]. With this technique, the surface of a SAC can be imaged, and slight contrast differences will become apparent if the atomic number of the species are different. Numerous groups throughout the SAC field have applied this technique to their work.[10,57,58,78] For example, Kim *et al.*[58] used Z-contrast imaging in their work to identify single-atoms of Pd and Pt on $C@C_3N_4$ supports with varying metal loadings.

Another technique commonly used by other groups is probe-molecule IR spectroscopy.[128] IR spectroscopy is a useful tool to analyze vibrational changes within a sample based on its functional groups or interaction with other molecules in the IR cell. Small changes in the IR spectrum can quantitatively determine what is occurring on the surface of the sample. Probe molecule IR is especially useful in characterizing the surface of SACs, as depending on how a gas adsorbs to the surface of the catalyst, the surface of that catalyst can be characterized. An excellent example of probe IR spectroscopy in SAC characterization was done by Liu *et al.*[42]. They synthesized a Pd-Au single atom alloy (SAA) and wanted to evaluate the surface of this catalyst.

To do this, they used CO-IR spectroscopy, where CO gas was passed through an attenuated total reflection (ATR) IR cell (ATR-IR). Pd NPs were synthesized for this analysis as well and compared to the PdAu SAA catalyst in the bridged-CO region in the IR spectrum (1935 – 1920 cm^{-1}). The results of this comparison show a bridged CO peak for the Pd NPs, whereas the PdAu SAA sample shows no bridged CO peak, indicating single-site Pd atoms on an Au NP surface. The bridged CO peak appears when multiple Pd atoms are within contact of one another, allowing CO to bind to multiple Pd atoms.

The focal point in terms of characterization of the catalysts discussed in this thesis is on XAS. The theory and practical use of XAS will be discussed in the following subsections of section 1.4.

1.4.1 Synchrotron Radiation

The first observation of synchrotron radiation dates back to 1947 from work by Elder *et al.*[129] Today, numerous synchrotron facilities exist throughout the globe and are used by researchers from all science disciplines. Many techniques are available using synchrotron sources, ranging from imaging to spectroscopy. The work in this thesis utilizes a spectroscopy technique called X-ray absorption spectroscopy (XAS), though the fundamentals of synchrotron radiation must be discussed first.

The fundamental building blocks of a synchrotron will not be discussed in this thesis, though it should be noted how synchrotron radiation is produced. In a general synchrotron, electrons are accelerated to a speed close to the speed of light by bending magnets and mirrors.[130] As the electron accelerates, it produces radiation, which can be used at an endstation on the beamline for different analyses. Synchrotron radiation can be quantified by three figures of merit:

flux, brightness, and brilliance.[130] Broadly, flux is the number of photons per second that are delivered to the endstation, brightness is the flux per solid angle, and brilliance is the brightness per source area. These figures of merit are used to compare synchrotron sources around the world, though the most ideal of sources will have high flux and small spot sizes in order to increase the brilliance of the source.

1.4.2 Synchrotron X-ray Absorption Spectroscopy

XAS is an element-specific technique that can be used to determine information on the local atomic structure of a metal centre.[131] XAS is based on the phenomenon called the photoelectric effect, where a core electron absorbs incoming X-rays at specific energies and is emitted depending on a parameter called the binding energy (BE) of the core electron. If the binding energy is less than the incoming X-ray energy, the core electron can be ejected from the core, resulting in the relaxation of an outer shell electron into the vacated core hole. As this outer shell electron relaxes, a photoelectron is emitted into the continuum and can be measured by a detector. However, if the binding energy is greater than the incoming X-ray energy, the core electron cannot be ejected as the incoming X-ray will not be absorbed. Beer's Law is shown in Equation 1.1 and is pertinent to the discussion on XAS, as the absorption coefficient, μ, determines the probability that an X-ray will be absorbed by the core electron:

$$I = I_0 e^{-\mu t} \tag{1.1}$$

where I_0 is the incident X-ray energy, t is sample thickness, and I is the intensity of the x-rays transmitted through the sample. The absorption coefficient is proportional to the sample density ρ, the atomic number Z, the atomic mass A, and the energy of the X-ray E, as shown in Equation 1.2:[131]

$$\mu \approx \frac{\rho Z^4}{AE^3} \tag{1.2}$$

The fact that μ is proportional to Z means specific metals can be analyzed at varying X-ray energies. An XAS graph is simply the absorption coefficient versus photon energy (μ vs. E), and an example of a Pd K-edge is shown in Figure 1.5.

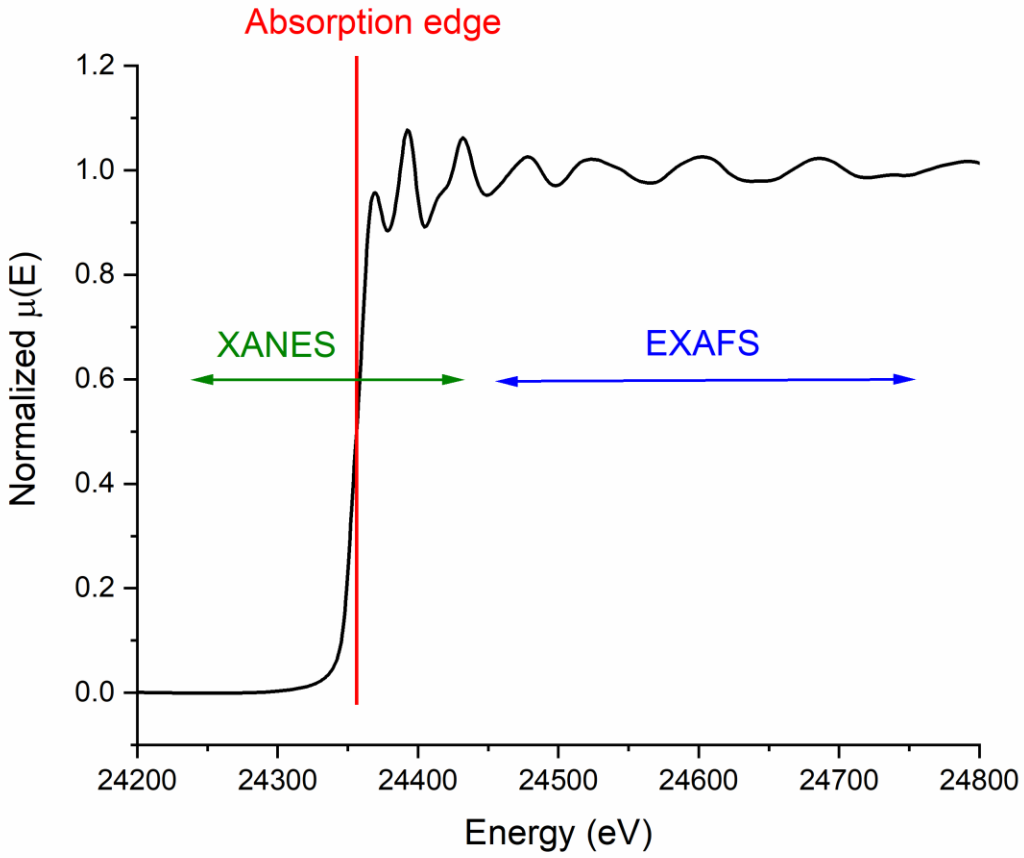

Figure 1.5. An XAS spectrum showing the XANES and EXAFS regions at the Pd K-edge.

The XAS graph is split into two regions: X-ray Absorption Near-Edge Structure (XANES) and Extended X-ray Absorption Fine Structure (EXAFS). Both regions contain useful information about a metal sample and will be discussed in further detail in sections 1.4.2.1 and 1.4.2.2. XANES

is considered to be ~50 eV before and after the absorption edge, while EXAFS is the feature after ~ 50 eV past the absorption edge. Where the absorption edge occurs depends on the element being analyzed. An absorption edge is quantified by the letters K, L, M, N, etc. The K-edge, for example, is the transition of a core electron from the 1s orbital (n = 1). The L-edge would, therefore, be the transition of a core electron from an n = 2 orbital (2s or 2p). The L-edge is slightly more complicated in the sense that n = 2 can relate to a 2s, $2p_{1/2}$, and $2p_{3/2}$ initial state, meaning L-edges are really denoted as L_I, L_{II}, and L_{III}, respectively. Where these absorption edges occur depends on the desired element. For example, the Au L_{III}-edge occurs at 11919 eV, while the Pd L_{III}-edge occurs at 3173 eV. These values differ according to Equation 1.2, where μ is proportional to Z^4. Once an XAS spectrum is obtained, it can be analyzed in terms of the XANES region and EXAFS region to determine the structural properties of the analyzed element. The specifics of these analyses will be given in detail below.

1.4.2.1 X-ray Absorption Near-Edge Structure

As mentioned in section 1.4.2, XANES is the region that is ~ 50 eV below and beyond the absorption edge. Analysis of XANES can give information on the oxidation state, coordination environment, band structures, and charge states of metal atoms in a sample.[131–133] This information garnered by XANES analysis is possible through comparison with known standards that are related to the element of interest. For example, the XANES region of Pd foil relative to an unknown Pd sample can be compared to discern differences in the oxidation state of Pd. Pd foil would have metallic Pd with an oxidation state of 0. If the sample is shifted to higher energies in the XANES region, this would indicate a higher oxidation state of Pd in the unknown sample. As discussed previously, the BE of an electron determines whether it will be ejected or not from the core orbital. If electrons are removed, the oxidation state is increased, and it becomes harder to eject a core

electron as the BE is increased. That is, more energy is required to eject the core electron, so a shift towards higher energy is typically seen with higher oxidation states. XANES is a useful qualitative tool in XAS, though more quantitative information such as coordination numbers (CNs) are desirable and can be modelled through an analysis of the EXAFS region.

1.4.2.2 Extended X-ray Absorption Fine Structure

The EXAFS region can provide information on the local atomic structure of a metal center. In the EXAFS region, a photoelectron has escaped the absorbing atom. This escaped photoelectron will then scatter off neighbouring atoms in the system, attenuating the absorption spectra that are produced. Essentially, EXAFS analysis allows one to discuss the radial distribution of atoms around an absorbing metal center through the fitting of a structural model to experimental EXAFS data.[132] In order to properly fit experimental EXAFS data, a good model must be constructed and fit to the data. When creating a model, good estimations on the coordination environment around the metal center and relative bond lengths must be used. Once a model is created, the experimental spectra can then be fit in terms of both k- and R-space. Figures 1.6A and B depict a general k-space and R-space spectrum for a Pd foil, respectively.

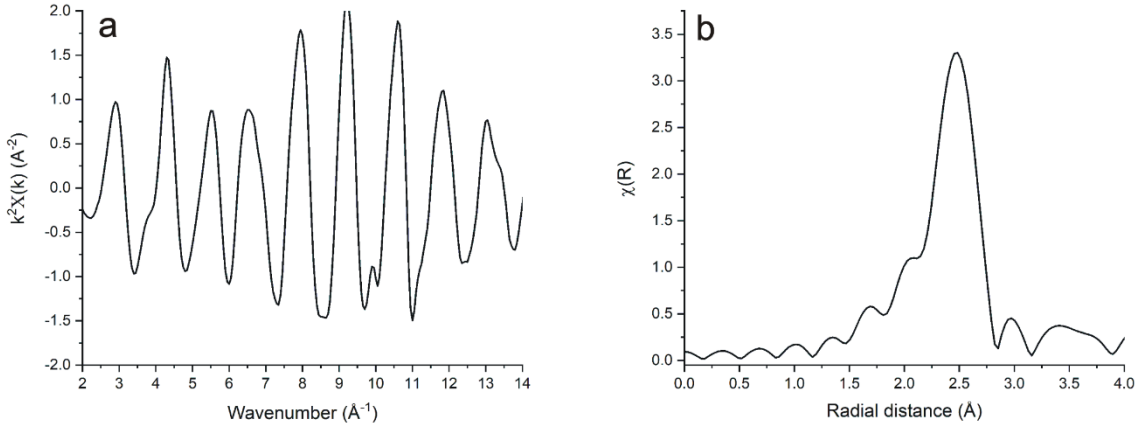

Figure 1.6 A) k-space and B) R-space at the Pd K-edge for Pd foil.

The k-space of a spectrum is the wavenumber of the photoelectron and is represented in Equation 1.3:

$$k = \sqrt{\frac{2m(E - E_0)}{\hbar^2}} \tag{1.3}$$

where m is the mass of the electron, E and E_0 are the measured absorption energy and absorption edge, respectively, and $\hbar^2$ is Planck's constant.[131] Generally, higher energy k-space data is enhanced by multiplying k by a power of k (k^2 and k^3 are common). This is done to enhance higher energy features that are generally quite important but have a weak signal in the non-weighted k-space spectrum.[132,133] R-space is simply a Fourier transform of k-space, though the details of a Fourier transform are not important to this discussion. In R-space, radial distributions of atoms around a metal center can be quantified by fitting the spectra with a model.

Once the experimental spectrum has been fit in k- and R-space, the CN, bond length (R), and the thermal disorder parameters (σ^2) and edge shift (E_o) can be quantified with errors. This information can give quantitative information on the local environment around the targeted metal center. An example of building a model and fitting k- and R-space data with it to pull out quantitative information about an unknown is shown by Balcha *et al.*[75] In this work, AuPd bimetallic NPs with different Au/Pd ratios were compared to monometallic Au and Pd NPs at the Pd K-edge and Au L_{III}-edge. Initially, k-space data from both edges were analyzed for the bimetallic samples at Au/Pd ratios of 1/3 and 1/1. High-quality fits were obtained, and EXAFS parameters such as CN and bond distances (R) were determined. Essentially, pure monometallic bulk Pd should have a Pd-Pd CN of around 12, while the introduction of Au into the system would decrease the Pd-Pd CN as Pd now as Au neighbours as well. EXAFS can be used to approximate

NP sizes using CN information, as shown by previous work in our group.[134] Work by Balcha and co-workers showed this, where pure Pd NPs had a Pd-Pd CN of 9.9 ± 0.5, and the bimetallic AuPd NPs showed Pd-Pd CNs of 8.3 ± 0.7 and 6.2 ± 1.1 for 1/3 and 1/1 Au/Pd NPs, respectively. Au-Au CNs were also obtained from analysis on the Au L_{III}-edge. Larger Au-Au CNs were seen for both bimetallic species, which showed that the Au must predominantly be in the core of NP, while Pd creates a shell on top. Similar ideas can be directly applied to the area of SACs, as many groups in the recent literature are starting to use EXAFS modelling as a way of determining whether metals are atomically dispersed on support surfaces.[53,58,67,92,93,121,135]

An example of using EXAFS fitting to determine the structural features of a catalyst is shown by Zhou *et al*.[92] In their work, Fe, Co, Ni, and Cu SACs supported on nitrogen-doped carbon were characterized by XAS at the K-edge for each metal. Through EXAFS fitting, it was determined that all of the catalysts contained single-atoms of each metal in an N-doped C matrix, with CNs for M-C (with M = Fe, Co, Ni, and Cu) of 1.0 or lower. The absence of an M-M CN suggests a single-atom structure. M-N CNs of around 3 were observed for each metal as well, indicating that the metal atoms are predominantly coordinated to N atoms in these catalysts.

1.5 Thesis Objectives

The field of single-atom catalysis is becoming more prominent as metal loadings in catalysts can be decreased without sacrificing catalytic activity or selectivity, improving the cost economy of the catalyst.[52,53,55,56,70,73,96,113,122,136] A plethora of work has gone into evaluating the catalytic ability of SACs, though the structure and stability of these catalysts are generally examined in detail. The main objective of this work is to evaluate the structure and stability of

bimetallic and monometallic quasi-homogeneous and heterogeneous SACs using XAS. In Chapter 2, different synthesis strategies are evaluated to produce quasi-homogeneous and heterogeneous Pd-based bimetallic and monometallic catalysts. It is paramount that these catalysts are thoroughly characterized using numerous techniques such as TEM, XPS, and XAS, with all the characterization work outlined in Chapters 3 and 4 for quasi-homogeneous AuPd, and heterogeneous Pd catalysts, respectively. An objective of this work is to evaluate the activity of bimetallic AuPd catalysts in the oxidation of crotyl alcohol, and whether the activity can be increased using SACs rather than non-SAC-bimetallic NPs and monometallic catalysts. Co- and sequential-reduction strategies towards designing AuPd catalysts will also be evaluated as to which reduction strategy is preferable for synthesizing single-atom structures. This work is outlined in Chapter 3. Another objective of this work is to evaluate the stability and activity of a heterogeneous Pd SAC in the hydrogenation of 2-methyl-3-butyn-2-ol relative to monometallic and bimetallic Pd catalysts. It is not evident from the literature if the single-atom structure of Pd-based heterogeneous catalysts is stable under hydrogenation conditions, i.e. does Pd remain in a single-atom state on the support surface during and after catalysis. XAS techniques will be used to evaluate heterogeneous Pd SACs before and after a hydrogenation reaction. This work is outlined in Chapter 4.

Chapter 2: Experimental Methods

2.1 Materials

Potassium tetrachloropalladate(II) (K_2PdCl_4, 98%, Sigma-Aldrich), gold(III) chloride trihydrate ($HAuCl_4 \cdot 3H_2O$, ≥99.9% trace metal basis, Sigma-Aldrich), polyvinylpyrrolidone (PVP, M.W. 58,000, Alfa Aesar), sodium borohydride ($NaBH_4$, 98%, Sigma-Aldrich), L-Ascorbic acid ($C_6H_8O_6$, reagent grade, crystalline, Sigma-Aldrich), aluminum oxide (Al_2O_3, pore size 58 Å, ~150 mesh, Sigma-Aldrich), dicyandiamide ($C_2H_4N_4$, 99%, Alfa Aesar), crotyl alcohol ($CH_3CH=CHCH_2OH$, mixture of cis and trans, Sigma-Aldrich), 2-methyl-3-butyn-2-ol (MBY, $HC\equiv CC(CH_3)_2OH$, 98%, Sigma-Aldrich), vinyl acetate (VA, $C_4H_6O_2$, stabilized for synthesis, Sigma-Aldrich), Acetone (Certified ACS, ≥99.5%, Fisher), methanol (CH_3OH, Certified ACS, ≥99.8%, Fisher), ethanol (CH_3CH_2OH, Reagent grade, Sigma-Aldrich), and ethyl acetate ($CH_3COOC_2H_5$, ACS reagent, ≥99.5%, Sigma-Aldrich) were used as received. Milli-Q (Millipore, Bedford, MA) deionized water (18 MΩ cm) was used throughout.

2.2 Synthesis of Au_xPd Catalysts

2.2.1 Co-reduction Synthesis of Single-Atom Au_xPd Catalysts

Co-reduced single-atom Au_xPd (x = 4, 3, 2, and 1) nanoparticles (NPs) were synthesized by modifying procedures from Tsunoyama *et al.*[137] and Balcha *et al.*[75] 1.0 g PVP (MW ~58,000) was dissolved in 5.8 mL H_2O in a 100-mL round-bottom flask (flask A) at room temperature (22 ^oC). The solution was then placed in an ice-bath and cooled to 0 ^oC. To this cooled solution, 6.2 mL K_2PdCl_4 (30 mM, 6.0 x 10^{-5} mol Pd) and 1, 2, 3, or 4 equiv. of $HAuCl_4 \cdot 3H_2O$ (9.0 x 10^{-5} mol Au to 3.6 x 10^{-4} mol Au) was added depending on the desired ratio of Pd/Au. In a separate 100-mL round-bottom flask (flask B), 1.0 g PVP (MW ~58,000) was dissolved in 6.0 mL H_2O and

cooled to 0 °C in an ice bath. Flask A was stirred at 800 rpm, while flask B was stirred at 1400 rpm, with both flasks in an ice bath. After 20 minutes of stirring, 2.0 mL of ice-cold $NaBH_4$ (5 equiv. to the amount of Au) was added to flask B, and both flasks left to stir for another 10 minutes. The stirring speed of flask A was increased to 1600 rpm, and flask B (containing the reducing agent) was added to flask A as quickly as possible. The solution in Flask A changed from a yellow-brown solution to a dark brown-black solution immediately after the solutions were mixed. This dark solution was then stirred for 30 minutes in an ice bath, followed by stirring at 30 minutes at room temperature (22 °C). Once the stirring was completed, the catalyst solution was placed in cellulose dialysis membranes with a molecular weight cutoff of 12,000 g/mol and dialyzed for 24 hours in 500 mL of deionized water without stirring. A final [Pd] = 3.0 mM was achieved, with the [Au] = 3.0 mM, 6.0 mM, 9.0 mM, and 12 mM depending on the Pd/Au ratio. It must be noted that a minute dilution occurred during dialysis, though the concentration of Pd is considered to be 3 mM throughout this work.

2.2.2 Sequential Reduction Synthesis of Core-Shell Au_xPd Catalysts

Sequentially reduced core-shell Au_xPd (x = 4, 3, 2, and 1) NPs were synthesized with slight modifications of literature protocols.[27] First, an Au NP seed solution was synthesized ([Au] = 18.2 mM), and then K_2PdCl_4 was reduced using ascorbic acid in the Au NP solution to give sequentially reduced Au_xPd.

Au NPs were synthesized as follows: 2.0 g PVP (MW ~58,000) was dissolved in a mixture of water/methanol (15 mL/16 mL) in a 100-mL round bottom flask (flask C). Flask C was placed in an ice bath and cooled to 0 °C before the addition of 473 mg $HAuCl_4 \cdot 3H_2O$ (6.0×10^{-4} mol Au). In another 100-mL round bottom flask (flask D), 1.0 g PVP (MW ~58,000) was dissolved in a

water/methanol mixture (3 mL/3 mL). Flask D was placed in an ice bath and cooled to 0 ^{o}C. For 20 minutes, flask C was stirred at 800 rpm, and flask D at 1400 rpm. After 20 minutes, 2.0 mL of ice-cold $NaBH_4$ (159 mg, 7 equiv. to Au) was added to flask D and stirred for a further 10 minutes at 1400 rpm. The stirring speed of flask C was increased to 1600 rpm, and the solution in flask D was added to flask C as quickly as possible. The solution changed from a yellow solution to a dark red solution upon $NaBH_4$ addition. This solution was left to stir in an ice bath for 30 minutes, following by stirring at room temperature (22 ^{o}C) for 30 minutes. The dark red solution of Au NPs was then dialyzed as detailed in section 2.2.1. After dialysis, the Au NP solution was concentrated by removing methanol to give an aqueous solution with a final [Au] of 18.2 mM. The methanol was removed by stirring the post-dialysis solution at 1200 rpm and heating it in a water bath to 40 ^{o}C under high vacuum conditions.

Sequentially reduced Au_xPd core-shell NPs were synthesized by mixing 1.0 g PVP (MW ~58,000) with 9.0 x 10^{-5} mol Pd (K_2PdCl_4) and 18.2 mM Au NPs so that the Au ratio to Pd was 1:1, 2:1, 3:1, or 4:1 (9.0 x 10^{-5} mol Au to 3.6 x 10^{-4} mol Au). This mixture was stirred at 800 rpm and cooled in an ice bath to 0 ^{o}C for 5 minutes before increasing the stir rate to 1600 rpm and adding 10 equiv. of ascorbic acid (equiv. with respect to the moles of Pd, 159 mg, 9.0 x 10^{-4} mol ascorbic acid) to reduce the Pd. The solution colour slowly changed from dark red to black after stirring the solution in ice at 1400 rpm for 1 hour. After all reactants were added, the final volume of the solution was adjusted to be 30.0 mL. The solution was dialyzed overnight, as detailed in section 2.2.1. The final solution had a [Pd] = 3.0 mM, with the [Au] = 3.0 mM, 6.0 mM, 9.0 mM, and 12 mM depending on the Pd/Au ratio.

2.3 Metal Deposition Method Towards Synthesizing a Pd/g-C_3N_4 Single-Atom Catalyst

Pd/g-C_3N_4 was synthesized following the work of Chen *et al.*[78] A graphitic carbon nitride (g-C_3N_4) support was first synthesized by loading 4.3 g dicyandiamide powder into two combustion boats and calcining the powder at 600 ^oC for 4 hours under minimal $N_{2(g)}$ flow (~ 10 mL/min) in a Thermo Scientific Lindberg TF55035A-1 furnace. The resulting yellow powder was collected from the combustion boats and transferred to a round-bottom flask for washing. The powder was washed with a water/ethanol mixture and collected using filter filtration with a final yield of 2.3 g. Once the g-C_3N_4 precursor powder was dry, Pd was deposited in the following manner. 200 mg of g-C_3N_4 was mixed with 30 mL H_2O in a 250 mL round-bottom flask. To this mixture, K_2PdCl_4 was added such that the weight percentage of Pd was 0.1%, 0.5%, or 2.0% (wt. % based off of 200. mg g-C_3N_4). The resulting Pd/g-C_3N_4 material was then stirred for 24 hours and either reduced with $NaBH_4$ (25 equiv. to Pd) or collected as-synthesized without the addition of $NaBH_4$. The reduced or non-reduced Pd/g-C_3N_4 catalyst was washed twice with copious amounts of a water/ethanol mixture and collected via filter filtration. The powder was then dried in a benchtop oven at 50 ^oC overnight.

2.4 Catalytic Oxidation of Crotyl Alcohol

The oxidation of crotyl alcohol was performed following previous literature protocols in Maclennan *et al.*[26] Co- and sequentially reduced Au_xPd samples, with [Pd] = 3.0 mM and varying [Au] depending on the Pd/Au ratio, were studied in this catalytic oxidation reaction. To a 50 mL 3-neck round-bottom flask, 5.0 mL of the catalyst solution was added. A condenser was then attached to the middle neck of the flask and the other two necks covered with septa. A needle was connected to one end of the flask and the tip placed into the catalyst solution in order to sparge the

solution with $O_{2(g)}$ during the reaction. The system was purged with $O_{2(g)}$ for 20 minutes before adding 250 equiv. of crotyl alcohol (0.32 mL, for a substrate:Pd ratio of 250:1) via a syringe needle. The reaction was then stirred at 1400 rpm for 3 hours at 22 ^{o}C. After the 3 hour reaction, 2.0 mL of the reaction mixture was collected in a vial and transferred to 2.0 mL of ethyl acetate. This was done by mixing the reaction mixture with ethyl acetate (1.0 mL per extraction) by shaking it vigorously in a vial, and then the contents were transferred to two 2.0 mL centrifugation tubes and centrifuged at 6000 rpm for 10 seconds. The top layer of the neat extract was collected for analysis, while the bottom water/catalyst layer was discarded. Conversion, selectivity, and turnover numbers for the reaction were obtained from gas chromatography (GC) using an FID detector (Agilent technologies 7890A) and an HP-Innowax capillary column. The ethyl acetate extract was used for GC-FID analysis. Two reactions were run for each Au_xPd sample with three injections per reaction.

The oxidation of crotyl alcohol was also performed in the absence of $O_{2(g)}$, using vinyl acetate as a sacrificial alkane.[59] For this reaction, 5.0 mL of the Au_xPd catalyst solution was delivered into a 100 mL round-bottom flask. 0.35 mL of vinyl acetate was then added, and the mixture stirred at 1400 rpm. After 2 minutes of stirring, 0.32 mL of crotyl alcohol was added (1:1 vinyl acetate:crotyl alcohol ratio), and the reaction was continued for 3 hours before GC-FID analysis. Product extraction was performed in the same way previously mentioned.

GC-FID calibration curves were run for this reaction using the starting substrate crotyl alcohol, and the three main products crotonaldehyde, 1-butanol, and 3-buten-1-ol. Six different concentrations were run for each reactant, with three injections performed at each concentration. Linear calibration curves were obtained for all species with R^2 values of ~ 0.99 for all systems.

2.5 Catalytic Hydrogenation of 2-methyl-3-butyn-2-ol

The catalytic hydrogenation of 2-methyl-3-butyn-2-ol (MBY) was performed in a similar manner to the oxidation of crotyl alcohol. Both co- and sequentially reduced Au_xPd, and Pd/g-C_3N_4 catalysts were evaluated in this hydrogenation reaction. Either 5 mL of the Au_xPd solution ([Pd] = 3.0 mM) or 10 mg of Pd/g-C_3N_4 and 5 mL H_2O was added into a 500 mL round-bottom flask. The flask was connected to a differential pressure manometer (Extech 407910: Heavy Duty Differential Pressure Manometer, 29 psi) to evaluate the change in pressure as the reaction progressed. The solution was purged under $H_{2(g)}$ for 20 minutes, followed by closing off the system under an H_2 atmosphere. For the co- or sequentially reduced Au_xPd NP catalysts, 250 equiv. MBY was added via a syringe (0.36 mL, substrate:Pd ratio =250:1). For the heterogeneous Pd/g-C_3N_4 powder, 0.10 mmol of MBY was used (0.10 mL, Pd:substrate ratio varied depending on weight percentage of Pd on g-C_3N_4). The reaction was run for 30 minutes, 1 hour, 1.5 hours, and 24 hours at 22 ^oC, while stirring at 1600 rpm. The product was extracted via the ethyl acetate by the same procedure used in Section 2.4. Conversion, selectivity, and turnover numbers were obtained by GC-FID using the same column previously mentioned. Reactions were run in duplicate with three injections per reaction. Calibration curves were run for this reaction using the starting substrate MBY, and the two products 2-methyl-3-buten-2-ol, and 2-methyl-2-butanol. Six different concentrations were run for each reactant, with three injections performed at each concentration. Calibration curves were linear, with R^2 values of ~ 0.99 in each case.

2.6 Characterization

UV–Vis spectra were obtained using a Varian Cary 50 Bio UV–Visible spectrophotometer with a scan range of 200 – 1000 nm and an optical path length of 1.0 cm. Transmission electron

micrographs (TEM) were taken with an HT7700 TEM operating at 100 kV. TEM grids were prepared by placing a few drops of catalyst in Milli-Q deionized water onto a lacey carbon TEM grid (Electron Microscopy Sciences). Particle sizes were calculated using the software ImageJ.[138] All X-ray Photoelectron Spectroscopy (XPS) measurements were collected using a Kratos (Manchester, UK) AXIS Supra system at the Saskatchewan Structural Sciences Centre (SSSC). This system is equipped with a 500 mm Rowland circle monochromated Al K-α (1486.6 eV) source and combined hemispherical analyzer (HSA) and spherical mirror analyzer (SMA). A spot size of hybrid slot (300x700) microns was used. All survey scan spectra were collected in the -5-1200 eV binding energy range in 1 eV steps with a pass energy of 160 eV. High-resolution scans of 2 regions were also conducted using 0.05 eV steps with a pass energy of 20 eV. An accelerating voltage of 15 keV and an emission current of 10 mA was used for the analysis. The XPS spectra were analyzed using the CasaXPS software program[139]. Powder X-ray diffraction measurements on g-C_3N_4 were collected using an Apex2 Kappa CCD diffractometer (40 kV, Brüker AXS) at the SSSC. A 2θ range of 5 – 90° with a step size of 0.02° was evaluated in continuous scanning mode.

The Hard X-ray Microanalysis beamline (HXMA) 061D-1 (energy range, 5 – 30 keV; resolution, 1 x 10^{-4} ΔE/E) and Biological X-ray Absorption Spectroscopy beamline (BioXAS) 07ID-2M (energy range, 5 – 32 keV; resolution, 5 x 10^{-5} ΔE/E) at the Canadian Light Source (CLS) were used for collecting X-ray absorption spectra (XANES and EXAFS) at the Pd K-edge and Au L_{III}-edge. The energy scan range for measurements on both beamlines was between -200 eV to +800 eV at each edge. Pd and Au foils were used for references at the Pd K-edge and Au L_{III}-edge, respectively. All measurements were conducted in both transmission and fluorescence modes at room temperature (22 ^{o}C), with Au_xPd samples loaded onto alumina at 2.0% by weight Pd (Au weight percentage varied with Pd/Au ratio) using an acetone precipitation method[140], and Pd/g-

C_3N_4 analyzed as-synthesized (with varying Pd weight percentages). These solid powders were placed into a Teflon sample holder and sealed with Kapton tape. XANES and EXAFS data analysis was performed using the software package IFEFFIT.[141] fcc bulk lattice parameters (i.e., first shell coordination numbers of 12) were used to fit the Pd and Au reference foil data and determine the amplitude reduction factor (S_o^2) for both foils. For the Au foil, S_o^2 was determined to be 0.90 and 0.88 on BioXAS and HXMA beamlines, respectively. For the Pd foil, S_o^2 was determined to be 0.82 on both BioXAS and HXMA. These S_o^2 values were fixed and used to determine the EXAFS parameters for all samples. The Soft X-ray Microcharacterization Beamline (SXRMB) 06B1-1 (energy range, 1.7 – 10 keV; resolution, 1.0 x 10^4 $\Delta E/E$) at the CLS was used for collecting XANES spectra at the Pd L_{III}-edge. SXRMB samples were prepared in two ways. Solid samples were loaded onto double-sided tape, and fluorescence data was collected under a helium atmosphere. Liquid samples were analyzed by loading solution into SPEX CertiPrep Disposable XRF X-Cell sample cups and covering the cup with a 4 µm ultralene window film. Data was collected in fluorescence mode.

Chapter 3: Selective Oxidation of Crotyl Alcohol by Quasi-Homogeneous Au_xPd Bimetallic Single-Atom Catalysts

3.1 Introduction

Alcohol oxidation reactions are important to organic synthesis and are used for a number of industrial applications.[26,27,117] Crotyl alcohol oxidation reactions have been studied by both our group and others to evaluate the activity and selectivity of metal catalysts in the production of crotonaldehyde using AuPd bimetallic nanoparticle (NP) catalysts.[26,27,65,74,75,112] These previous catalytic systems used by our group differ from the work in this chapter in terms of Au:Pd loadings and the dispersion of Pd within the Au NP matrix (*i.e.*, single-atom Pd in an Au NP matrix). Scheme 3.1 depicts the three major products that can be formed during this reaction. Crotonaldehyde is the oxidation product of interest, while the other two are side-products, formed by Pd-H species on the surface of Pd catalysts.[26,27,74,75] These side-products can theoretically be minimized by sparging the reaction mixture with $O_{2(g)}$ at moderate flow rates. Scheme 3.2 shows how $O_{2(g)}$ can be used to clean the catalyst surface, to rid it of Pd-H species, and therefore reducing side-product formation. To evaluate this system, we synthesized two morphologies of putative single-atom bimetallic Au_xPd catalysts using different reduction strategies, co- and sequential reduction, where the ratio of Au to Pd was manipulated from 4:1 to 1:1 Au:Pd.

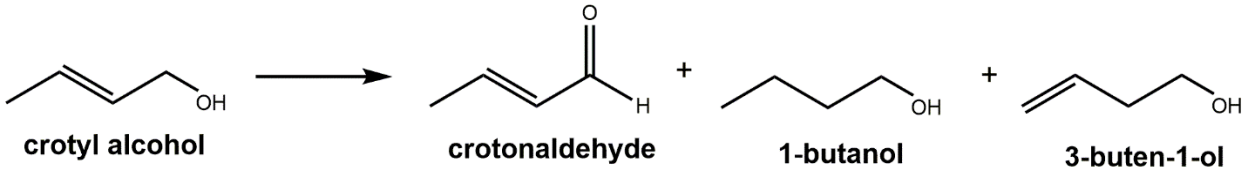

Scheme 3.1. The three main products observed in the oxidation of crotyl alcohol.

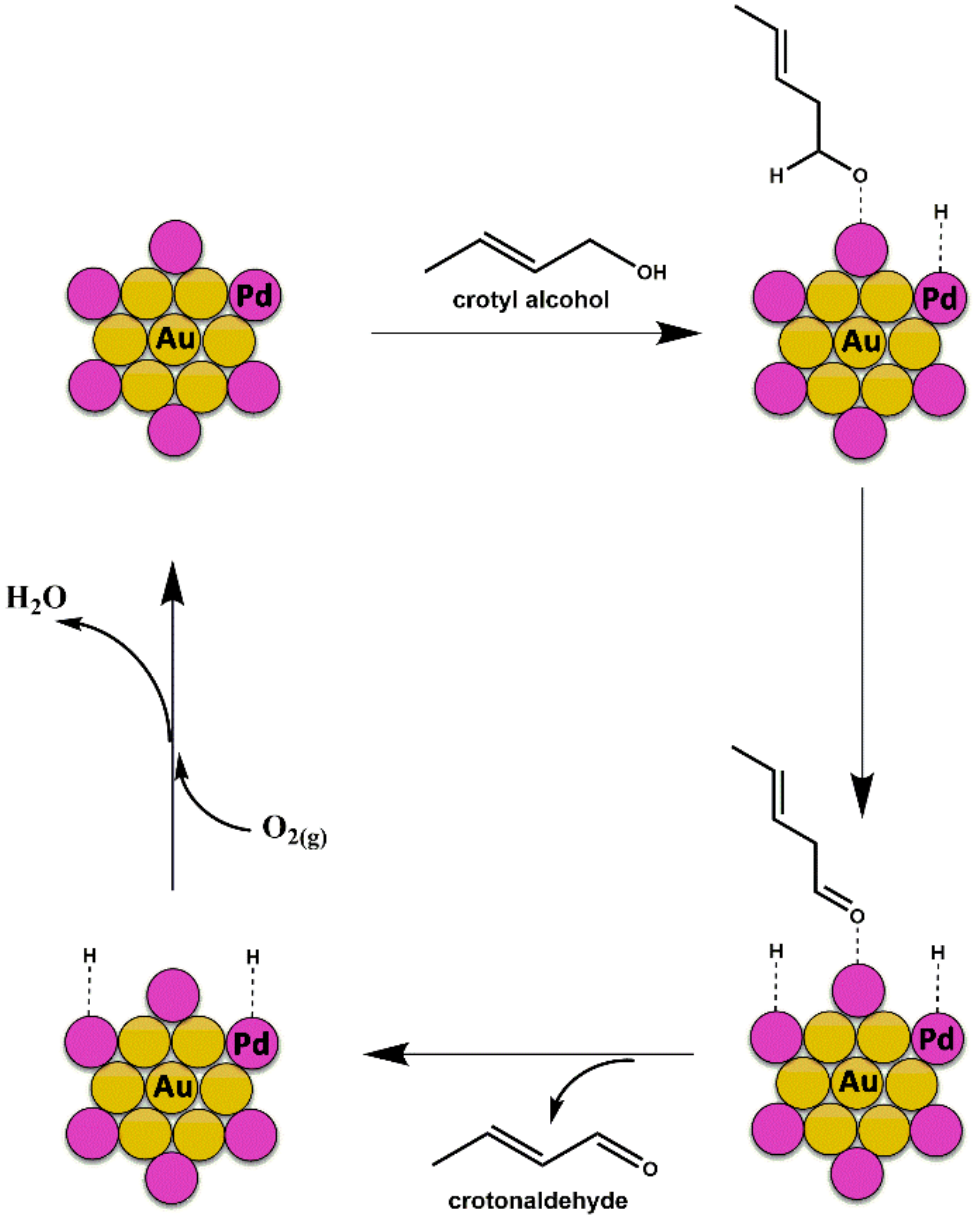

Scheme 3.2. The oxidation mechanism of crotyl alcohol to crotonaldehyde suggested by literature.[26,75] Adapted from Maclennan *et al.* [26].

3.2 Synthesis and Characterization of Co- and Seq-reduced Au_xPd Catalysts

The concentration of Pd was kept constant for the crotyl alcohol oxidation reactions at 3.0 mM. This value was chosen with the idea of evaluating these catalysts with XAS measurements at the CLS. In order to obtain high-quality data that exhibits a deep k-space, a higher concentration

of metals needed to be used. Therefore, the concentration of Pd was 3.0 mM, while the [Au] increased from 3.0 mM to 12 mM, depending on the Au:Pd ratio. Since a high metal concentration was used, the size of these catalysts was monitored by TEM to ensure that particle agglomeration and growth did not occur, while retaining relatively monodisperse particle sizes. Both co-reduction and sequential reduction strategies were used to obtain Au_xPd catalysts. The co-reduced Au_xPd catalysts were made by reducing an Au and Pd precursor in the presence of a stabilizer, while seq-reduced Au_xPd catalysts were made by first reducing an Au precursor to give Au NPs, then reducing a Pd precursor into the Au NP matrix. Figure 3.1 shows TEM images for each ratio of co- and seq-Au_xPd catalysts. A complete table of average particle sizes and standard deviations are listed in Table 3.1 based on measurements using ImageJ software.[138] For the co-Au_xPd catalysts, particle sizes vary between 3.0 and 3.5 nm. For the seq-Au_xPd catalysts, particle sizes vary between 3.6 and 4.9 nm. The particle sizes of each catalyst for both reduction methods are all within similar ranges, which would suggest that particle growth or agglomeration is not occurring, meaning these catalysts are stable under the reduction conditions during their synthesis. A smaller NP catalyst also ensures that the surface of the catalyst can be better studied using XAS, as a larger fraction of atoms is on the surface of the NPs.

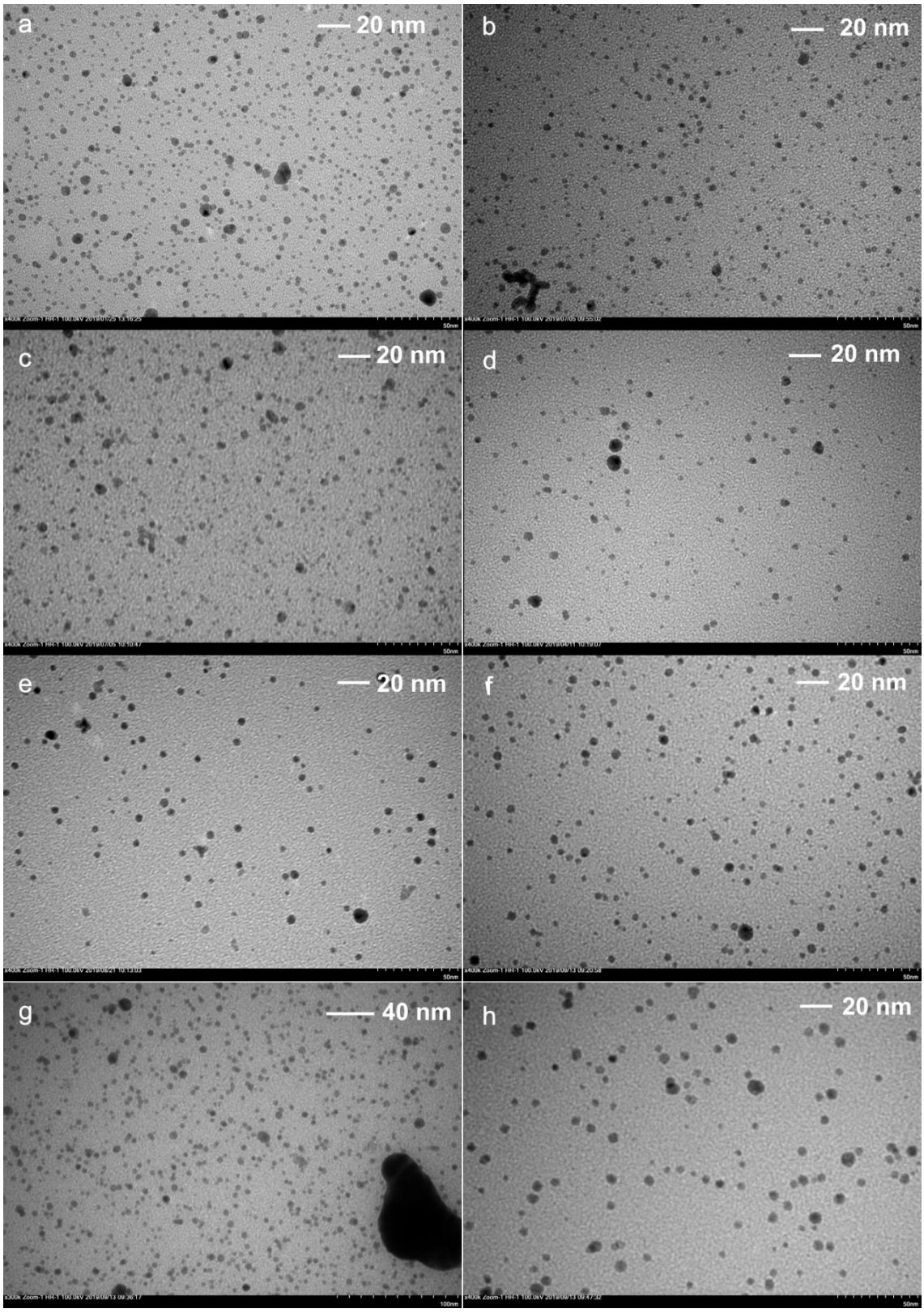

Figure 3.1. TEM images of a) co-Au_4Pd, b) co-Au_3Pd, c) co-Au_2Pd, d) co-AuPd, e) seq-Au_4Pd, f) seq-Au_3Pd, g) seq-Au_2Pd, and h) seq-AuPd catalysts.

Table 3.1. Average TEM particle sizes.

Catalyst	Particle size (nm)
co-Au_4Pd	3.1 ± 0.9
co-Au_3Pd	3.0 ± 1.1
co-Au_2Pd	3.6 ± 1.0
co-AuPd	3.5 ± 1.3
seq-Au_4Pd	3.6 ± 0.9
seq-Au_3Pd	3.7 ± 0.8
seq-Au_2Pd	4.0 ± 1.0
seq-AuPd	4.9 ± 1.3
Au NPs	3.6 ± 1.1

From Table 3.1, the average particle size for the Au NP seed solution is 3.6 ± 1.1 nm. As Pd is added into the system, the seq-Au_xPd particle sizes increase as the ratio of Au:Pd is decreased towards unity (*i.e.*, 1:1). Expected particle sizes can be calculated for the seq-Au_xPd catalysts using Equation 3.1:[63]

$$D = D_{core}\left(1 + \frac{V_{Pd}[Pd]}{V_{Au}[Au]}\right)^{\frac{1}{3}} \qquad 3.1$$

Where D_{core} is the particle size of the Au NPs, V_{Pd} is the molar volume of Pd, [Pd] is the concentration of Pd, V_{Au} is the molar volume of Au, and [Au] is the concentration of Au. For the seq-Au_xPd catalysts, particle sizes of 3.8, 3.9, 4.1, and 4.4 nm were predicted for Au:Pd ratios of 4:1, 3:1, 2:1, and 1:1, respectively. These values correspond well with the measured particle sizes in Table 4.1.

To prove that no secondary nucleation of Pd is occurring in the sequentially reduced system, a histogram of particle sizes is shown in Figure 3.2. Histograms were generated by plotting the raw count of binned particle sizes for each sequentially-reduced catalyst and Au NP, and then

fitting normal distribution curves to the raw data. For each sample, 70 particles were analyzed in a TEM image and their sizes measured using Image J software. The highest count of particle sizes occurs between 3 – 5 nm for each system, including the Au NPs. As Pd is introduced into the system (i.e., seq-Au_xPd), smaller particle sizes are not observed. This would indicate that a secondary nucleation event of new Pd NPs is not occurring, meaning the system is bimetallic, though the catalysts are characterized further below to show they are bimetallic.

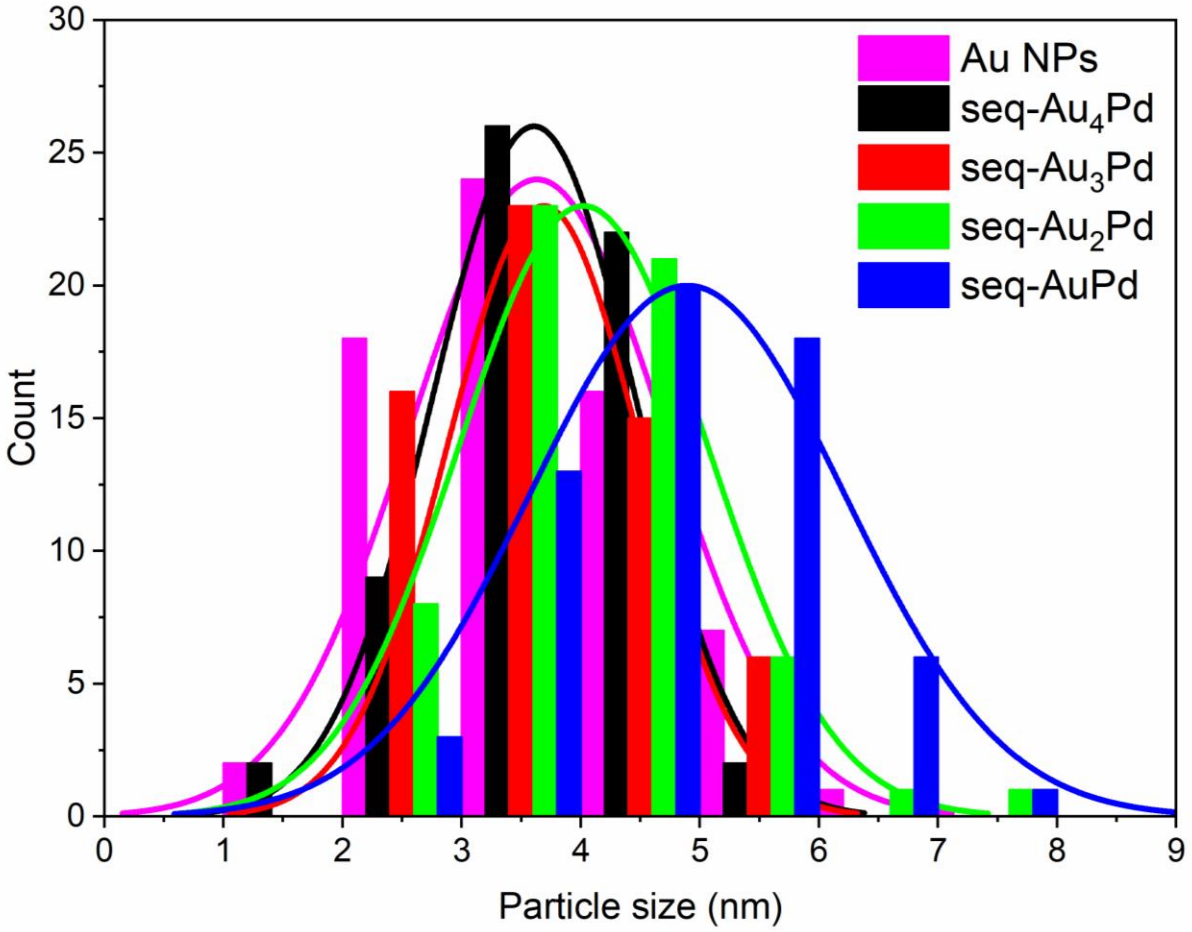

Figure 3.2. Distribution of particle sizes measured for Au NPs and all seq-Au_xPd catalyst.

Figure 3.3 contains UV-Vis spectra comparing Au NP seeds with the bimetallic Au_4Pd NP system after Pd is deposited on the surface, as well as the co-reduced Au_4Pd NP system. A typical absorption peak is seen ~ 550 nm for Au NPs caused by a phenomenon called surface plasmon

resonance (SPR).[11] In the case of co-Au_4Pd, no SPR peak is seen in the system. This would point towards Au-Pd interactions becoming more prominent, and a bimetallic alloy structure for the NPs.[75] On the other hand, for the seq-Au_4Pd catalyst, a slight peak can be seen at ~ 520 nm after the Pd reduction, which is dampened and shifted to lower energy compared to the pure Au NP plasmon peak. This indicates that Au-Au interactions are still prevalent in the system, though a dampening of the peak would indicate the addition of Pd into the system, likely on the surface of Au.[63,75,142]

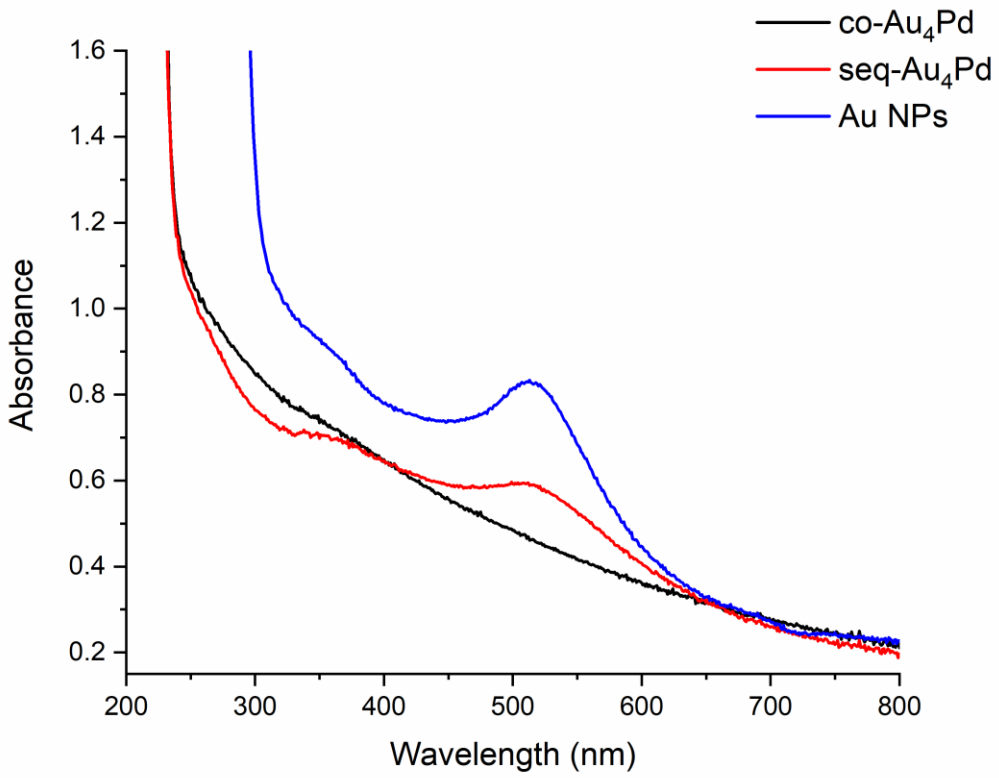

Figure 3.3. Comparison of UV-Vis spectra for co-Au_4Pd, seq-Au_4Pd, and Au NPs.

XPS studies were performed to characterize the surface composition of both co- and sequentially- reduced Au_4Pd catalysts. Figure 3.4 shows XPS spectra that were fit using Casa XPS software[139] for both co- and seq-Au_4Pd samples. High-resolution scans were obtained for Pd 3d and Au 4f peaks, which were then calibrated to a C 1s peak at 284.8 eV. In Figure 3.4a, Pd $3d_{5/2}$

and $3d_{3/2}$ peaks were fit for co-Au_4Pd, giving binding energies of 334.6 and 339.9 eV, respectively. These values correlate well with literature to metallic Pd(0) at 335.4 ± 0.9 eV and 340.2 ± 0.4 eV, respectively.[143] Figure 3.4b shows Au $4f_{7/2}$ and $4f_{5/2}$ peaks for co-Au_4Pd, with binding energies of 82.8 and 86.4 eV, respectively. These values also correlate well with metallic Au(0) in the literature at 83.2 and 86.9 eV, respectively.[144] Figure 3.4c shows seq-Au_4Pd fitted peaks for Pd $3d_{5/2}$ and $3d_{3/2}$ with binding energies of 334.6 and 339.9 eV, respectively. Again, these values correlate well to Pd(0) from the previously mentioned literature.[143] Lastly, Figure 3.4d shows seq-Au_4Pd fitted peaks for Au $4f_{7/2}$ and $4f_{5/2}$ with binding energies of 83.0 and 86.6 eV, respectively. These values correlate well with the previously mentioned literature.[144] From this analysis, it can be concluded that both Au and Pd are in their metallic forms on the surface of the catalyst, meaning a full reduction has occurred. The surface analysis also confirms that both metallic Au and Pd are present in the system, though more in-depth results from X-ray absorption spectroscopy (XAS) will be discussed below to provide further conclusions on the make-up of these catalysts at each Au:Pd ratio.

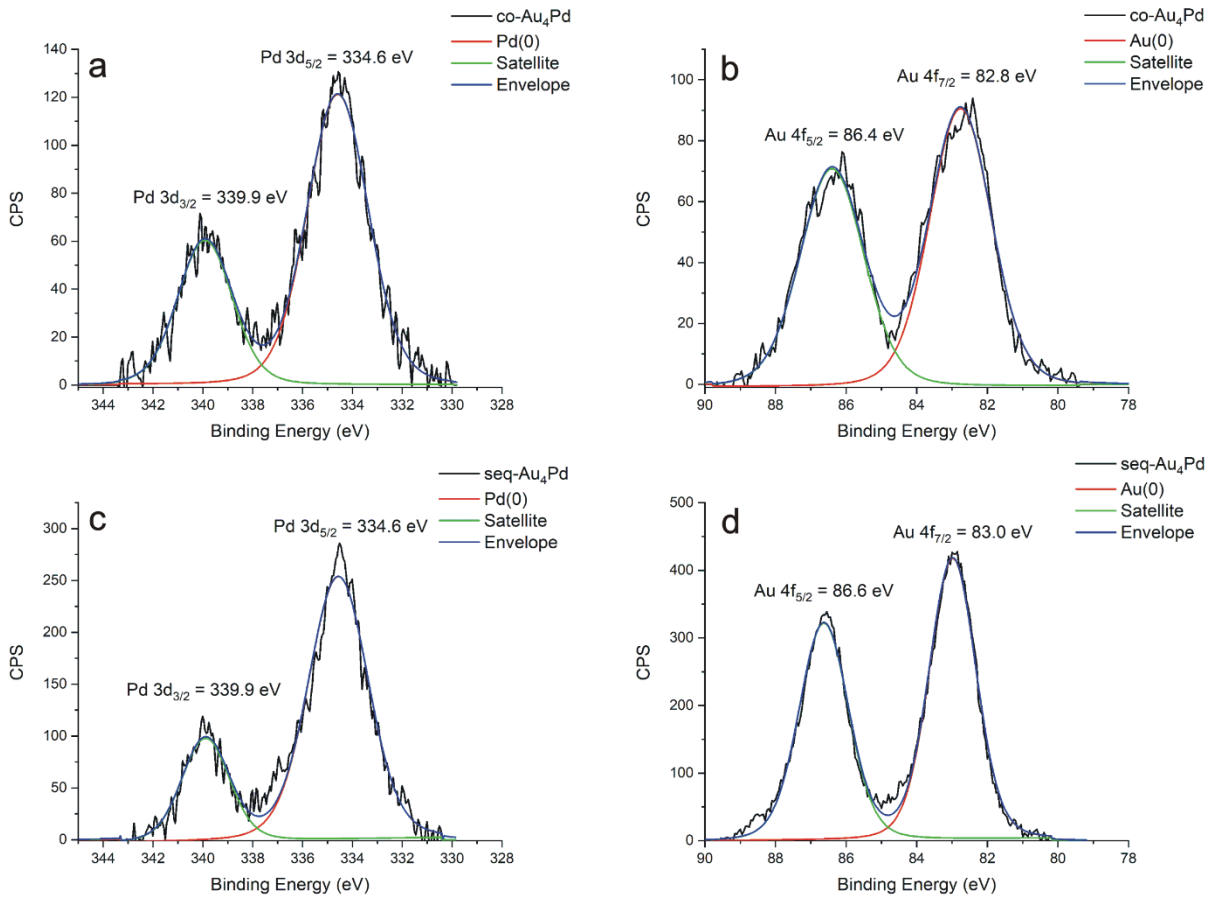

Figure 3.4. Fitted XPS spectra for (a) co-red Au_4Pd Pd 3d peak, (b) co-red Au_4Pd Au 4f peak, (c) seq-Au_4Pd Pd 3d peak, and (d) seq-Au_4Pd Au 4f peak.

Figure 3.5 contains XANES data at the Pd L_{III}-edge, showing a reference Pd foil compared to each ratio of co-Au_xPd catalysts. The white-line feature at 3173 eV is caused by the excitation of electrons from the $2p^{3/2}$ to 4d band in Pd.[145,146] The increase in white line intensity relative to Pd foil would suggest for each co-Au_xPd catalyst would indicate that electrons are being withdrawn from the 4d band of Pd by Au in the catalyst.[26,147,148] Also, a shift in the energy of the white line is observed for co-Au_xPd catalysts, further concluding that electrons are being withdrawn from the 4d band of Pd by Au. This allows one to conclude that our catalyst is a bimetallic AuPd system as these apparent shifts in white line intensity and energy correlate well with the literature from our group and others.[26,145,147,148]

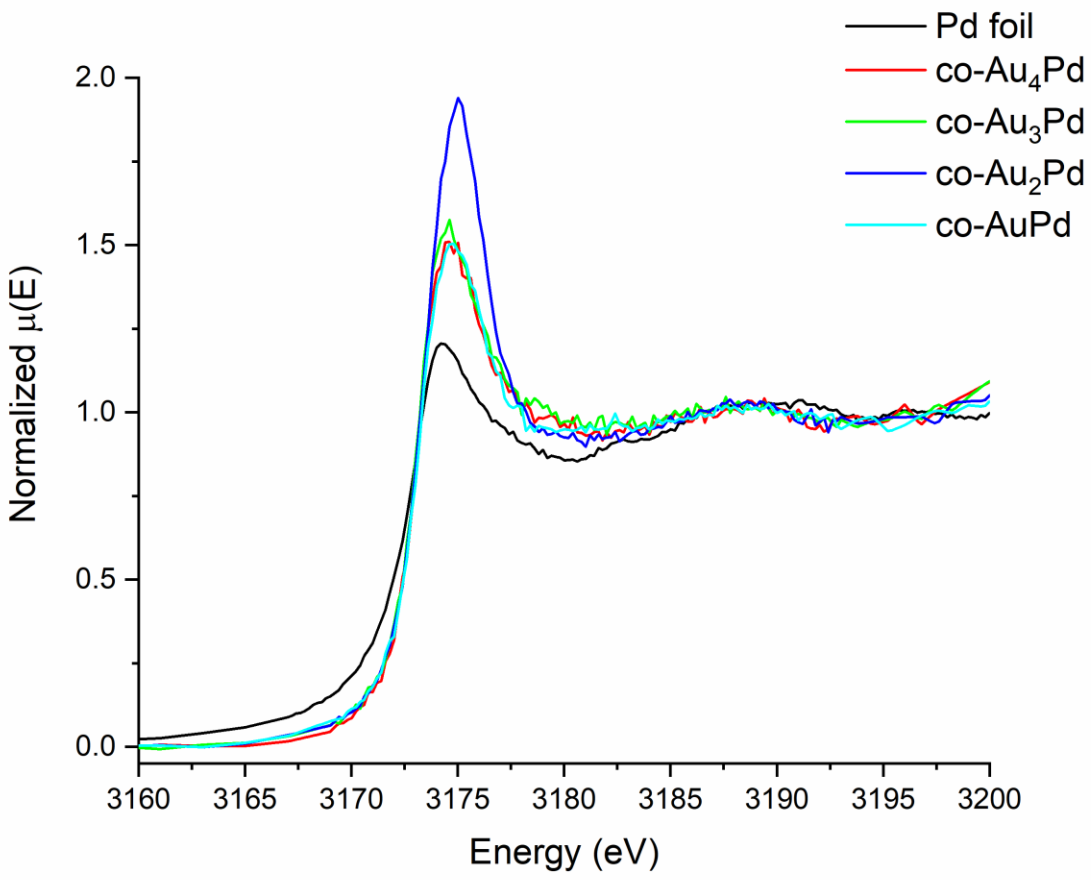

Figure 3.5. Pd L_{III}-edge XANES data on co-Au_xPd samples.

The bimetallic nature of both co- and sequentially- reduced Au_xPd catalysts was evaluated via XAS. Figure 3.6 contains XAS data collected on HXMA at the CLS for co-Au_xPd catalysts at each ratio of Au:Pd (i.e., 4:1, 3:1, 2:1, and 1:1). Figure 3.6a shows XANES spectra from the Pd K-edge for each co-Au_xPd catalyst. The Pd K-edge measures the transition from a 1s orbital to 5p orbital in Pd at the edge, with a white line observed near 24350 eV. Figure 3.6b shows XANES spectra from the Au L_{III}-edge for each co-Au_xPd catalyst. A shift to lower white line energy for the bimetallic samples relative to the Au foil would indicate an increase in electron density of the 5d band of Au.[75,147,149] This result, combined with results discussed from Figure 3.5, shows that Au is withdrawing electrons from Pd, increasing the electron density of the Au 5d band and

depleting electrons from the 4d band of Pd. Figures 3.6c and d contain k-space data collected on the Pd K-edge and Au L_{III}-edge, respectively, for all co-Au_xPd catalysts. A comparison between the bimetallic samples and monometallic reference foils shows an obvious shift in periodicity at both metal edges beyond a wavenumber of 4 $Å^{-1}$. This indicates there is a strong Au-Pd interaction in the co-Au_xPd catalysts, providing further proof that they are bimetallic.[103] The R-space data at the Pd K-edge and Au L_{III}-edge for co-Au_xPd catalysts are shown in Figures 3.6e and f. More intense peaks correlate to stronger interactions with the metal center being analyzed. In Figure 3.6e, the sharp peak seen slightly below 2.5 Å for the Pd reference foil is due to first shell Pd-Pd interactions, while significantly reduced Pd-M peak intensities are seen for the co-Au_xPd catalysts. This Pd-Pd R-value is shifted by ~ 0.3 Å as the data was not phase corrected in this figure. Fitted EXAFS spectra included in Appendix A are phase-corrected for both the Pd-Pd peak and Au-Au peak. Figure 3.6e suggests that a minute Pd-M interaction is observed for the co-reduced systems, indicating that Pd is likely located on the surface of Au. To quantitatively show this, a further discussion on the fitting of this data will be included later in Section 3.2. Figure 3.6f shows the R-space data at the Au L_{III}-edge for all co-reduced Au_xPd catalysts as well as Au foil. A strong first shell Au-Au interaction is seen slightly above 2.5 Å, while a strong Au-Pd interaction is observed slightly below 2.25 Å for each co-Au_xPd sample. Both values are slightly shifted from 2.83 and 2.80 Å, respectively, due to this data not being phase corrected. This strong Au-Pd interaction in the co-Au_xPd catalysts suggests that these systems are alloys. There is a qualitative shift in the co-reduced spectra versus the Au foil, further providing proof of strong Au-Pd interactions.

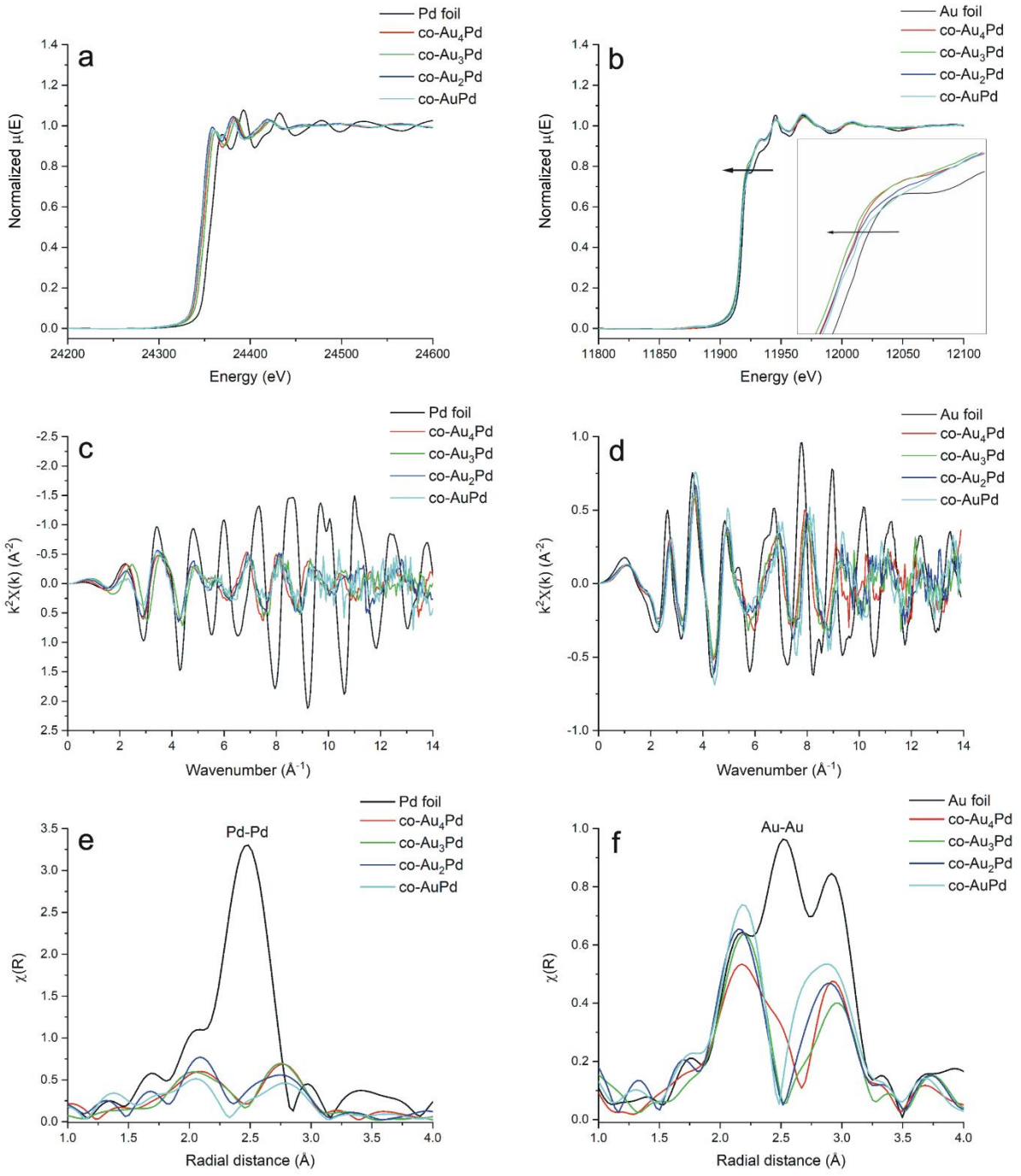

Figure 3.6. Synchrotron data for co-Au_xPd catalysts. (a) Pd K-edge XANES, (b) Au L_{III}-edge XANES, (c) Pd K-edge k-space, (d) Au L_{III}-edge k-space, (e) Pd K-edge R-space, and (f) Au L_{III}-edge R-space.

Figure 3.7 shows the XANES region at the Pd L_{III}-edge, where an increase in white line intensity at 3173 eV, as well as a shift in white line energy is observed. As discussed for the co-reduced system, an increase in white line intensity and shift to higher energy indicates electron withdrawal from the 4d band of Pd, though the shift is less dramatic for the seq-Au_xPd system.

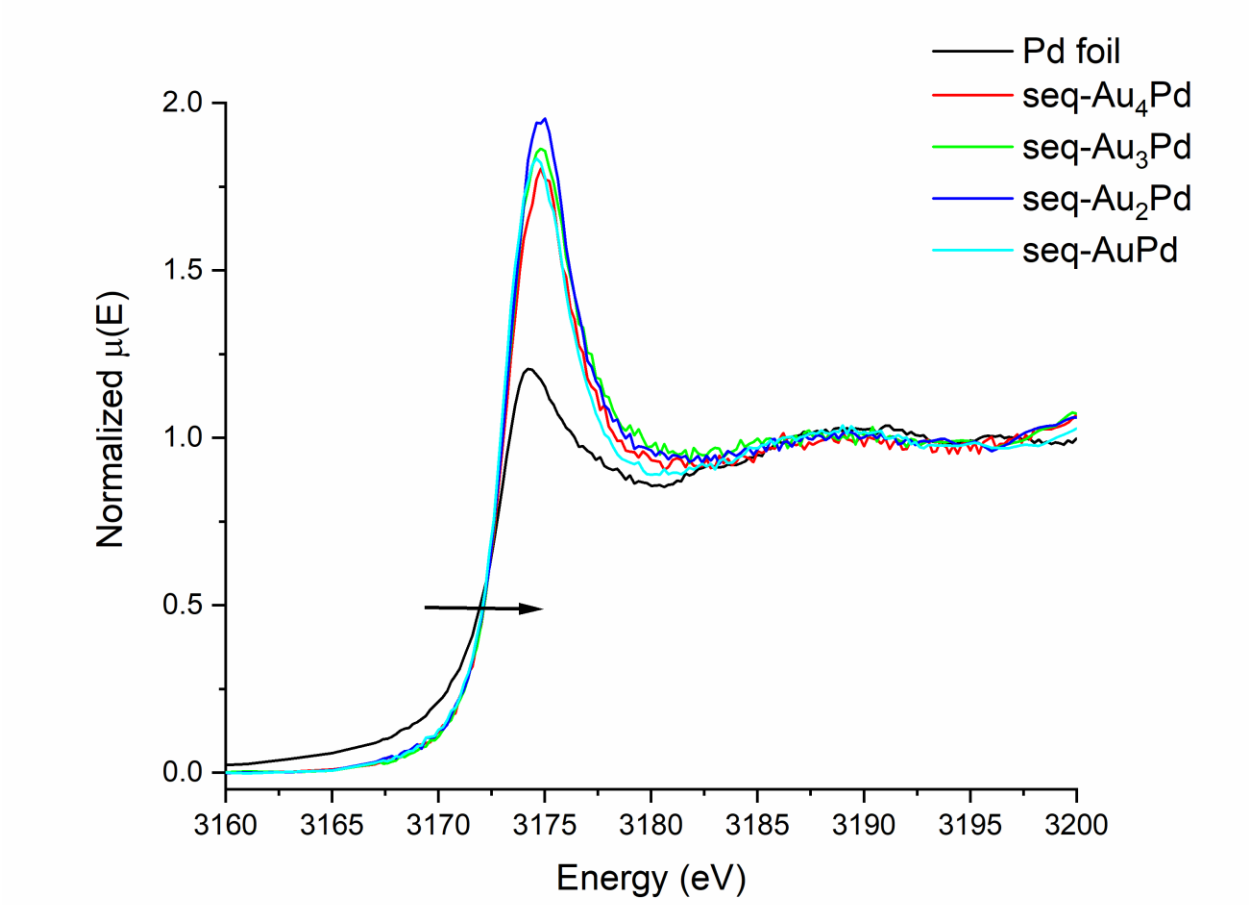

Figure 3.7. Pd L_{III}-edge XANES data for seq-Au_xPd samples.

Figure 3.8 contains XANES and EXAFS spectra collected on BioXAS and HXMA beamlines at the CLS for seq-Au_xPd catalysts at each ratio of Au:Pd (i.e., 4:1, 3:1, 2:1, and 1:1). Figure 3.8a shows XANES spectra from the Pd K-edge for all seq-Au_xPd catalysts. As previously mentioned, this is the transition from a 1s to 5p orbital for Pd, with a white line observed near 24350 eV. Figure 3.8b shows the Au L_{III}-edge XANES data for each seq-Au_xPd sample. No

obvious shift in the white line is observed, indicating that an increase in electron density in the 5d band of Au is not as prominent for these samples. Figures 3.8c and d show the k-space data collected on both metal edges for the seq-Au_xPd catalysts. No significant shifts in the periodicity of the wave are observed at either metal edge, though the amplitude of the wave at the Au L_{III}-edge correlates well with the Au reference foil, indicating that Au is in a near-bulk coordination environment. Again, this will be discussed near the end of Section 3.2, though a suggestion can be made that the seq-Au_xPd catalysts take on a core-shell morphology.[75] Figure 3.8e contains R-space data for each seq-Au_xPd catalyst at the Pd K-edge as well as a Pd reference foil. Like the co-reduced catalysts, an intense feature just below 2.5 Å is observed for the reference foil, though weak Pd-M interactions are observed for the seq-Au_xPd catalyst. There is a slight qualitative difference in peak shapes between the co- and seq-Au_xPd catalysts, which will be discussed in more detail below. Figure 3.8f shows the R-space data collected on the Au L_{III}-edge for each seq-Au_xPd catalyst and an Au reference foil. A strong Au-Au interaction is observed for the Au reference foil as well as the seq-Au_xPd catalysts just above 2.5 Å, indicating a near-bulk Au environment in the seq-Au_xPd catalysts.

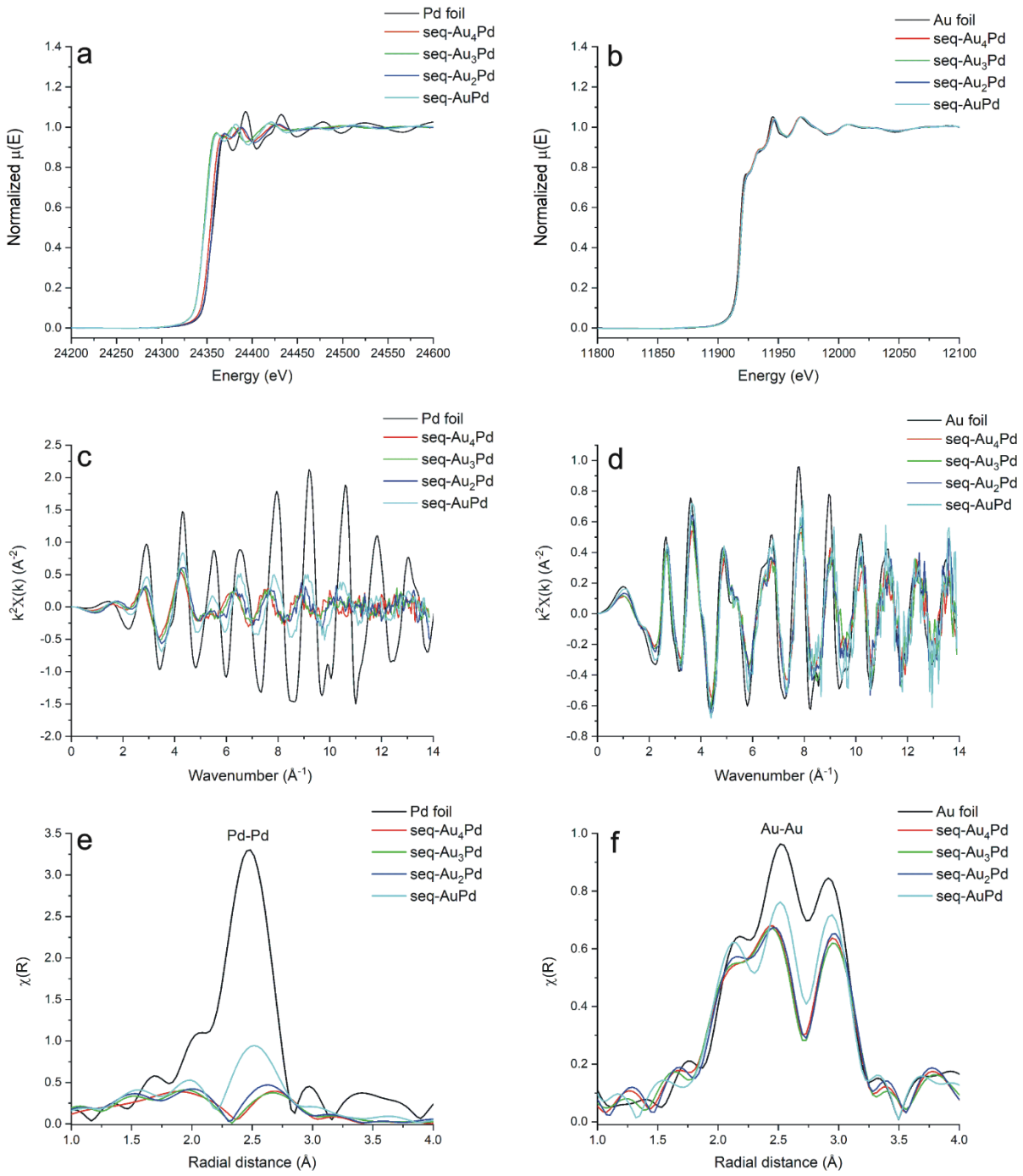

Figure 3.8. Synchrotron data for seq-Au_xPd catalysts. (a) Pd K-edge XANES from BioXAS, (b) Au L_{III}-edge XANES from BioXAS, (c) Pd K-edge k-space from HXMA, (d) Au L_{III}-edge k-space from BioXAS, (e) Pd K-edge R-space from HXMA, and (f) Au L_{III}-edge R-space from BioXAS.

Figure 3.9 provides an in-depth comparison on the Pd K-edge and Au L_{III}-edge between both co- and seq-Au_xPd catalysts at 4:1 and 1:1 Au:Pd ratios. In Figure 3.9a, R-space data at the Pd K-edge is shown for co- and seq-Au_xPd samples. As mentioned previously, the reduction in amplitude for the Pd-Pd just below 2.5 Å indicates that most of the Pd is on the surface of both catalysts. The low intensity of the Pd-Pd peak may indicate low coordination numbers (CNs) for the Pd-Pd bond in both catalysts, though the data must be fit using IFEFFIT software[141,150] to quantify this Pd-Pd interaction in terms of CNs. Small features can be seen slightly shifted to a higher radial distance for both catalysts, indicating Au-Pd bonding. A slightly further shift is seen for co-Au_4Pd and co-AuPd relative to the seq-Au_xPd catalysts, indicating that Pd may be in more of an isolated environment compared to the seq-Au_xPd catalysts and Pd-Pd CNs are lower for each ratio of Au:Pd, though further quantification was done through fitting the EXAFS data. In addition to the Pd K-edge R-space data, Figure 3.9b contains the Au L_{III}-edge R-space data for co- and sequentially- reduced Au_xPd catalysts at the same ratios. Qualitatively, there are nuanced differences in line shapes between the co- and seq-Au_xPd catalysts. The co-Au_xPd catalysts show a stronger Au-Pd interaction just below 2.25 Å than the seq-Au_xPd catalysts, indicating more Au-Pd mixing in the co-reduced catalysts. A more significant difference in the R-space data between co- and seq-Au_xPd is seen as the seq-Au_xPd takes on a very similar shape to the Au foil. This would qualitatively conclude that Au is in a near-bulk environment in the seq-Au_xPd catalyst with very strong Au-Au interactions, whereas a strong Au-Au interaction is not as prevalent in co-Au_xPd catalysts. Further quantitative conclusions can be made in regard to Pd-M and Au-M interactions by calculating CNs for Pd-Pd, Pd-Au, Au-Au, and Au-Pd interactions through EXAFS data fitting using the IFEFFIT software package.

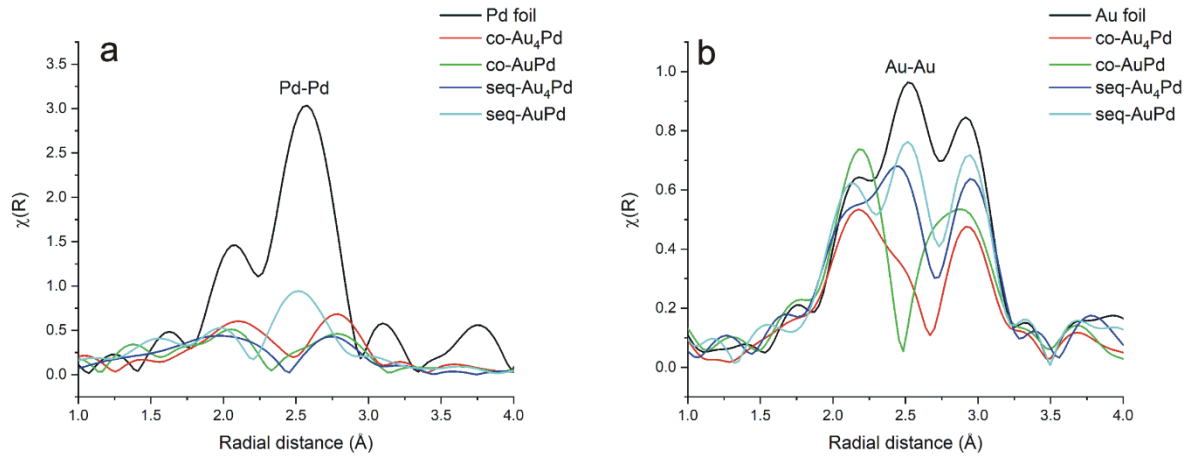

Figure 3.9. R-space data comparing co-Au$_x$Pd and seq-Au$_x$Pd catalysts at (a) Pd K-edge and (b) Au L_{III}-edge.

Simultaneous EXAFS fitting of both the Pd K-edge and Au L_{III} edge was done using AuPd alloy fcc models, and fitting results are shown in Tables 3.2 and 3.3. In Table 3.2 and 3.3, the element that comes first symbolizes the absorbing atom, while the second element symbolizes the neighbouring atom that scatters photoelectrons released by the absorbing atom (*e.g.* a PdAu interaction is a Pd absorbing atom with neighbouring first shell Au atoms). Both first shell Pd-Pd and Pd-Au interactions were quantified for all the co-reduced systems. For the Au$_4$Pd co-reduced NPs, the small CN of 1.2 ± 0.3 for the Pd-Pd interaction, along with a significant CN of 8.7 ± 0.8 for the Pd-Au interaction in the co-Au$_4$Pd system indicates that the Pd is nearly in a single-atom environment.[14,151] The co-reduced systems showed a slightly increased Pd-Pd CN of 2.5 ± 0.6, 2.5 ± 0.4, and 2.4 ± 1.2, for 3:1, 2:1, and 1:1 Au:Pd systems, respectively. This small increase in Pd-Pd CN signals the loss of single-atom Pd, with Pd starting to associate with neighbouring Pd atoms within the core or on the surface of Au. Notably, the Pd-Au CN begins to decrease with the Au:Pd ratio, going from 7.2 ± 0.9 down to 6.0 ± 2.4 for the 3:1 and 1:1 samples, respectively. Au-Au and Au-Pd first shell interactions were also quantified for all the co-reduced catalysts. A large CN of

7.1 ± 0.7 for the first shell Au-Au in the co-Au_4Pd catalyst was seen, indicating a large number of Au-Au neighbours. A low CN for Au-Pd in the co-Au_4Pd catalyst of 1.2 ± 0.3 was also quantified. As the ratio of Au:Pd decreases from 4:1 to 1:1, the CN of Au-Au decreases while the CN of Au-Pd increases. At an Au:Pd ratio of 1:1, the CN for Au-Au is 5.8 ± 0.9, and for Au-Pd it is 3.7 ± 0.6. To conclude, the nearest catalyst to a SAC is the co-Au_4Pd system, with all other ratios showing a trend towards AuPd catalysts with more contiguous Pd domains (*i.e.*, higher coordination between Pd atoms on the surface). The total Pd-M and Au-M CNs can be calculated by adding together Pd-Au with Pd-Pd, and Au-Pd with Au-Au, respectively, to confirm which metal is preferentially on the surface of the catalysts. As the ratio of Au:Pd decreases from 4:1 to 1:1, the total Pd-M CN decreases, while Au-M increases, indicating that Pd is initially predominantly on the surface of the 4:1 catalyst and not as predominantly on the surface as the ratio approaches unity. The bond distances listed are in good agreement with the literature[14,26] on bimetallic AuPd systems, with Pd-Pd distances at 2.79 ± 0.01 Å and Au-Au at 2.83 ± 0.01 Å. These values are slightly lower than the reference foils, which is typical for NP systems.[152,153]

Table 3.2. EXAFS Fitting Parameters for co-Au_xPd catalysts.

Catalyst	Bond	CN	R (Å)	σ^2 (Å^2)	E_0 (eV)	R-factor
co-Au_4Pd	Pd-Au	8.7 ± 0.8	2.80 ± 0.01	0.008 ± 0.001	-4.1 ± 0.6	0.008
	Pd-Pd	1.2 ± 0.3	2.79 ± 0.02	0.006 ± 0.002	-4.1 ± 0.6	
	Au-Au	7.1 ± 0.7	2.83 ± 0.01	0.009 ± 0.001	4.7 ± 0.4	
	Au-Pd	1.2 ± 0.3	2.80 ± 0.01	0.006 ± 0.002	4.7 ± 0.4	
co-Au_3Pd	Pd-Au	7.2 ± 0.9	2.80 ± 0.01	0.007 ± 0.001	-1.7 ± 0.4	0.016
	Pd-Pd	2.5 ± 0.6	2.79 ± 0.01	0.007 ± 0.002	-1.7 ± 0.4	
	Au-Au	6.3 ± 0.8	2.82 ± 0.01	0.008 ± 0.001	4.2 ± 0.5	
	Au-Pd	1.6 ± 0.3	2.80 ± 0.01	0.004 ± 0.001	4.2 ± 0.5	
co-Au_2Pd	Pd-Au	7.3 ± 0.9	2.80 ± 0.01	0.008 ± 0.002	-5.4 ± 0.4	0.007
	Pd-Pd	2.5 ± 0.4	2.79 ± 0.01	0.005 ± 0.001	-5.4 ± 0.4	
	Au-Au	6.5 ± 1.2	2.82 ± 0.01	0.009 ± 0.002	5.2 ± 0.6	
	Au-Pd	2.7 ± 0.5	2.80 ± 0.01	0.007 ± 0.001	5.2 ± 0.6	
co-AuPd	Pd-Au	6.0 ± 2.4	2.80 ± 0.01	0.008 ± 0.006	-6.2 ± 0.8	0.023
	Pd-Pd	2.4 ± 1.2	2.77 ± 0.03	0.005 ± 0.004	-6.2 ± 0.8	
	Au-Au	5.8 ± 0.9	2.82 ± 0.01	0.008 ± 0.001	6.1 ± 0.6	
	Au-Pd	3.7 ± 0.6	2.80 ± 0.01	0.007 ± 0.001	6.1 ± 0.6	

Compared to the co-reduced samples, slight increases in Pd-Pd CNs become apparent for the sequentially reduced samples. For the seq-Au_4Pd system, a CN of 1.6 ± 0.3 for Pd-Pd and 6.1 ± 0.5 for Pd-Au is observed. As the ratio of Au:Pd decreases, the CN of Pd-Pd increases while Pd-Au decreases, with the seq-AuPd system showing 6.0 ± 0.4 for Pd-Pd, and 3.2 ± 0.6 for Pd-Au. This is a similar trend observed in the co-Au_xPd catalysts. For seq-Au_4Pd, a large CN of 9.5 ± 0.4 for Au-Au is observed. The seq-AuPd catalyst has an Au-Au CN of 11.2 ± 1.1, resembling an Au fcc lattice (CN of 12). This is a sign that all Au atoms are in the interior of the NPs as Au:Pd ratios approach unity. The insignificant Au-Pd interaction for each sequentially reduced catalyst along

with large Pd-Pd and Au-Au interactions would indicate a core-shell morphology rather than an alloy.[26,75,152] Bond distances of ~ 2.70, ~ 2.73, and ~ 2.83 for Pd-Pd, Pd-Au, and Au-Au are in good agreement with previous work.[26] It should be noted that the energy shift parameter (E_0) is generally in the range of ± 10 eV, which is near the acceptable limit for modelling purposes. In Table 3.3, seq-Au_3Pd has an E_0 value slightly outside this range, though the errors are large enough that we can consider these values to be within the ± 10 eV range.

Table 3.3. EXAFS Fitting Parameters for seq-Au_xPd Catalysts.

Catalyst	Bond	CN	R (Å)	σ^2 (Å^2)	E_0 (eV)	R-factor
seq-Au_4Pd	Pd-Au	6.1 ± 0.5	2.73 ± 0.01	0.008 ± 0.001	-4.4 ± 0.7	0.017
	Pd-Pd	1.6 ± 0.3	2.68 ± 0.02	0.007 ± 0.002	-4.4 ± 0.7	
	Au-Au	9.5 ± 0.4	2.84 ± 0.01	0.010 ± 0.001	3.5 ± 0.6	
	Au-Pd	ND[1]	ND	ND	ND	
seq-Au_3Pd	Pd-Au	5.2 ± 0.5	2.74 ± 0.01	0.006 ± 0.001	-10.5 ± 0.8	0.020
	Pd-Pd	1.9 ± 0.3	2.69 ± 0.02	0.005 ± 0.002	-10.5 ± 0.8	
	Au-Au	9.5 ± 0.4	2.83 ± 0.01	0.009 ± 0.001	3.0 ± 0.6	
	Au-Pd	0.5 ± 0.1	2.74 ± 0.01	0.004 ± 0.001	3.0 ± 0.6	
seq-Au_2Pd	Pd-Au	5.7 ± 0.7	2.71 ± 0.01	0.011 ± 0.002	-2.9 ± 1.0	0.017
	Pd-Pd	3.3 ± 0.5	2.68 ± 0.02	0.008 ± 0.001	-2.9 ± 1.0	
	Au-Au	12.2 ± 0.7	2.84 ± 0.01	0.011 ± 0.001	4.9 ± 0.7	
	Au-Pd	ND	ND	ND	ND	
seq-AuPd	Pd-Au	3.2 ± 0.6	2.73 ± 0.02	0.008 ± 0.001	-7.6 ± 0.6	0.015
	Pd-Pd	6.0 ± 0.4	2.73 ± 0.01	0.009 ± 0.001	-7.6 ± 0.6	
	Au-Au	11.2 ± 1.1	2.84 ± 0.01	0.009 ± 0.001	4.6 ± 1.2	
	Au-Pd	ND	ND	ND	ND	

[1]ND = Not detected. This indicates that the errors in the EXAFS parameter were larger than the value obtained.

3.3 Selective Oxidation of Crotyl Alcohol Using Co- and Seq-reduced Au_xPd Catalysts

The co-reduced and sequentially reduced Au_xPd catalysts were monitored for the base-free, room-temperature selective oxidation of crotyl alcohol to evaluate the selectivity of each catalyst in producing crotonaldehyde. Table 3.4 shows the results from this reaction with co- and seq-reduced Au_xPd catalysts, as well as monometallic Au and Pd NPs. Both the monometallic NP catalysts showed < 10% conversion to the three products of the crotyl alcohol oxidation, crotonaldehyde, 1-butanol, and 3-buten-1-ol. Each bimetallic catalyst was more active (*i.e.*, higher conversion) and more selective to crotonaldehyde than either monometallic catalyst. The near single-atom co-Au_4Pd catalyst showed the greatest selectivity towards crotonaldehyde formation, at 77%. The largest conversion of 39 ± 9% was also observed for this catalyst. Notably, the selectivity towards crotonaldehyde decreased from the co-Au_4Pd catalyst to the co-AuPd system, which had a selectivity of 36%. This result would suggest that not only is the near SAC more selective, the selectivity is also related to the minimal Pd-Pd interactions (Table 3.2) that exist for this catalyst. An increase in side-product formation from the 3:1 catalyst down to 1:1 would indicate increased amounts of Pd-H species present in the catalyst (refer to Scheme 3.2), which is directly related to the increase in the CNs of Pd-Pd. As Pd forms continuous domains on the surface of Au, Pd-H species can be directly adjacent to other Pd catalytic sites, which adsorb the alkene, increasing the likelihood of side-products to form. Comparing the co-reduced catalyst to the sequentially reduced system, a decrease in aldehyde selectivity is observed for the sequentially reduced system at each Au:Pd ratio relative to the co-reduced system. The selectivity to the aldehyde decreases from 62% for seq-Au_4Pd down to 27% for seq-AuPd. Control reactions were performed to show that Au NPs are nearly inert for the oxidation reaction, while Pd NPs show high selectivity, but low conversion. The Pd NP control agrees with previous work.[145] Turnover

numbers (TONs) were generated based on the Pd:substrate ratio in our catalysts, which was 1:250, and average turnover frequencies (TOFs) were calculated by dividing the TON by 3 hours. The TON and TOF values can be compared to previous work by Maclennan *et al.*[26] using a seq-$AuPd_3$ catalyst, which used a higher ratio of Pd to Au than our work and different concentrations of each metal ([Pd] = 9.36 mM, [Au] = 3.13 mM). The same Pd:substrate ratio of 1:250 was used in this work, as well as similar reaction conditions at ambient temperature (25 ^{o}C). In this work, a conversion of 72.4% and selectivity of 62.8% was obtained, with a TON of 180. Our best catalyst, co-Au_4Pd, showed lower conversion (39 ± 9%) and better selectivity (77%), as well as a TON of 98 ± 22, which lower than the work by Maclennan *et al*. In this work, we were able to significantly reduce the amount of Pd in the catalyst, without hindering the selectivity greatly. Crotyl alcohol oxidations have been studied by our group and others, although typically using much harsher reaction (higher T, presence of bases) conditions which make comparisons difficult.[74,75,145]

Table 3.4. Crotyl Alcohol Oxidation Results[a].

Catalyst	Conversion	Compound	Selectivity	TON	TOF (h^{-1})
co-Au_4Pd	39 ± 9	Crotonaldehyde 1-butanol 3-buten-1-ol	77 ± 2 17 ± 1 6 ± 3	98 ± 22	33 ± 7
co-Au_3Pd	24 ± 2	Crotonaldehyde 1-butanol 3-buten-1-ol	65 ± 1 21 ± 1 15 ± 1	59 ± 4	20 ± 1
co-Au_2Pd	21 ± 3	Crotonaldehyde 1-butanol 3-buten-1-ol	67 ± 3 17 ± 1 17 ± 1	53 ± 8	18 ± 3
co-AuPd	10 ± 1	Crotonaldehyde 1-butanol 3-buten-1-ol	36 ± 1 22 ± 1 42 ± 1	24 ± 2	8 ± 1
seq-Au_4Pd	21 ± 1	Crotonaldehyde 1-butanol 3-buten-1-ol	62 ± 1 20 ± 1 18 ± 1	51 ± 1	17 ± 1
seq-Au_3Pd	15 ± 1	Crotonaldehyde 1-butanol 3-buten-1-ol	48 ± 4 25 ± 2 27 ± 2	37 ± 3	12 ± 1
seq-Au_2Pd	12 ± 1	Crotonaldehyde 1-butanol 3-buten-1-ol	35 ± 3 28 ± 1 37 ± 2	29 ± 2	10 ± 1
seq-AuPd	9 ± 1	Crotonaldehyde 1-butanol 3-buten-1-ol	27 ± 2 29 ± 1 45 ± 1	23 ± 1	8 ± 1
Au NP control[1]	0.3	Crotonaldehyde 1-butanol 3-buten-1-ol	0.0 100.0 0.0	0.8	0.3
Pd NP control[2]	7	Crotonaldehyde 1-butanol 3-buten-1-ol	70 22 8	17	6

[a]All reactions were run for 3 hours, stirring at 1400 rpm at room temperature (22 °C). The Pd:substrate ratio used for all reactions was 1:250 (5 mL of sample, 0.32 mL of crotyl alcohol). [Pd] = 3 mM for all Au_xPd catalysts. [1][Au] = 18.2 mM. [2][Pd] = 3 mM. TON was calculated by multiplying the substrate ratio to Pd (250:1) by the total conversion percentage. The average TOF was calculated by dividing the TON by 3 hours.

Table 3.5. Crotyl Alcohol Oxidation Results Using Vinyl Acetate[a]

Catalyst	Conversion	Compound	Selectivity	TON	TOF (h^{-1})
co-Au_4Pd	45 ± 1	Crotonaldehyde 1-butanol 3-buten-1-ol	88 ± 1 6.6 ± 0.3 5.9 ± 0.1	113 ± 2	38 ± 1
co-AuPd	17 ± 8	Crotonaldehyde 1-butanol 3-buten-1-ol	69 ± 4 13 ± 2 18 ± 2	42 ± 21	14 ± 7
seq-Au_4Pd	30 ± 1	Crotonaldehyde 1-butanol 3-buten-1-ol	78 ± 1 11 ± 1 11 ± 1	75 ± 1	25 ± 1
seq-AuPd	13 ± 1	Crotonaldehyde 1-butanol 3-buten-1-ol	50 ± 1 20 ± 1 30 ± 1	32 ± 1	11 ± 1
Vinyl acetate blank	3	Crotonaldehyde 1-butanol 3-buten-1-ol	13 80 7	6	2

[a]All reactions were run for 3 hours, stirring at 1400 rpm at room temperature (22 ^{o}C). The Pd:substrate ratio used for all reactions was 1:250 (5 mL of sample, 0.32 mL crotyl alcohol), while the substrate:VA ratio was kept at 1:1 (0.35 mL VA).

A comparison study was performed to show that vinyl acetate (VA) can also be used as a sacrificial alkane to "clean" the surface of the catalyst, similar to how $O_{2(g)}$ removes Pd-H species.[59] This study was done to prove that Pd-H species lead to the production of undesired side-products (Scheme 3.2), and to mitigate side-product formation to drive selectivity towards crotonaldehyde. The result of substituting $O_{2(g)}$ with VA is noted in Table 3.5. The co-Au_4Pd and co-AuPd catalysts were compared, as well as seq-Au_4Pd and seq-AuPd. For all four catalysts, increased conversions and selectivities are observed, with the selectivity for the co-Au_4Pd system increasing from 77 ± 2% using $O_{2(g)}$ to 88 ± 1% using VA. Similarly, for seq-Au_4Pd, the selectivity increased from 62 ± 1% to 78 ± 1% using $O_{2(g)}$ and VA, respectively. The reduction of side-product formation would indicate the VA cleans the surface of the catalyst by removing Pd-H species more efficiently than $O_{2(g)}$; this may be due to the fact that VA is in the same phase as the substrate, while O_2 has to diffuse into the liquid phase which sets up possible mass transfer limitations. The

significance of using VA is that it is inexpensive, small amounts of it are needed for the oxidation reaction (1:1 VA:substrate), and a pressurized system of oxygen gas is not needed. The use of VA also makes it easier to replicate the oxidation reaction, as everything can be thrown into "one-pot" and left to react for a desired amount of time.

3.4 Conclusion

To conclude Chapter 3, a series of co- and seq-reduced Au_xPd catalysts with x = 4, 3, 2, and 1 were synthesized, characterized, and evaluated as selective catalysts in the oxidation of crotyl alcohol to crotonaldehyde. TEM, XPS, and XAS analysis techniques confirmed that bimetallic co- and seq-Au_xPd systems were synthesized, with seq-Au_xPd showing a core-shell morphology. XPS spectra were fit to conclude that metallic Au and Pd were present in each catalyst system. Modelling of the EXAFS data confirmed that co-Au_4Pd and seq-Au_4Pd contained nearly isolated Pd atoms, while other ratios of co- and seq-Au_xPd catalysts showed more contiguous domains of Pd. Results from the oxidation of crotyl alcohol showed co-Au_4Pd was not only more active but also most selective in forming crotonaldehyde. As the ratio of Au:Pd decreased in both co- and seq-Au_xPd catalysts, activity and selectivity decreased. These catalysts were compared to monometallic Au and Pd NPs and were all more active and selective than the monometallic catalysts.

Chapter 4: Selective Hydrogenation of 2-methyl-3-butyn-2-ol by Single-Atom Heterogeneous and Quasi-Homogeneous Catalysts

4.1 Introduction

The hydrogenation of 2-methyl-3-butyn-2-ol (MBY) can be used to quantify the selectivity of numerous single-atom catalysts (SACs),[43,44,154,155] particularly Pd/g-C_3N_4 single-atom heterogeneous catalysts and bimetallic AuPd quasi-homogeneous SACs. Scheme 4.1 shows the two products of the hydrogenation of MBY, 2-methyl-3-buten-2-ol (MBE) and 2-methyl-2-butanol (MBA). These are the semi-hydrogenated and fully hydrogenated products, respectively. The purpose of using this system is to see if SACs can selectively synthesize the semi-hydrogenated product (MBE) over the fully hydrogenated product (MBA), as shown by the work of Li *et al.*[155] Their work was able to show that an $Au@Au_4Pd_1$ core-shell nanocube catalyst was able to successfully convert MBY to MBE at 98.4% conversion as well as selectively produce MBE at 90.2% selectivity (with only 9.80% of the substrate fully reducing to MBA). Li and co-workers deem this catalyst to be heterogeneous, though it differs from our Pd/g-C_3N_4 system in the fact that their nanocube is bimetallic, and ours contains only Pd. Their catalyst contained 0.4 nmol of Pd, while 0.1 mmol of MBY was used.

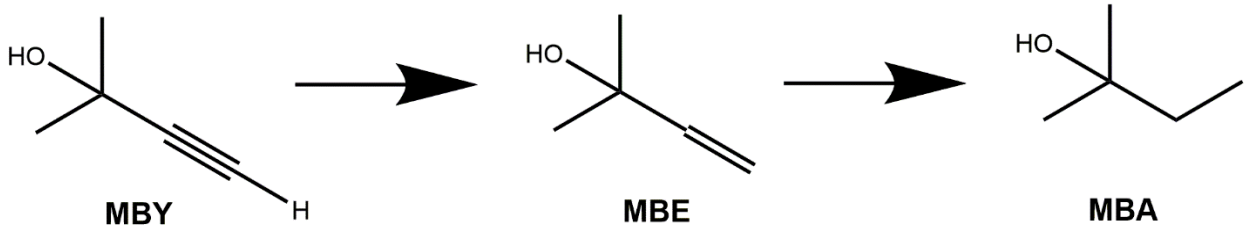

Scheme 4.1. Catalytic hydrogenation of MBY to MBE and MBA.

This Pd/g-C_3N_4 SAC was evaluated in the crotyl alcohol system from Chapter 3, though no activity could be seen, deeming the crotyl alcohol system to be structure-sensitive in the sense that a quasi-homogeneous bimetallic catalyst was active, while a heterogeneous system containing only Pd was not. For this hydrogenation system, both the heterogeneous Pd/g-C_3N_4 and quasi-homogeneous bimetallic Au_zPd systems were evaluated to see whether either catalytic system exhibited structure-sensitive catalytic behaviour in terms of selectively producing MBE with minimal MBA production.

4.2 Synthesis and Characterization of Pd/g-C_3N_4 Catalysts

Pd/g-C_3N_4 catalysts were made by first synthesizing the g-C_3N_4 support material through a polymerization reaction of dicyandiamide at 600 ^oC under moderate $N_{2(g)}$ flow. Once the support was made, Pd was deposited on g-C_3N_4 by mixing the support with K_2PdCl_4 in water for 24 hours. K_2PdCl_4 was added such that the weight percentage of Pd on g-C_3N_4 was 0.1%, 0.5%, and 2.0%. After the thorough mixing of the support and Pd precursor, Pd was either reduced with $NaBH_4$ or not reduced at all. The support was collected via filtration and dried in an oven at 50 ^oC overnight to give xPd/g-C_3N_4, where x = 0.1, 0.5, and 2.0% Pd. Figure 4.1a shows a typical TEM image of the g-C_3N_4 support material without any Pd deposition, while Figure 4.1b shows the pXRD spectra of the same support material. The TEM image shows a powdered solid on the micrometre scale, while the pXRD pattern depicts a sharp feature at 27.5° 2θ, which is representative of the (002) plane of g-C_3N_4. The peak at 27.5° 2θ indicates graphite-like layer stacking of the g-C_3N_4 material.[78] Both the TEM image and the pXRD spectrum compare nicely to literature work done on the same support material, g-C_3N_4[78], with the (002) peak occurring at 27.3° 2θ.

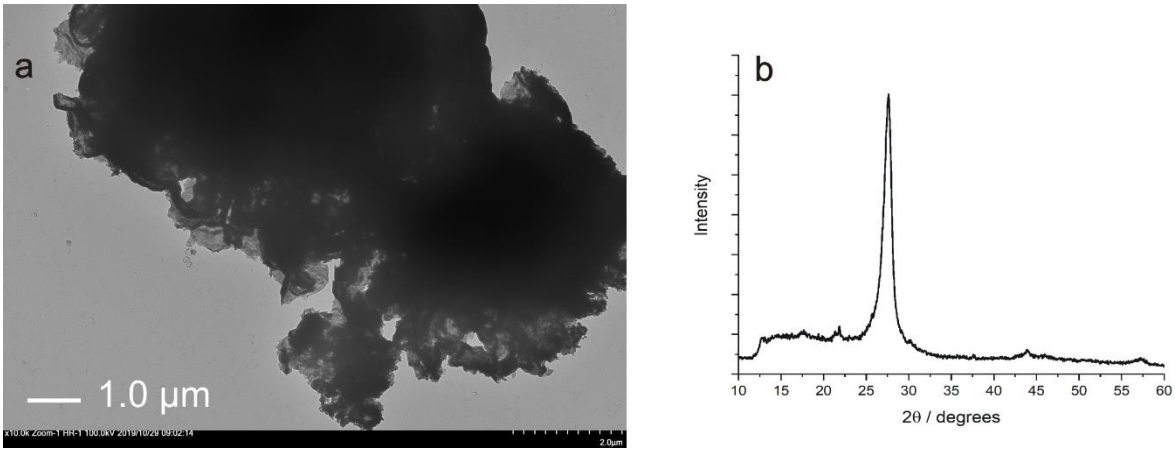

Figure 4.1. a) A TEM image of g-C_3N_4 and b) pXRD pattern of the g-C_3N_4 sample.

Figure 4.2a shows a TEM image of an as-synthesized Pd/g-C_3N_4 catalyst (*i.e.*, Pd was not reduced with $NaBH_4$ during the synthesis). Contrasting this is Figure 4.2b, where Pd was reduced with $NaBH_4$ in a g-C_3N_4 matrix. A noticeable difference can be observed where small Pd nanoparticles can be seen on the g-C_3N_4 support when Pd is reduced in the system. The average particle size calculated for the particles seen in Figure 4.2b is 4.7 ± 1.6 nm. Particle sizes were calculated using ImageJ software.[138] The non-reduced Pd/g-C_3N_4 does not show any small Pd particles in the TEM, resembling the image seen in Figure 4.1a.

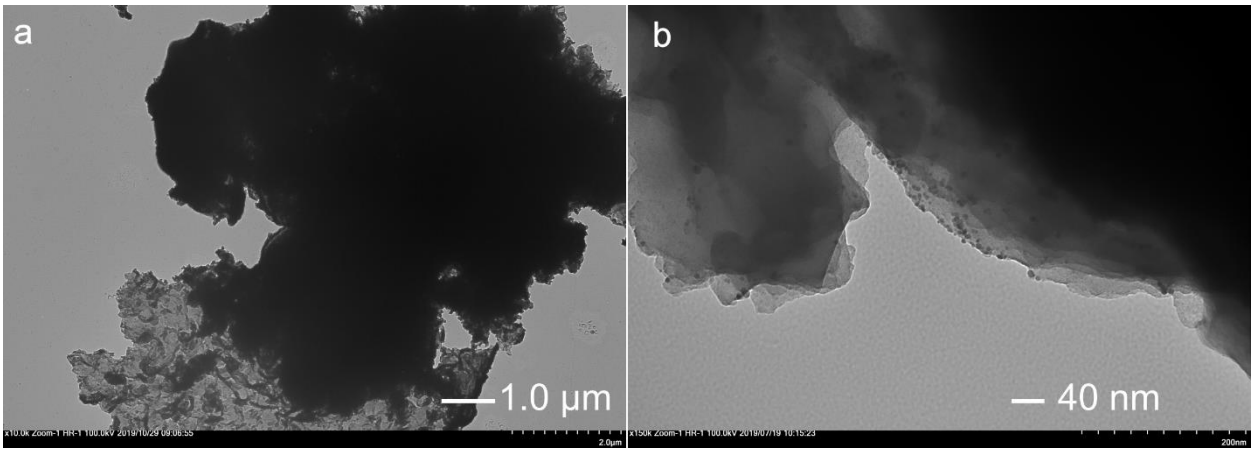

Figure 4.2. a) A TEM image of a 2.0% Pd/g-C_3N_4 (as-synthesized), and b) A TEM image of 2.0% Pd/g-C_3N_4 (reduced).

Figure 4.3 shows the fitted XPS spectra of both the as-synthesized and reduced Pd/g-C_3N_4 catalysts. XPS spectra were fit using CasaXPS software.[139] Figure 4.3a shows the fitted XPS spectrum for the as-synthesized 2.0% Pd/g-C_3N_4 catalyst. The binding energies of the Pd $3d_{5/2}$ and Pd $3d_{3/2}$ peaks occur at 337.8 eV and 343.0 eV, respectively, which are indicative of a Pd(II) species[143]. The Pd $3d_{5/2}$ peak compares well with literature at 337.9 ± 0.2 eV for a Pd(II) species ($PdCl_2$), and the Pd $3d_{5/2}$ and $3d_{3/2}$ peaks are separated by 5.2 eV, comparing well to a literature value of 5.31 ± 0.12 eV.[143] As this catalyst was not reduced, it would be expected that Pd would have an oxidation state of +2 since the precursor, K_2PdCl_4, was used in the synthesis. The Pd $3d_{5/2}$ peak is not completely Gaussian, indicating that another species may be present. From comparison with literature binding energies, we believe this small feature to be PdO, though this species could not be fit for both the $3d_{5/2}$ and $3d_{3/2}$ peaks as the intensity of the peak was too low. PdO is seen at 336.4 ± 0.7 eV according to literature,[143] and a small feature can be seen at ~336 eV in our data. Figure 4.3b shows the fitted XPS spectrum for a 2.0% Pd/g-C_3N_4 catalyst reduced by $NaBH_4$. The binding energies for the Pd $3d_{5/2}$ and $3d_{3/2}$ peaks are seen at 337.2 and 342.4 eV, respectively. These values are slightly shifted to lower binding energy than the as-synthesized catalyst and compare well to the literature value of a PdO peak at 336.4 ± 0.7 eV.[143] Again, a non-Gaussian peak for the reduced catalyst is observed. The intensity of the feature at ~335 eV was too low in intensity to fit for both the $3d_{5/2}$ and $3d_{3/2}$ peaks but correlates well with a literature value of 335.4 ± 0.9 eV for a Pd(0) species.[143] Since $NaBH_4$ was used in the synthesis to reduce Pd(II), we can postulate that this non-Gaussian feature at ~335 eV is indicative of Pd(0). The Pd $3d_{5/2}$ and $3d_{3/2}$ peaks are separated by 5.2 eV, which compares well with the literature value for the doublet separation at 5.31 ± 0.12 eV.[143]

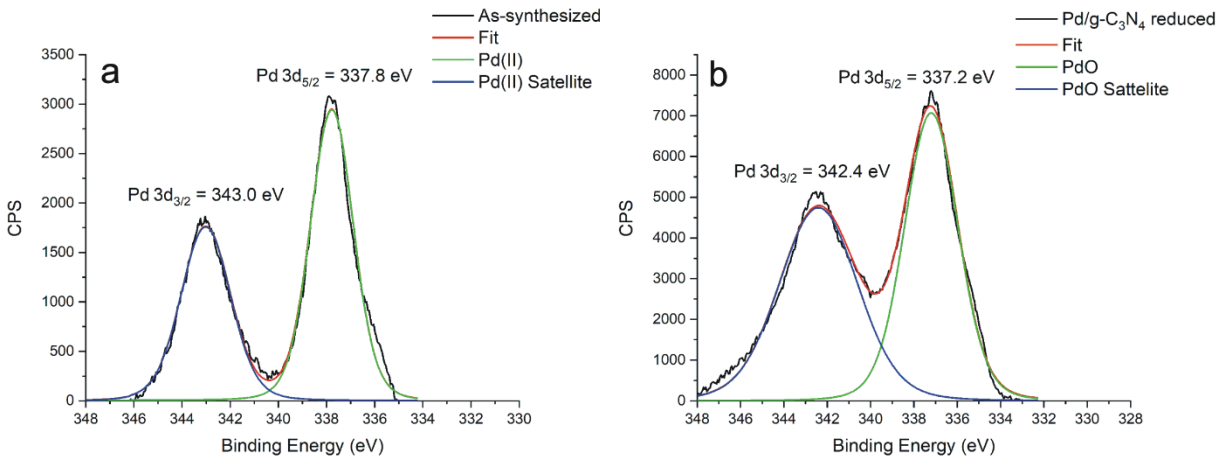

Figure 4.3. Fitted XPS spectra for a) as-synthesized and b) reduced 2.0% Pd/g-C_3N_4 catalysts.

Figure 4.4 shows XANES spectra from the Pd L_{III}-edge ($2p^{3/2}$ to 4d transition) on SXRMB at the CLS of the 2.0% Pd/g-C_3N_4 catalyst that is not reduced, reduced under H_2(g) (post-hydrogenation), and reduced using $NaBH_4$. The decreasing white line intensity at *ca.* 3175 eV for samples that have been reduced suggests that some Pd reduction is occurring both in the presence of $NaBH_4$ and H_2(g), which is consistent with XPS data above. However, the reduction is only partial, as the white line intensity is still significantly higher than the Pd nanoparticle standard. This is consistent with the XPS analysis above. An interesting observation of this analysis is the as-synthesized, non-reduced 2.0% Pd/g-C_3N_4 catalyst showed some reduction under hydrogenation reaction conditions.

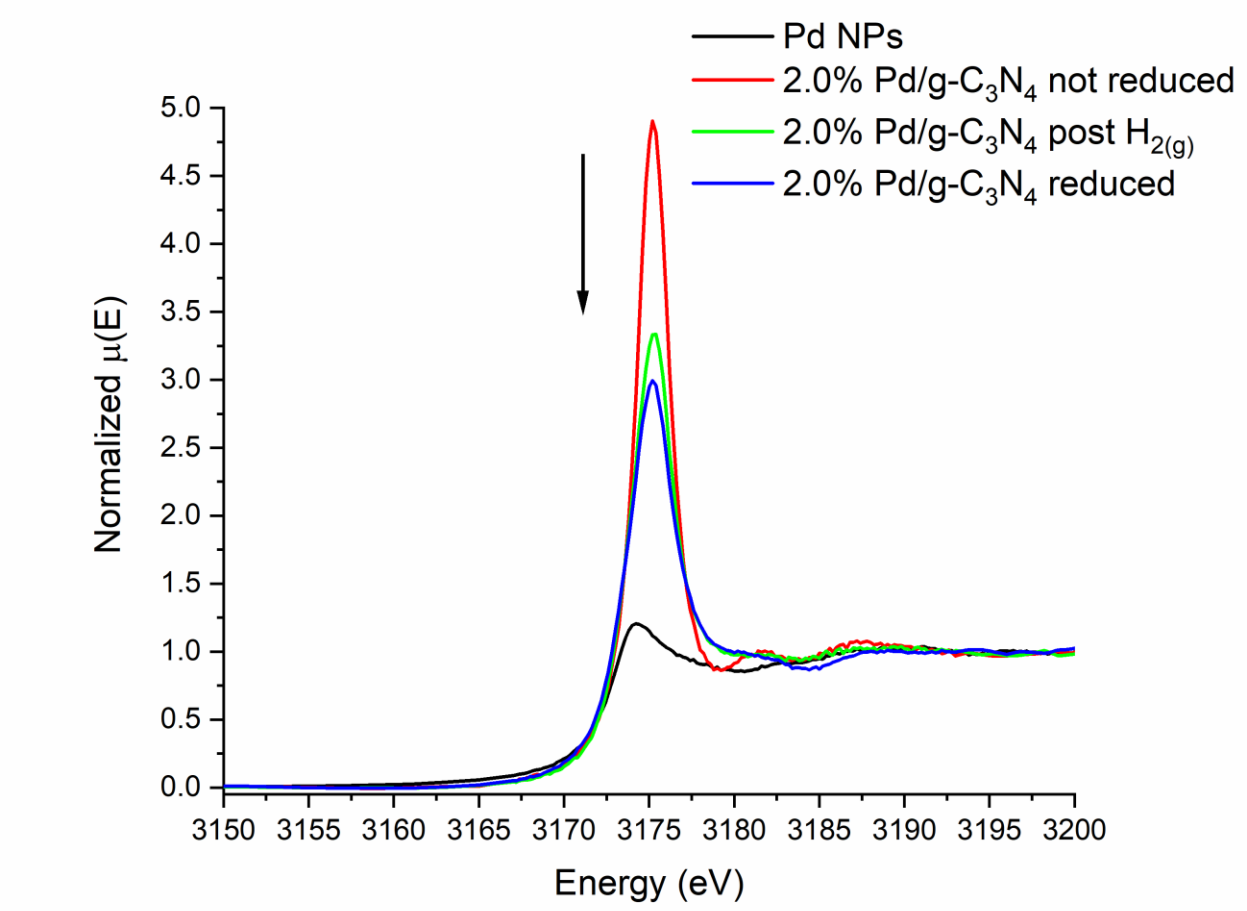

Figure 4.4. XANES data on the Pd L_{III}-edge for as-synthesized, post $H_{2(g)}$ treatment, and reduced 2.0% Pd/g-C_3N_4 catalysts.

Figure 4.5a shows k-space data from each sample compared to the k-space of Pd foil at the Pd K-edge on both the HXMA and BioXAS beamlines. The k-space data for the reduced samples appear to have similar periodicity with the Pd foil, albeit with much-depressed amplitudes, while the non-reduced sample has significantly different periodicity. This suggests that some Pd reduction to Pd clusters and/or nanoparticles may be occurring upon reduction. Figure 4.5b shows the R-space EXAFS data for each sample as well as Pd foil. As expected, the reduced samples show a noticeable Pd-Pd interaction and Pd-N interaction around 2.5 Å and 1.6 Å, respectively, while a Pd-Pd peak cannot be seen for the non-reduced system. The very low intensity of the Pd-

Pd peak is indicative of very small clusters of Pd. This information further confirms that the non-reduced sample contains minimal amounts of metallic Pd in a g-C_3N_4 matrix, while the reduction of Pd creates metallic Pd species on g-C_3N_4. This R-space data was further quantified by fitting with IFEFFIT software using the program Artemis[141] using a Pd fcc model and a simple Pd-N single-shell model. All fitting for Pd/g-C_3N_4 catalysts was performed with a k-weight of 1. Fitting results are summarized in Table 4.1. An increasing CN for Pd-Pd is observed as the catalyst is further reduced. Notably, the Pd-Pd interaction cannot be quantified for the non-reduced catalyst. A Pd-Pd CN of 1.0 ± 0.2 and 2.2 ± 1.1 is observed for the post H_2(g) and $NaBH_4$-reduced catalysts, respectively. The absence of a Pd-Pd feature for the non-reduced catalyst suggests that Pd(II) is in a single-atom environment on a g-C_3N_4 matrix. The larger CN for the reduced systems suggests slight agglomeration of Pd species to form clusters in the g-C_3N_4 matrix. This suggests that the single-atom Pd/g-C_3N_4 catalyst is not stable under hydrogenation conditions; that is, Pd begins to agglomerate. R-values for Pd-Pd and Pd-N bonds given in Table 4.1 are in good agreement with literature values of 2.75 Å for Pd-Pd and ~ 2.0 Å for Pd-N.[14,58] Note that the 2.0% Pd/g-C_3N_4 reduced sample (reduced with $NaBH_4$) was analyzed on the HXMA beamline, while the other two samples (not reduced and post $H_{2(g)}$ treatment) were analyzed on BioXAS at the CLS. The Pd foil reference data was almost identical, though the flux was much lower on BioXAS than on HXMA at the Pd K-edge, which leads to more noise at higher k values. This means that secondary shells can not be analyzed as well using BioXAS, though the data and fits do not appear to be affected in any way. The appendix of this work contains the phase-corrected EXAFS fits from Artemis for each of the catalysts mentioned in Table 4.1.

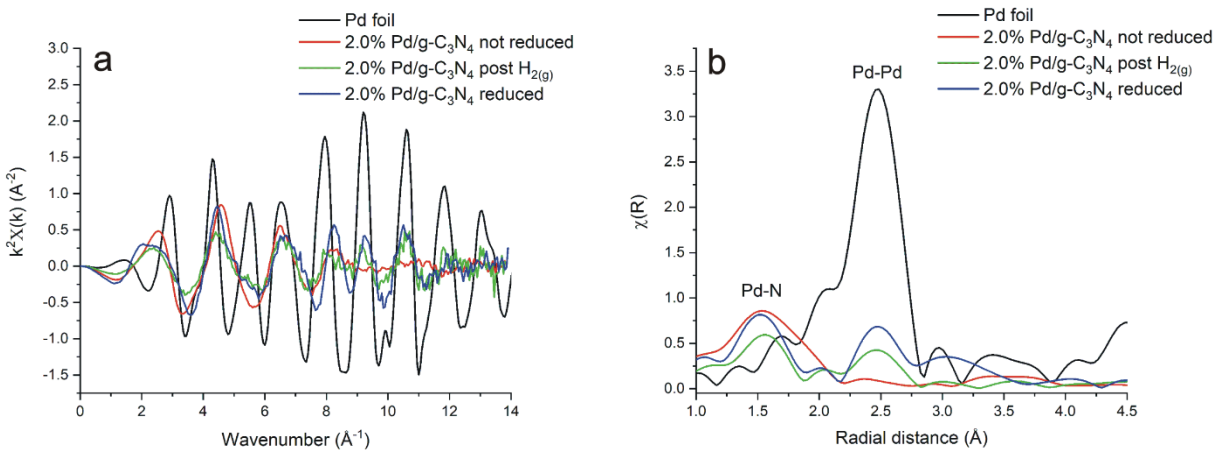

Figure 4.5. a) k-space data from the Pd K-edge on HXMA and BioXAS beamlines, and b) R-space data from HXMA and BioXAS beamlines.

Table 4.1. EXAFS Fitting Parameters for 2.0% Pd/g-C_3N_4 Catalysts.

Catalyst	Bond	CN	R (Å)	σ^2 (Å^2)	E_0 (eV)	R-
2.0% as-synthesized	Pd-Pd Pd-N	ND[1] 3.4 ± 0.2	ND 2.05 ± 0.01	ND 0.001 ± 0.001	ND 7.0 ± 1.3	0.021
2.0% post $H_{2(g)}$	Pd-Pd Pd-N	1.0 ± 0.2 1.8 ± 0.1	2.74 ± 0.01 2.04 ± 0.01	0.003 ± 0.002 0.001 ± 0.001	-1.8 ± 1.6 4.3 ± 0.9	0.013
2.0% Pd/g-C_3N_4	Pd-Pd Pd-N	2.2 ± 1.1 2.5 ± 0.6	2.71 ± 0.03 2.03 ± 0.03	0.006 ± 0.004 0.001 ± 0.004	-3.9 ± 3.2 3.4 ± 3.0	0.056

[1]ND = Not detected. This indicates that the errors in the EXAFS parameter were larger than the value given.

Figure 4.6 contains R-space data from the HXMA beamline at the CLS on the Pd K-edge for 0.1, 0.5, and 2.0% Pd/g-C_3N_4 catalysts reduced with $NaBH_4$. A Pd-Pd interaction around 2.5 Å and Pd-N interaction around 1.5 Å are observed for each catalyst. Qualitatively, changing the weight percentage of Pd from 0.1 to 2.0% does not show an obvious trend in the EXAFS region. Each catalyst shows a reduced intensity peak at 2.5 Å, indicating Pd cluster formation. The EXAFS spectra were fit with IFEFFIT software using Artemis with the same models that were used to

generate the values in Table 4.1. These EXAFS fitting results are listed in Table 4.2. Pd-Pd CNs of 1.5 ± 0.5, 1.4 ± 0.6, and 2.2 ± 1.1 are measured for the 0.1, 0.5, and 2.0% Pd/g-C_3N_4 reduced catalysts, respectively. Again, there is no obvious trend in the data, though it is apparent that some Pd-Pd bonding is present in all these systems. R-values in Table 4.2 for Pd-Pd and Pd-N bonds agree well with literature at 2.75 and ~ 2.0 Å, respectively.[14,58] Through fitting the EXAFS data, it can be concluded that as the Pd/g-C_3N_4 catalyst is reduced by $NaBH_4$, small Pd clusters become apparent on the g-C_3N_4 matrix, as noted by Pd-Pd CNs that are larger than 1.

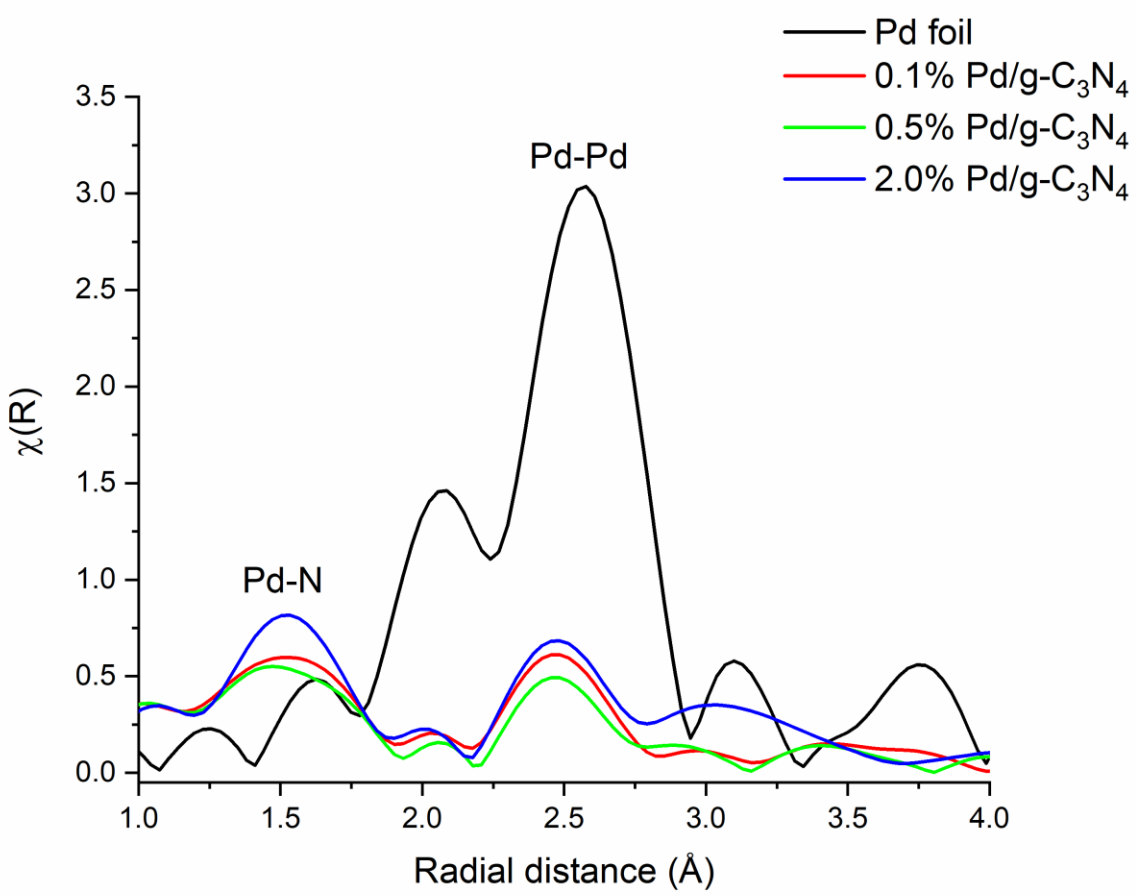

Figure 4.6. R-space data on the Pd K-edge from the HXMA beamline at the CLS for 0.1, 0.5, and 2.0% reduced Pd/g-C_3N_4 Catalysts.

Table 4.2. EXAFS Fitting Parameters for 0.1, 0.5, and 0.2% reduced Pd/g-C_3N_4 Catalysts.

Catalyst	Bond	CN	R (Å)	σ^2 (Å^2)	E_0 (eV)	R-
0.1% Pd/g-C_3N_4	Pd-Pd Pd-N	1.5 ± 0.5 2.9 ± 0.4	2.74 ± 0.02 2.03 ± 0.02	0.004 ± 0.003 0.005 ± 0.003	-0.6 ± 2.3 4.9 ± 1.7	0.025
0.5% Pd/g-C_3N_4	Pd-Pd Pd-N	1.4 ± 0.6 3.0 ± 0.6	2.74 ± 0.03 2.03 ± 0.03	0.006 ± 0.004 0.007 ± 0.004	-2.3 ± 3.1 4.4 ± 2.4	0.025
2.0% Pd/g-C_3N_4	Pd-Pd Pd-N	2.2 ± 1.1 2.5 ± 0.6	2.71 ± 0.03 2.03 ± 0.03	0.006 ± 0.004 0.001 ± 0.004	-3.9 ± 3.2 3.4 ± 3.0	0.056

4.3 Hydrogenation of 2-methyl-3-butyn-2-ol by Pd/g-C_3N_4 and co-Au_4Pd catalysts

Table 4.3 contains the results of MBY hydrogenation studies using the Pd/g-C_3N_4 catalyst with varying weight percentages of Pd on g-C_3N_4. An obvious trend of increased activity at increase Pd weight percentages is seen, with near 100% conversions observed for the catalysts with more than 0.5% Pd present. As more Pd is present, the reaction goes to completion sooner, which is marked by the high selectivity for the alkane (MBA) in the case of the 2.0% Pd catalyst. MBA is considered the fully hydrogenated product, where the alkene (MBE) is first produced and then further hydrogenated to the final alkane product.[29,43,44,155,156] An interesting feature in Table 4.3 is the comparison between the reduced and not reduced 2.0% Pd catalyst. For a 1 hour reaction, both show nearly 100.0% conversions to the fully hydrogenated alkane product, suggesting that Pd is reduced on g-C_3N_4 over the course of the hydrogenation reaction. This conclusion is consistent with the XAS and XPS data previously discussed. The equivalence of MBY used in each case differed as a constant volume of MBY was delivered (0.1 mL) for each reaction.

Table 4.3. MBY Hydrogenation Results for Pd/g-C_3N_4 Catalysts[a]

Wt. % Pd	MBY equiv. to Pd	Conversion (%)	Compound	Selectivity (%)	TON	TOF (h^{-1})
0.1%	10642	44	MBE MBA	90 10	4683	4683
0.5%	2128	99	MBE MBA	67 33	2107	2107
2.0% reduced	532	99	MBE MBA	0 100	528	528
2.0% as-synthesized	532	99	MBE MBA	1 99	527	527

[a]All reactions were run for 1 hour, stirring at 1600 rpm at room temperature (22 ^oC). TON was calculated by multiplying the substrate ratio to Pd by the total conversion percentage. TOF was calculated by dividing the TON by 1 hour.

Table 4.4 shows a time study comparison between a 0.5% Pd/g-C_3N_4 catalyst, and a PVP-stabilized co-Au_4Pd catalyst from Chapter 3 and a PVP-stabilized 3 mM Pd NP solution. This comparison was performed to evaluate the structure-sensitivity of this hydrogenation reaction and to compare the heterogeneous system to our earlier quasi-homogeneous system. Each reaction was run in duplicate. The [Pd] = 3.0 mM for both the quasi-homogeneous system and the Pd NP system. Results from Table 4.3 suggest that the hydrogenation of MBY is not structure-sensitive; that is, MBE can not be selectively produced using either the heterogeneous or quasi-homogeneous SACs. Pd NPs were the most active catalyst, while the quasi-homogeneous co-Au_4Pd is the least active catalysts at a set reaction time, with the heterogeneous system residing in the middle of these two. For the 30 minute reaction, a conversion of 62 ± 3%, 39 ± 5%, and 22 ± 1% to MBE and MBA are seen for the Pd NP, 0.5% Pd/g-C_3N_4, and co-Au_4Pd catalyst, respectively. There is no obvious trend in the selectivity data, meaning this reaction or the catalysts are not selective in forming the MBE product without producing MBA. Increasing the time increases the amount of MBA

produced as the reaction is allowed to react further. These results indicate that less Pd can be used in the synthesis of a supported Pd/g-C_3N_4 catalyst to achieve similar results to a higher concentrated Pd NP catalyst if allowed to react for slightly longer periods of time.

Table 4.4. MBY Hydrogenation Time Study and Catalyst Comparison[a]

Sample (reaction time)	MBY equiv. to Pd	Conversion (%)	Compound	Selectivity (%)	TON	TOF (h^{-1})
0.5% Pd (1.5 hours)	2128	99 ± 1	MBE MBA	0 100	2112 ± 1	1408 ± 1
0.5% Pd (1 hour)	2128	99 ± 1	MBE MBA	43 ± 34 57 ± 34	2106 ± 1	2106 ± 1
0.5% Pd (30 min)	2128	39 ± 5	MBE MBA	89 ± 3 11 ± 3	828 ± 111	1657 ± 223
co-Au_4Pd (1.5 hours)	250	99 ± 1	MBE MBA	12 ± 1 88 ± 1	248 ± 1	166 ± 1
co-Au_4Pd (1 hour)	250	48 ± 4	MBE MBA	81 ± 1 19 ± 1	121 ± 9	121 ± 9
co-Au_4Pd (30 min)	250	22 ± 1	MBE MBA	81 ± 1 19 ± 1	56 ± 1	111 ± 1
Pd NP (1.5 hours)	250	100	MBE MBA	10 ± 10 90 ± 10	249 ± 1	166 ± 1
Pd NP (1 hour)	250	100 ± 1	MBE MBA	50 ± 19 50 ± 19	249 ± 1	249 ± 1
Pd NP (30 min)	250	62 ± 3	MBE MBA	89 ± 10 11 ± 10	155 ± 7	311 ± 14

[a]All reactions were stirred at 1600 rpm at room temperature (22 ^oC). TON and TOF values were calculated as in Table 4.3.

4.4 Conclusion

Revisiting the results of the work of Li *et al.*,[155] the Pd/g-C_3N_4 system was able to show high conversions, though selectivity did not appear to structure-sensitive. Li *et al.* noted reaction conditions between 4 and 12 hours, much longer than our work. The products of the reaction were analyzed using similar GC-FID techniques, though selectivities from our work compared to theirs differ drastically. Our Pd/g-C_3N_4 catalyst was able to convert MBY to MBE or MBA much quicker than the Au@Au_4Pd_1 core-shell nanocube catalyst and our previously mentioned co-reduced Au_4Pd near SAC, though the ability to selectively hydrogenate MBY to MBE was not seen. A more prominent conclusion can be made about the stability of the Pd/g-C_3N_4 system. The as-synthesized catalyst shows single-atom Pd(II) sites on a g-C_3N_4 matrix, though as the catalyst is used in the hydrogenation reaction, Pd begins to reduce to Pd(0) and agglomerate on the g-C_3N_4 matrix, losing the single-atom morphology. Care should be taken when calling these catalysts "single-atom," as it is evident that Pd cluster formation occurs upon introduction to an $H_{2(g)}$ atmosphere, indicating that these systems are not robust.

Chapter 5 Conclusions and Future Work

5.1 Conclusions on the Synthesis, Characterization, and Catalytic Properties of Quasi-Homogeneous and Heterogeneous Pd-Based Catalysts

In Chapter 2, the synthesis of three different Pd-based catalysts was discussed. Quasi-homogeneous bimetallic Au_xPd catalysts (x = 4, 3, 2, and 1) were synthesized via two reduction methods, co-reduction and sequential reduction, to produce single-atom and NP catalysts. A heterogeneous catalyst was also designed to compare and contrast with the quasi-homogeneous Pd catalysts. In this synthesis, a precursor, K_2PdCl_4, was mixed with a g-C_3N_4 support with different weight percentages of Pd at 0.1%, 0.5%, and 2.0%. In the heterogeneous system, the Pd precursor was added to the support, followed by reduction, to produce a Pd/g-C_3N_4 catalyst. These catalysts were then subject to numerous characterization techniques to determine the structural characteristics of each catalyst.

In Chapters 3 and 4, TEM, XPS, and XAS techniques were employed to analyze the surface and composition of each catalyst. In Chapter 3, particle sizes were calculated for co- and seq-Au_xPd catalysts to determine whether particle growth was occurring upon Pd addition. Results suggest that no secondary nucleation of Pd NPs is occurring upon Pd reduction in the Au matrix. This result was the first identification of a bimetallic system, though XPS and XAS techniques were more conclusive. In our XPS analysis, the Pd 3d peak and Au 4f peak showed that both Au(0) and Pd(0) metal were present on the surface of each catalyst. XAS was performed at the Pd K-edge, Pd L_{III}-edge, and Au L_{III}-edge for the co-and seq-Au_xPd catalysts to determine the local environment around Pd and Au metal centers. Shifts in the energy and intensity of the white line in the XANES region on the Pd K-edge and Au L_{III}-edge confirmed that electrons were being

withdrawn from the 4d band of Pd by neighbouring Au atoms. Modelling of the EXAFS region in R-space and k-space gave quantitative evidence that Pd was singly isolated in an Au matrix for co-reduced Au_4Pd, giving a Pd-Pd first shell CN of 1.2 ± 0.3 and a large Pd-Au first shell CN of 8.7 ± 0.8, indicating that a large amount of Pd was on the surface and almost exclusively surrounded by Au atoms (*i.e.* it is nearly a single-atom catalyst (SAC)). The sequentially reduced Au_4Pd showed near single-atom structure with Pd only on the surface, though with a first shell Pd-Pd CN of 1.6 ± 0.3 and a lower Pd-Au first shell CN of 6.1 ± 0.5. For the sequentially reduced Au_xPd catalysts, it was determined through qualitative k-space analysis and EXAFS modelling that a core-shell morphology was present (*i.e.*, an Au core with a Pd shell), as the Au in these Au_xPd catalysts was in a near-bulk environment (*i.e.*, they had a first shell Au-Au CN of 12). Large first shell Au-Au CNs and minute Au-Pd CNs were observed through EXAFS modelling, which further established a core-shell morphology for the sequentially reduced Au_xPd catalysts.

Results from the selective oxidation of crotyl alcohol showed that the bimetallic Au_xPd catalysts were more active and selective in forming crotonaldehyde than typical monometallic Au and Pd NPs. Comparing the co-reduced and sequentially reduced Au_xPd catalysts, it was shown that co-reduced Au_4Pd, the near SAC, was most active with a conversion of 39 ± 9% and selectivity for crotonaldehyde of 77 ± 2%. As the ratio of Au:Pd decreased towards unity, both conversion and selectivity decreased. This trend was also observed for the sequentially reduced Au_xPd catalysts, with seq-Au_4Pd having a conversion of 21 ± 1% and selectivity towards crotonaldehyde of 62 ± 1%. Furthermore, the oxidation reaction was performed in the absence of $O_{2(g)}$ and the addition of vinyl acetate (VA). VA was successfully shown to perform as a sacrificial alkene to aid in removing Pd-H species from the surface of the catalysts, improving conversion and selectivity to crotonaldehyde and reducing side-product formation. Both conversion and selectivity

increased for co-reduced and sequentially reduced Au_xPd catalysts at 4:1 and 1:1 Au:Pd ratios when VA was added to the reaction, with co-Au_4Pd having a conversion of 45 ± 1% while seq-Au_4Pd gave a conversion of 30 ± 1%. Selectivities towards crotonaldehyde of 88 ± 1% and 78 ± 1% were also observed for the co- and sequentially reduced catalysts, respectively. Through the work in Chapter 3, it was shown that a near SAC, co-Au_4Pd, was more active and selective in oxidizing crotyl alcohol to crotonaldehyde compared to monometallic Au and Pd NPs, as well as other co- and seq-Au_xPd catalysts.

In Chapter 4, a heterogeneous Pd/g-C_3N_4 catalyst with 0.1%, 0.5%, and 2.0% weight percentages of Pd was characterized via TEM, XPS, and XAS techniques. This SAC was then subjected to the hydrogenation reaction of 2-methyl-3-butyn-2-ol (MBY) to see if the alkene, 2-methyl-3-buten-2-ol (MBE), could be produced selectively. XPS spectra were collected for the Pd 3d peaks for Pd/g-C_3N_4 catalyst that was not reduced (denoted "as-synthesized") and reduced by $NaBH_4$ to analyze the Pd speciation on g-C_3N_4. From XPS fitting, it was determined that the as-synthesized catalyst was predominantly Pd(II). Upon reduction with $NaBH_4$, a large Pd(II) feature was observed along with a small Pd(0) feature. This result suggests that some Pd is indeed reduced from an oxidation state of 2+ to 0 upon $NaBH_4$ addition. Furthermore, XANES data was collected on SXRMB at the CLS on the Pd L_{III}-edge for the as-synthesized, post $H_{2(g)}$, and reduced catalysts. It was observed that a noticeable decrease in the white line intensity *ca.* 3175 eV occurred after reduction with $NaBH_4$ or with the use of the unreduced catalyst as a hydrogenation catalyst. This further proves that Pd begins to reduce under an $H_{2(g)}$ atmosphere, as well as upon $NaBH_4$ addition. EXAFS analysis was performed on HXMA and BioXAS beamlines at the CLS on the Pd K-edge. From EXAFS data fitting, it was determined that the 0.1, 0.5, and 2.0% Pd/g-C_3N_4 catalysts showed minimal first shell Pd-Pd CNs of 1.5 ± 0.5, 1.4 ± 0.6, and 2.2 ± 1.1, respectively, while

more substantial first shell Pd-N contributions were seen. No obvious trend was apparent in terms of the Pd-Pd CN and weight percentage of Pd used. More conclusively, a series of 2.0% Pd/g-C_3N_4 catalysts as-synthesized, subject to $H_{2(g)}$ treatment, and reduced by $NaBH_4$ were analyzed by EXAFS. From EXAFS fitting data, a conclusion can be made that the as-synthesized catalyst has Pd(II) in a single-atom environment, as no Pd-Pd contributions were apparent. However, upon $H_{2(g)}$ treatment to simulate the hydrogenation environment, it was found that Pd(II) begins to reduce to Pd(0), forming small Pd clusters on the g-C_3N_4 matrix. Furthermore, the reduced Pd/g-C_3N_4 catalyst by $NaBH_4$ showed further Pd agglomeration and cluster formation. Pd-Pd first shell CNs for the treated and reduced catalysts were determined to be 1.0 ± 0.2 and 2.2 ± 1.1, respectively. These EXAFS fitting results agree with previous conclusions made from XPS and XANES analyses.

Pd/g-C_3N_4 catalysts were evaluated for the hydrogenation of MBY. As the weight percentage of Pd was increased, the activity of the catalyst increased, though selectivity towards the alkene (MBE) was not achieved. Conversions of 44, 99, and 99% were observed for a 1 hour hydrogenation reaction for each catalyst, respectively. Selectivities towards MBE of 90, 67, and 0% were achieved, respectively. The decrease in selectivity is simply due to the fully-hydrogenated product, 2-methyl-2-butanol (MBA), being produced more rapidly with increasing Pd weight percentage. The 2.0% Pd/g-C_3N_4 catalyst was then compared to an as-synthesized 2.0% Pd/g-C_3N_4 catalyst in the same 1 hour hydrogenation of MBY. Conversions of 99 and 99% were obtained, with selectivities to MBE of 0 and 1%, respectively. This result further suggests that Pd is reduced during the hydrogenation reaction, as the catalysts behave almost similarly during the 1 hour reaction. Finally, a time study was performed to compare the activity and selectivity of a reduced 0.5% Pd/g-C_3N_4, PVP-stabilized co-Au_4Pd, and PVP-stabilized Pd NP catalyst. This serves as a

comparison between the catalyst from Chapter 3 and Chapter 4, as well as an observation of structure-sensitivity in terms of producing MBE from MBY without any MBA. Each catalyst was able to convert MBY to MBE, though as the time of the reaction was increased from 30 minutes to 1 hour to 1.5 hours, the selectivity of MBE decreased to near 0% for each catalyst. This suggests that the hydrogenation reaction is not structure-sensitive and that either a heterogeneous or quasi-homogeneous catalyst can be used to hydrogenate MBY, though neither catalyst can selectively isolate the semi-hydrogenated MBE product. Through the work in Chapter 4, it was shown that an as-synthesized Pd/g-C_3N_4 catalyst has Pd(II) in a single-atom morphology, though upon reduction by $H_{2(g)}$ or $NaBH_4$, the single-atom Pd morphology is partially lost as Pd clusters begin to form. This result indicates that care should be taken when denoting these catalysts as "single-atom" in the literature, as it is apparent that the reaction environment or addition of a reducing agent can produce Pd clusters on a g-C_3N_4 matrix. Another conclusion can be made about the structure-sensitivity for the hydrogenation of MBY to MBE. Through our work in Chapter 4, it was shown that both SAC and non-SAC Pd catalysts could convert MBY to MBE and further to MBA without any indication that MBE can be selectively produced. This would indicate that no structure-sensitive relationship for hydrogenation reactions exist in this system.

In this work, a series of near SACs were synthesized, characterized, and evaluated in the oxidation of crotyl alcohol and hydrogenation of 2-methyl-3-butyn-2-ol. Both quasi-homogeneous and heterogeneous Pd-based catalysts were synthesized in this work. Through the characterization of these catalysts with TEM, XPS, and XAS, it was shown that we were able to make a single-atom bimetallic and monometallic catalysts supported on an Au NP and graphitic carbon nitride, respectively. In the oxidation of crotyl alcohol, it was shown that a near SAC (co-Au_4Pd) is not only more active but also more selective in producing crotonaldehyde, the desired product from

crotyl alcohol, relative to larger bimetallic and monometallic NP catalysts. It was also discovered that the heterogeneous Pd catalyst (Pd/g-C_3N_4) was not active for the oxidation reaction. For the hydrogenation of 2-methyl-3-butyn-2-ol, it was shown that the Pd/g-C_3N_4 heterogeneous catalyst was more active than the quasi-homogeneous near SAC, but selectivity towards the alkene could not be controlled using either catalyst. This reaction was also performed with a larger Pd NP catalyst, again showing no obvious selectivity. This lack of selectivity in either a near SAC or larger NP catalyst indicates that the hydrogenation reaction is not structure-sensitive. Through EXAFS fitting, it was shown that over the course of the hydrogenation reaction, Pd begins to agglomerate on the surface of graphitic carbon nitride, losing its single-atom structure. The final state of the catalyst after catalysis is rarely reported for SACs in the literature, and this works shows that it cannot be assumed that SACs retain their structures during catalytic events.

5.2 Future Work

5.2.1 Methane Oxidation

Recently, Pd- and Pt-based SACs and NPs have been studied in the selective oxidation of methane (CH_4) to methanol (CH_3OH).[39–41,116,157] For example, Agarwal *et al.* synthesized a bimetallic AuPd colloid catalyst for the selective oxidation of methane to methanol under high pressure and moderate temperature conditions (30 bar of CH_4 at 50 ^oC). The issue with most methane oxidation reactions is the need for high temperature and pressure systems to oxidize methane, creating either a dangerous work environment or expensive cost for producing methanol. Current approaches towards methanol formation involve the use of syngas, a mixture of CO and H_2. This process is not economically favourable, has a low carbon efficiency, and is a multistage process.[157] DFT studies are becoming prominent[40,158,159] for the use of SACs in the direct

conversion of methane to methanol, though few laboratory-scale experiments have been performed. The use of metal-based SACs under ambient conditions to oxidize methane into methanol could massively improve the economic and environmental aspects of this industrially relevant catalytic cycle.

5.2.2 Using Operando Synchrotron Techniques for *In Situ* Catalysis

Within our group and others,[21,26,136,160,161] *in situ* catalysis at synchrotron facilities has been used to evaluate numerous characteristics of catalysts during catalytic reactions. "On the line" catalysis is a term used for running catalytic experiments while collecting XAS data at the same time, providing information on how a catalyst behaves under the reaction conditions. This information can be used to either improve the catalyst or the catalytic conditions to create a more efficient cycle. For example, an *in situ* oxidation of crotyl alcohol, "on the line," could be performed at the CLS to evaluate when the catalytic reaction begins or ends and how the catalyst behaves under certain conditions (i.e., does it oxidize or degrade). A reaction cell would have to be designed to deliver a set amount of substrate (crotyl alcohol) over a designated period, while also incorporating either $O_{2(g)}$ or vinyl acetate under high-stirring conditions. XAS scans would have numerous times over a specified time interval. We could also employ operando techniques[162–165] to quantify the products of the reaction during analysis on the beamline. For example, gas chromatography could be attached to the system, and the products of a crotyl alcohol oxidation could be quantified almost instantaneously.

5.2.3 Designing a Pd/g-C_3N_4 Single-Atom Catalyst for Structure-Sensitive Hydrogenation Reactions

From our work in Chapter 4, it was shown that the Pd/g-C_3N_4 catalyst was not truly a SAC; that is, the Pd-Pd first shell CNs were slightly above 1 at each weight percentage of Pd. Future work with this catalyst would include optimizing the synthesis to reduce Pd agglomeration in the g-C_3N_4 matrix to design a single-atom heterogeneous catalyst for use in structure-sensitive hydrogenation reactions. The hydrogenation of MBY was shown to occur using both quasi-homogeneous and heterogeneous catalysts in Chapter 4, with no selectivity towards the alkene product. We were not able to control the production of the alkene, with time being the only factor in the reaction. It would be beneficial to show that the structure of the catalyst can dictate which products are formed for other possible reactions (i.e. a structure-sensitive reaction). In the literature, the dependence on the catalyst structure is shown to drive reactions to produce the desired product without the formation of side-products.[166–169] It would be useful to show that our g-C_3N_4 catalyst is capable of selectively producing some desired product and compare that to the quasi-homogeneous catalysts that have different structures. A model reaction that could be followed is the hydrogenation of phenol, as shown by Guan *et al.*[169] and Zhang *et al.*[168] The hydrogenation of phenol is particularly important to produce biodiesel and other bio-oils. Oxygenated aromatic compounds, such as phenol, are detrimental to the efficiency of bio-oils and need to be removed.[168,169] If we were able to convert these phenolic compounds to useful compounds such as ketones, alcohols, and hydrocarbons, selectively, it would prove to be environmentally and economically beneficial.

References

(1) Roduner, E. Understanding Catalysis. *Chem. Soc. Rev.* **2014**, *43* (24), 8226–8239.

(2) Sheldon, R. A.; Pereira, P. C. Biocatalysis Engineering: The Big Picture. *Chem. Soc. Rev.* **2017**, *46* (10), 2678–2691.

(3) Zhang, P.; Sadler, P. J. Advances in the Design of Organometallic Anticancer Complexes. *J. Organomet. Chem.* **2017**, *839*, 5–14.

(4) Stamenkovic, V. R.; Strmcnik, D.; Lopes, P. P.; Markovic, N. M. Energy and Fuels from Electrochemical Interfaces. *Nat. Mater.* **2017**, *16* (1), 57–69.

(5) Link, S.; El-Sayed, M. A. Optical Properties and Ultrafast Dynamics of Metallic Nanocrystals. *Annu. Rev. Phys. Chem* **2003**, *54* (1), 331–366.

(6) Astruc, D.; Lu, F.; Aranzaes, J. R. Nanoparticles as Recyclable Catalysts: The Frontier between Homogeneous and Heterogeneous Catalysis. *Angew. Chem. Int. Ed.* **2005**, *44* (48), 7852–7872.

(7) Michalet, X. Quantum Dots for Live Cells, in Vivo Imaging, and Diagnostics. *Science* **2005**, *307* (5709), 538–544.

(8) Dabbousi, B. O.; Rodriguez-Viejo, J.; Mikulec, F. V.; Heine, J. R.; Mattoussi, H.; Ober, R.; Jensen, K. F.; Bawendi, M. G. (CdSe)ZnS Core−Shell Quantum Dots: Synthesis and Characterization of a Size Series of Highly Luminescent Nanocrystallites. *J. Phys. Chem. B* **1997**, *101* (46), 9463–9475.

(9) Baughman, R. H.; Zakhidov, A. A.; Heer, W. A. de. Carbon Nanotubes--the Route Toward Applications. *Science* **2002**, *297* (5582), 787–792.

(10) Pan, Y.; Sun, K.; Liu, S.; Cao, X.; Wu, K.; Cheong, W.-C.; Chen, Z.; Wang, Y.; Li, Y.; Liu, Y.; et al. Core–Shell ZIF-8@ZIF-67-Derived CoP Nanoparticle-Embedded N-Doped Carbon

Nanotube Hollow Polyhedron for Efficient Overall Water Splitting. *J. Am. Chem. Soc.* **2018**, *140* (7), 2610–2618.

(11) Daniel, M.-C.; Astruc, D. Gold Nanoparticles: Assembly, Supramolecular Chemistry, Quantum-Size-Related Properties, and Applications toward Biology, Catalysis, and Nanotechnology. *Chem. Rev.* **2004**, *104* (1), 293–346.

(12) Narayanan, R.; El-Sayed, M. A. Catalysis with Transition Metal Nanoparticles in Colloidal Solution: Nanoparticle Shape Dependence and Stability. *J. Phys. Chem. B* **2005**, *109* (26), 12663–12676.

(13) Thomas, J. M.; Johnson, B. F. G.; Raja, R.; Sankar, G.; Midgley, P. A. High-Performance Nanocatalysts for Single-Step Hydrogenations. *Acc. Chem. Res.* **2003**, *36* (1), 20–30.

(14) Wrasman, C. J.; Boubnov, A.; Riscoe, A. R.; Hoffman, A. S.; Bare, S. R.; Cargnello, M. Synthesis of Colloidal Pd/Au Dilute Alloy Nanocrystals and Their Potential for Selective Catalytic Oxidations. *J. Am. Chem. Soc.* **2018**, *140* (40), 12930–12939.

(15) Shivhare, A.; Ambrose, S. J.; Zhang, H.; Purves, R. W.; Scott, R. W. J. Stable and Recyclable Au25 Clusters for the Reduction of 4-Nitrophenol. *Chem. Commun.* **2012**, *49* (3), 276–278.

(16) Chen, H.; Liu, C.; Wang, M.; Zhang, C.; Luo, N.; Wang, Y.; Abroshan, H.; Li, G.; Wang, F. Visible Light Gold Nanocluster Photocatalyst: Selective Aerobic Oxidation of Amines to Imines. *ACS Catal.* **2017**, *7* (5), 3632–3638.

(17) Lu, P.; Teranishi, T.; Asakura, K.; Miyake, M.; Toshima, N. Polymer-Protected Ni/Pd Bimetallic Nano-Clusters: Preparation, Characterization and Catalysis for Hydrogenation of Nitrobenzene. *J. Phys. Chem. B* **1999**, *103* (44), 9673–9682.

(18) Camacho-Bunquin, J.; Ferrandon, M. S.; Sohn, H.; Kropf, A. J.; Yang, C.; Wen, J.; Hackler, R. A.; Liu, C.; Celik, G.; Marshall, C. L.; et al. Atomically Precise Strategy to a PtZn Alloy

Nanocluster Catalyst for the Deep Dehydrogenation of *n* -Butane to 1,3-Butadiene. *ACS Catal.* **2018**, *8* (11), 10058–10063.

(19) Sun, S.; Murray, C. B.; Weller, D.; Folks, L.; Moser, A. Monodisperse FePt Nanoparticles and Ferromagnetic FePt Nanocrystal Superlattices. *Science* **2000**, *287* (5460), 1989–1992.

(20) Chertok, B.; Moffat, B. A.; David, A. E.; Yu, F.; Bergemann, C.; Ross, B. D.; Yang, V. C. Iron Oxide Nanoparticles as a Drug Delivery Vehicle for MRI Monitored Magnetic Targeting of Brain Tumors. *Biomaterials* **2008**, *29* (4), 487–496.

(21) Yao, Y.; Rubino, S.; Gates, B. D.; Scott, R. W. J.; Hu, Y. In Situ X-Ray Absorption Spectroscopic Studies of Magnetic Fe@Fe_xO_y/Pd Nanoparticle Catalysts for Hydrogenation Reactions. *Catal. Today* **2017**, *291*, 180–186.

(22) Alberti, S.; Caratto, V.; Peddis, D.; Belviso, C.; Ferretti, M. Synthesis and Characterization of a New Photocatalyst Based on TiO_2 Nanoparticles Supported on a Magnetic Zeolite Obtained from Iron and Steel Industrial Waste. *J. Alloys Compd.* **2019**, *797*, 820–825.

(23) Zhang, F.; Zhao, J.; Shen, T.; Hidaka, H.; Pelizzetti, E.; Serpone, N. TiO_2-Assisted Photodegradation of Dye Pollutants II. Adsorption and Degradation Kinetics of Eosin in TiO_2 Dispersions under Visible Light Irradiation. *Appl. Catal., B* **1998**, *15* (1), 147–156.

(24) Liu, Y.; Guo, W.; Guo, H.; Ren, X.; Xu, Q. Cu (II)-Doped V2O5 Mediated Persulfate Activation for Heterogeneous Catalytic Degradation of Benzotriazole in Aqueous Solution. *Sep. Purif. Technol.* **2020**, *230*, 115848.

(25) Rodriguez, J. A.; Ma, S.; Liu, P.; Hrbek, J.; Evans, J.; Pérez, M. Activity of CeOx and TiOx Nanoparticles Grown on Au(111) in the Water-Gas Shift Reaction. *Science* **2007**, *318* (5857), 1757–1760.

(26) Maclennan, A.; Banerjee, A.; Hu, Y.; Miller, J. T.; Scott, R. W. J. In Situ X-Ray Absorption Spectroscopic Analysis of Gold–Palladium Bimetallic Nanoparticle Catalysts. *ACS Catal.* **2013**, *3* (6), 1411–1419.

(27) Maclennan, A.; Banerjee, A.; Scott, R. W. J. Aerobic Oxidation of α,β-Unsaturated Alcohols Using Sequentially-Grown AuPd Nanoparticles in Water and Tetraalkylphosphonium Ionic Liquids. *Catal. Today* **2013**, *207*, 170–179.

(28) da Silva, F. P.; Fiorio, J. L.; Gonçalves, R. V.; Teixeira-Neto, E.; Rossi, L. M. Synergic Effect of Copper and Palladium for Selective Hydrogenation of Alkynes. *Ind. Eng. Chem. Res.* **2018**, *57* (48), 16209–16216.

(29) Crespo-Quesada, M.; Grasemann, M.; Semagina, N.; Renken, A.; Kiwi-Minsker, L. Kinetics of the Solvent-Free Hydrogenation of 2-Methyl-3-Butyn-2-ol over a Structured Pd-Based Catalyst. *Catal. Today* **2009**, *147* (3), 247–254.

(30) Li, A.; Tang, Y.; Dong, C.; Wang, G. Facile Synthesis of Ag-CuO/SBA-15 for Aerobic Epoxidation of Olefins with High Activity. *Nanotechnology* **2019**.

(31) Zhao, G.; Gao, Z.; Li, H.; Liu, S.; Chen, L.; Zhang, R.; Guo, H. Controlled Assembly of Ag Nanoparticles on the Surface of Phosphate Pillar [6]Arene Functionalized Single-Walled Carbon Nanotube for Enhanced Catalysis and Sensing Performance. *Electrochim. Acta* **2019**, *318*, 711–719.

(32) Liu, S.; Tian, J.; Wang, L.; Sun, X. A Method for the Production of Reduced Graphene Oxide Using Benzylamine as a Reducing and Stabilizing Agent and Its Subsequent Decoration with Ag Nanoparticles for Enzymeless Hydrogen Peroxide Detection. *Carbon* **2011**, *49* (10), 3158–3164.

(33) Li, G.; Jin, R. Gold Nanocluster-Catalyzed Semihydrogenation: A Unique Activation Pathway for Terminal Alkynes. *J. Am. Chem. Soc.* **2014**, *136* (32), 11347–11354.

(34) Dong, Y.; Jiang, P.; Xie, W. Harvesting Hot Electrons on Au Nanoparticle Monolayer by Efficient Compensation of Holes. *Appl. Mater. Today* **2019**, *14*, 201–206.

(35) Zhu, W.; Michalsky, R.; Metin, Ö.; Lv, H.; Guo, S.; Wright, C. J.; Sun, X.; Peterson, A. A.; Sun, S. Monodisperse Au Nanoparticles for Selective Electrocatalytic Reduction of CO_2 to CO. *J. Am. Chem. Soc.* **2013**, *135* (45), 16833–16836.

(36) Alayoglu, S.; Nilekar, A. U.; Mavrikakis, M.; Eichhorn, B. Ru–Pt Core–Shell Nanoparticles for Preferential Oxidation of Carbon Monoxide in Hydrogen. *Nat. Mater.* **2008**, *7* (4), 333–338.

(37) Turner, M.; Golovko, V. B.; Vaughan, O. P. H.; Abdulkin, P.; Berenguer-Murcia, A.; Tikhov, M. S.; Johnson, B. F. G.; Lambert, R. M. Selective Oxidation with Dioxygen by Gold Nanoparticle Catalysts Derived from 55-Atom Clusters. *Nature* **2008**, *454* (7207), 981–983.

(38) Wang, D.; Villa, A.; Spontoni, P.; Su, D. S.; Prati, L. In Situ Formation of Au–Pd Bimetallic Active Sites Promoting the Physically Mixed Monometallic Catalysts in the Liquid-Phase Oxidation of Alcohols. *Chem. Eur. J.* **2010**, *16* (33), 10007–10013.

(39) Agarwal, N.; Freakley, S. J.; McVicker, R. U.; Althahban, S. M.; Dimitratos, N.; He, Q.; Morgan, D. J.; Jenkins, R. L.; Willock, D. J.; Taylor, S. H.; et al. Aqueous Au-Pd Colloids Catalyze Selective CH_4 Oxidation to CH_3OH with O_2 under Mild Conditions. *Science* **2017**, *358* (6360), 223–227.

(40) Yuan, J.; Zhang, W.; Li, X.; Yang, J. A High Performance Catalyst for Methane Conversion to Methanol: Graphene Supported Single Atom Co. *Chem. Commun.* **2018**, *54* (18), 2284–2287.

(41) Petrov, A. W.; Ferri, D.; Krumeich, F.; Nachtegaal, M.; Bokhoven, J. A. van; Kröcher, O. Stable Complete Methane Oxidation over Palladium Based Zeolite Catalysts. *Nat. Commun.* **2018**, *9* (1), 2545.

(42) Liu, J.; Shan, J.; Lucci, F. R.; Cao, S.; Sykes, E. C. H.; Flytzani-Stephanopoulos, M. Palladium–Gold Single Atom Alloy Catalysts for Liquid Phase Selective Hydrogenation of 1-Hexyne. *Catal. Sci. Technol.* **2017**, *7* (19), 4276–4284.

(43) Okhlopkova, L. B.; Cherepanova, S. V.; Prosvirin, I. P.; Kerzhentsev, M. A.; Ismagilov, Z. R. Semihydrogenation of 2-Methyl-3-Butyn-2-ol on Pd-Zn Nanoalloys: Effect of Composition and Heterogenization. *Appl. Catal., A* **2018**, *549*, 245–253.

(44) Okhlopkova, L. B.; Kerzhentsev, M. A.; Ismagilov, Z. R. Coating the Internal Surface of a Capillary Microreactor for the Selective Hydrogenation of 2-Methyl-3-Butyn-2-ol by $Pd_xZn_{1}–x/TiO_2$ Catalysts: A Kinetic Study. *Kinet. Catal.* **2018**, *59* (4), 450–458.

(45) Kattel, S.; Ramírez, P. J.; Chen, J. G.; Rodriguez, J. A.; Liu, P. Active Sites for CO_2 Hydrogenation to Methanol on Cu/ZnO Catalysts. *Science* **2017**, *355* (6331), 1296–1299.

(46) Huang, F.; Deng, Y.; Chen, Y.; Cai, X.; Peng, M.; Jia, Z.; Ren, P.; Xiao, D.; Wen, X.; Wang, N.; et al. Atomically Dispersed Pd on Nanodiamond/Graphene Hybrid for Selective Hydrogenation of Acetylene. *J. Am. Chem. Soc.* **2018**, *140* (41), 13142–13146.

(47) Beaumont, S. K. Heterogeneously Catalyzing C–C Coupling Reactions with Precious Metal Nanoparticles. *J. Chem. Technol. Biotechnol.* **2012**, *87* (5), 595–600.

(48) Sawoo, S.; Srimani, D.; Dutta, P.; Lahiri, R.; Sarkar, A. Size Controlled Synthesis of Pd Nanoparticles in Water and Their Catalytic Application in C–C Coupling Reactions. *Tetrahedron* **2009**, *65* (22), 4367–4374.

(49) Qu, F.; Li, N. B.; Luo, H. Q. Transition from Nanoparticles to Nanoclusters: Microscopic and Spectroscopic Investigation of Size-Dependent Physicochemical Properties of Polyamine-Functionalized Silver Nanoclusters. *J. Phys. Chem. C* **2013**, *117* (7), 3548–3555.

(50) Chakraborty, I.; Pradeep, T. Atomically Precise Clusters of Noble Metals: Emerging Link between Atoms and Nanoparticles. *Chem. Rev.* **2017**, *117* (12), 8208–8271.

(51) Jin, R.; Zeng, C.; Zhou, M.; Chen, Y. Atomically Precise Colloidal Metal Nanoclusters and Nanoparticles: Fundamentals and Opportunities. *Chem. Rev.* **2016**, *116* (18), 10346–10413.

(52) Parkinson, G. S. Single-Atom Catalysis: How Structure Influences Catalytic Performance. *Catal. Lett.* **2019**.

(53) Zhang, H.; Liu, G.; Shi, L.; Ye, J. Single-Atom Catalysts: Emerging Multifunctional Materials in Heterogeneous Catalysis. *Adv. Energy. Mater.* **2018**, *8* (1), 1701343.

(54) Thirumalai, H.; Kitchin, J. R. Investigating the Reactivity of Single Atom Alloys Using Density Functional Theory. *Top. Catal.* **2018**, *61* (5–6), 462–474.

(55) Yang, X.-F.; Wang, A.; Qiao, B.; Li, J.; Liu, J.; Zhang, T. Single-Atom Catalysts: A New Frontier in Heterogeneous Catalysis. *Acc. Chem. Res.* **2013**, *46* (8), 1740–1748.

(56) Liang, S.; Hao, C.; Shi, Y. The Power of Single-Atom Catalysis. *ChemCatChem* **2015**, *7* (17), 2559–2567.

(57) Liu, L.; Wu, X.; Wang, L.; Xu, X.; Gan, L.; Si, Z.; Li, J.; Zhang, Q.; Liu, Y.; Zhao, Y.; et al. Atomic Palladium on Graphitic Carbon Nitride as a Hydrogen Evolution Catalyst under Visible Light Irradiation. *Commun. Chem.* **2019**, *2* (1), 18.

(58) Kim, H.-E.; Lee, I. H.; Cho, J.; Shin, S.; Ham, H. C.; Kim, J. Y.; Lee, H. Palladium Single-Atom Catalysts Supported on $C@C_3N_4$ for Electrochemical Reactions. *Chem. Electro. Chem.* **2019**, *6* (18), 4757–4764.

(59) Muzart, J. Palladium-Catalysed Oxidation of Primary and Secondary Alcohols. *Tetrahedron* **2003**, *59* (31), 5789–5816.

(60) Toshima, N.; Yonezawa, T. Bimetallic Nanoparticles—Novel Materials for Chemical and Physical Applications. *New J. Chem.* **1998**, *22* (11), 1179–1201.

(61) Harada, M.; Asakura, K.; Toshima, N. Catalytic Activity and Structural Analysis of Polymer-Protected Gold/Palladium Bimetallic Clusters Prepared by the Successive Reduction of Hydrogen Tetrachloroaurate(III) and Palladium Dichloride. *J. Phys. Chem.* **1993**, *97* (19), 5103–5114.

(62) Sinfelt, J. H. Catalysis by Alloys and Bimetallic Clusters. *Acc. Chem. Res.* **1977**, *10* (1), 15–20.

(63) Scott, R. W. J.; Wilson, O. M.; Oh, S.-K.; Kenik, E. A.; Crooks, R. M. Bimetallic Palladium−Gold Dendrimer-Encapsulated Catalysts. *J. Am. Chem. Soc.* **2004**, *126* (47), 15583–15591.

(64) Jover, J.; García-Ratés, M.; López, N. The Interplay between Homogeneous and Heterogeneous Phases of PdAu Catalysts for the Oxidation of Alcohols. *ACS Catal.* **2016**, *6* (7), 4135–4143.

(65) Lee, A. F.; Ellis, C. V.; Wilson, K.; Hondow, N. S. In Situ Studies of Titania-Supported Au Shell–Pd Core Nanoparticles for the Selective Aerobic Oxidation of Crotyl Alcohol. *Catal. Today* **2010**, *157* (1), 243–249.

(66) Mori, K.; Hara, T.; Mizugaki, T.; Ebitani, K.; Kaneda, K. Hydroxyapatite-Supported Palladium Nanoclusters: A Highly Active Heterogeneous Catalyst for Selective Oxidation of Alcohols by Use of Molecular Oxygen. *J. Am. Chem. Soc.* **2004**, *126* (34), 10657–10666.

(67) Liu, J.; Uhlman, M. B.; Montemore, M. M.; Trimpalis, A.; Giannakakis, G.; Shan, J.; Cao, S.; Hannagan, R. T.; Sykes, E. C. H.; Flytzani-Stephanopoulos, M. Integrated Catalysis-Surface Science-Theory Approach to Understand Selectivity in the Hydrogenation of 1-Hexyne to 1-Hexene on PdAu Single-Atom Alloy Catalysts. *ACS Catal.* **2019**, *9* (9), 8757–8765.

(68) Feng, Y.; Zhou, L.; Wan, Q.; Lin, S.; Guo, H. Selective Hydrogenation of 1,3-Butadiene Catalyzed by a Single Pd Atom Anchored on Graphene: The Importance of Dynamics. *Chem. Sci.* **2018**, *9* (27), 5890–5896.

(69) Ueno, T.; Suzuki, M.; Goto, T.; Matsumoto, T.; Nagayama, K.; Watanabe, Y. Size-Selective Olefin Hydrogenation by a Pd Nanocluster Provided in an Apo-Ferritin Cage. *Angew. Chem. Int. Ed.* **2004**, *43* (19), 2527–2530.

(70) Liu, J. Catalysis by Supported Single Metal Atoms. *ACS Catal.* **2017**, *7* (1), 34–59.

(71) Dhiman, M.; Polshettiwar, V. Supported Single Atom and Pseudo-Single Atom of Metals as Sustainable Heterogeneous Nanocatalysts. *ChemCatChem* **2018**, *10* (5), 881–906.

(72) Chen, Z.; Vorobyeva, E.; Mitchell, S.; Fako, E.; López, N.; Collins, S. M.; Leary, R. K.; Midgley, P. A.; Hauert, R.; Pérez-Ramírez, J. Single-Atom Heterogeneous Catalysts Based on Distinct Carbon Nitride Scaffolds. *Natl. Sci. Rev.* **2018**, *5* (5), 642–652.

(73) Mitchell, S.; Vorobyeva, E.; Pérez-Ramírez, J. The Multifaceted Reactivity of Single-Atom Heterogeneous Catalysts. *Angew. Chem. Int. Ed.* **2018**, *57* (47), 15316–15329.

(74) Hou, W.; Dehm, N. A.; Scott, R. W. J. Alcohol Oxidations in Aqueous Solutions Using Au, Pd, and Bimetallic AuPd Nanoparticle Catalysts. *J. Catal.* **2008**, *253* (1), 22–27.

(75) Balcha, T.; Strobl, J. R.; Fowler, C.; Dash, P.; Scott, R. W. J. Selective Aerobic Oxidation of Crotyl Alcohol Using AuPd Core-Shell Nanoparticles. *ACS Catal.* **2011**, *1* (5), 425–436.

(76) Hayashi, S.; Ishida, R.; Hasegawa, S.; Yamazoe, S.; Tsukuda, T. Doping a Single Palladium Atom into Gold Superatoms Stabilized by PVP: Emergence of Hydrogenation Catalysis. *Top. Catal.* **2018**, *61* (1–2), 136–141.

(77) Chen, Y.; Yang, F.; Dai, Y.; Wang, W.; Chen, S. Ni@Pt Core−Shell Nanoparticles: Synthesis, Structural and Electrochemical Properties. *J. Phys. Chem. C* **2008**, *112* (5), 1645–1649.

(78) Chen, Z.; Mitchell, S.; Vorobyeva, E.; Leary, R. K.; Hauert, R.; Furnival, T.; Ramasse, Q. M.; Thomas, J. M.; Midgley, P. A.; Dontsova, D.; et al. Stabilization of Single Metal Atoms on Graphitic Carbon Nitride. *Adv. Funct. Mater.* **2017**, *27* (8), 1605785.

(79) Xin, P.; Li, J.; Xiong, Y.; Wu, X.; Dong, J.; Chen, W.; Wang, Y.; Gu, L.; Luo, J.; Rong, H.; et al. Revealing the Active Species for Aerobic Alcohol Oxidation by Using Uniform Supported Palladium Catalysts. *Angew. Chem. Int. Ed.* **2018**, *57* (17), 4642–4646.

(80) Huang, X.; Yan, H.; Huang, L.; Zhang, X.; Lin, Y.; Li, J.; Xia, Y.; Ma, Y.; Sun, Z.; Wei, S.; et al. Toward Understanding of the Support Effect on Pd_1 Single-Atom-Catalyzed Hydrogenation Reactions. *J. Phys. Chem. C* **2019**, *123* (13), 7922–7930.

(81) Marx, S.; Baiker, A. Beneficial Interaction of Gold and Palladium in Bimetallic Catalysts for the Selective Oxidation of Benzyl Alcohol. *J. Phys. Chem. C* **2009**, *113* (15), 6191–6201.

(82) Miura, H.; Endo, K.; Ogawa, R.; Shishido, T. Supported Palladium–Gold Alloy Catalysts for Efficient and Selective Hydrosilylation under Mild Conditions with Isolated Single Palladium Atoms in Alloy Nanoparticles as the Main Active Site. *ACS Catal.* **2017**, *7* (3), 1543–1553.

(83) Pei, G. X.; Liu, X. Y.; Wang, A.; Lee, A. F.; Isaacs, M. A.; Li, L.; Pan, X.; Yang, X.; Wang, X.; Tai, Z.; et al. Ag Alloyed Pd Single-Atom Catalysts for Efficient Selective Hydrogenation of Acetylene to Ethylene in Excess Ethylene. *ACS Catal.* **2015**, *5* (6), 3717–3725.

(84) Marcinkowski, M. D.; Darby, M. T.; Liu, J.; Wimble, J. M.; Lucci, F. R.; Lee, S.; Michaelides, A.; Flytzani-Stephanopoulos, M.; Stamatakis, M.; Sykes, E. C. H. Pt/Cu Single-Atom Alloys as Coke-Resistant Catalysts for Efficient C–H Activation. *Nat. Chem.* **2018**, *10* (3), 325–332.

(85) Vorobyeva, E.; Chen, Z.; Mitchell, S.; Leary, R. K.; Midgley, P.; Thomas, J. M.; Hauert, R.; Fako, E.; López, N.; Pérez-Ramírez, J. Tailoring the Framework Composition of Carbon Nitride to Improve the Catalytic Efficiency of the Stabilised Palladium Atoms. *J. Mater. Chem. A* **2017**, *5* (31), 16393–16403.

(86) Wang, A.; Li, J.; Zhang, T. Heterogeneous Single-Atom Catalysis. *Nat. Rev. Chem* **2018**, *2* (6), 65–81.

(87) He, F.; Li, K.; Yin, C.; Wang, Y.; Tang, H.; Wu, Z. Single Pd Atoms Supported by Graphitic Carbon Nitride, a Potential Oxygen Reduction Reaction Catalyst from Theoretical Perspective. *Carbon* **2017**, *114*, 619–627.

(88) Vilé, G.; Albani, D.; Nachtegaal, M.; Chen, Z.; Dontsova, D.; Antonietti, M.; López, N.; Pérez-Ramírez, J. A Stable Single-Site Palladium Catalyst for Hydrogenations. *Angew. Chem. Int. Ed.* **2015**, *54* (38), 11265–11269.

(89) Gao, G.; Jiao, Y.; Waclawik, E. R.; Du, A. Single Atom (Pd/Pt) Supported on Graphitic Carbon Nitride as an Efficient Photocatalyst for Visible-Light Reduction of Carbon Dioxide. *J. Am. Chem. Soc.* **2016**, *138* (19), 6292–6297.

(90) Li, Z.; Wang, D.; Wu, Y.; Li, Y. Recent Advances in the Precise Control of Isolated Single Site Catalysts by Chemical Methods. *Natl. Sci. Rev.* **2018**.

(91) Kim, J.; Kim, H.-E.; Lee, H. Single-Atom Catalysts of Precious Metals for Electrochemical Reactions. *ChemSusChem* **2018**, *11* (1), 104–113.

(92) Zhou, H.; Hong, S.; Zhang, H.; Chen, Y.; Xu, H.; Wang, X.; Jiang, Z.; Chen, S.; Liu, Y. Toward Biomass-Based Single-Atom Catalysts and Plastics: Highly Active Single-Atom Co on N-Doped Carbon for Oxidative Esterification of Primary Alcohols. *Appl. Catal., B* **2019**, *256*, 117767.

(93) Zhao, J.; Qin, R.; Liu, R. Urea-Bridging Synthesis of Nitrogen-Doped Carbon Tube Supported Single Metallic Atoms as Bifunctional Oxygen Electrocatalyst for Zinc-Air Battery. *Appl. Catal., B* **2019**, *256*, 117778.

(94) Xu, B.; Wang, H.; Wang, W.; Gao, L.; Li, S.; Pan, X.; Wang, H.; Yang, H.; Meng, X.; Wu, Q.; et al. A Single-Atom Nanozyme for Wound Disinfection Applications. *Angew. Chem. Int. Ed.* **2019**, *58* (15), 4911–4916.

(95) Sun, Y.; Zhou, J.; Ji, H.; Liu, J.; Qian, T.; Yan, C. Single-Atom Iron as Lithiophilic Site To Minimize Lithium Nucleation Overpotential for Stable Lithium Metal Full Battery. *ACS Appl. Mater. Interfaces* **2019**, *11* (35), 32008–32014.

(96) Hunter, M. A.; Fischer, J. M. T. A.; Yuan, Q.; Hankel, M.; Searles, D. J. Evaluating the Catalytic Efficiency of Paired, Single-Atom Catalysts for the Oxygen Reduction Reaction. *ACS Catal.* **2019**, *9* (9), 7660–7667.

(97) Zhang, B.; Sun, G.; Ding, S.; Asakura, H.; Zhang, J.; Sautet, P.; Yan, N. Atomically Dispersed Pt1–Polyoxometalate Catalysts: How Does Metal–Support Interaction Affect Stability and Hydrogenation Activity? *J. Am. Chem. Soc.* **2019**, *141* (20), 8185–8197.

(98) Yang, M.; Allard, L. F.; Flytzani-Stephanopoulos, M. Atomically Dispersed Au–$(OH)_x$ Species Bound on Titania Catalyze the Low-Temperature Water-Gas Shift Reaction. *J. Am. Chem. Soc.* **2013**, *135* (10), 3768–3771.

(99) Lin, J.; Wang, A.; Qiao, B.; Liu, X.; Yang, X.; Wang, X.; Liang, J.; Li, J.; Liu, J.; Zhang, T. Remarkable Performance of Ir_1/FeO_x Single-Atom Catalyst in Water Gas Shift Reaction. *J. Am. Chem. Soc.* **2013**, *135* (41), 15314–15317.

(100) Lang, R.; Li, T.; Matsumura, D.; Miao, S.; Ren, Y.; Cui, Y.-T.; Tan, Y.; Qiao, B.; Li, L.; Wang, A.; et al. Hydroformylation of Olefins by a Rhodium Single-Atom Catalyst with Activity Comparable to $RhCl(PPh_3)_3$. *Angew. Chem. Int. Ed.* **2016**, *55* (52), 16054–16058.

(101) Deng, D.; Chen, X.; Yu, L.; Wu, X.; Liu, Q.; Liu, Y.; Yang, H.; Tian, H.; Hu, Y.; Du, P.; et al. A Single Iron Site Confined in a Graphene Matrix for the Catalytic Oxidation of Benzene at Room Temperature. *Sci. Adv.* **2015**, *1* (11), e1500462.

(102) Zhang, H.; Wei, J.; Dong, J.; Liu, G.; Shi, L.; An, P.; Zhao, G.; Kong, J.; Wang, X.; Meng, X.; et al. Efficient Visible-Light-Driven Carbon Dioxide Reduction by a Single-Atom Implanted Metal–Organic Framework. *Angew. Chem. Int. Ed.* **2016**, *55* (46), 14310–14314.

(103) Shivhare, A.; Scott, R. W. J. Au25 Clusters as Precursors for the Synthesis of AuPd Bimetallic Nanoparticles with Isolated Atomic Pd-Surface Sites. *J. Mol. Catal.* **2018**, *457*, 33–40.

(104) Zhao, J.; Jin, R. Heterogeneous Catalysis by Gold and Gold-Based Bimetal Nanoclusters. *Nano Today* **2018**, *18*, 86–102.

(105) Negishi, Y.; Kurashige, W.; Kobayashi, Y.; Yamazoe, S.; Kojima, N.; Seto, M.; Tsukuda, T. Formation of a $Pd@Au_{12}$ Superatomic Core in $Au_{24}Pd_1(SC_{12}H_{25})_{18}$ Probed by ^{197}Au

Mössbauer and Pd K-Edge EXAFS Spectroscopy. *J. Phys. Chem. Lett.* **2013**, *4* (21), 3579–3583.

(106) Tofanelli, M. A.; Ni, T. W.; Phillips, B. D.; Ackerson, C. J. Crystal Structure of the $PdAu_{24}(SR)_{18}^{0}$ Superatom. *Inorg. Chem.* **2016**, *55* (3), 999–1001.

(107) Hülsey, M. J.; Zhang, J.; Yan, N. Harnessing the Wisdom in Colloidal Chemistry to Make Stable Single-Atom Catalysts. *Adv. Mater.* **2018**, *30* (47), 1802304.

(108) Shan, J.; Liu, J.; Li, M.; Lustig, S.; Lee, S.; Flytzani-Stephanopoulos, M. NiCu Single Atom Alloys Catalyze the C H Bond Activation in the Selective Non- Oxidative Ethanol Dehydrogenation Reaction. *Appl. Catal., B* **2018**, *226*, 534–543.

(109) Boucher, M. B.; Marcinkowski, M. D.; Liriano, M. L.; Murphy, C. J.; Lewis, E. A.; Jewell, A. D.; Mattera, M. F. G.; Kyriakou, G.; Flytzani-Stephanopoulos, M.; Sykes, E. C. H. Molecular-Scale Perspective of Water-Catalyzed Methanol Dehydrogenation to Formaldehyde. *ACS Nano* **2013**, *7* (7), 6181–6187.

(110) Dimitratos, N.; Villa, A.; Wang, D.; Porta, F.; Su, D.; Prati, L. Pd and Pt Catalysts Modified by Alloying with Au in the Selective Oxidation of Alcohols. *J. Catal.* **2006**, *244* (1), 113–121.

(111) Enache, D. I.; Barker, D.; Edwards, J. K.; Taylor, S. H.; Knight, D. W.; Carley, A. F.; Hutchings, G. J. Solvent-Free Oxidation of Benzyl Alcohol Using Titania-Supported Gold–Palladium Catalysts: Effect of Au–Pd Ratio on Catalytic Performance. *Catal. Today* **2007**, *122* (3–4), 407–411.

(112) Mertens, P. G. N.; Corthals, S. L. F.; Ye, X.; Poelman, H.; Jacobs, P. A.; Sels, B. F.; Vankelecom, I. F. J.; De Vos, D. E. Selective Alcohol Oxidation to Aldehydes and Ketones

over Base-Promoted Gold–Palladium Clusters as Recyclable Quasihomogeneous and Heterogeneous Metal Catalysts. *J. Mol. Catal. A: Chem.* **2009**, *313* (1), 14–21.

(113) Zhao, K.; Zhu, Y.; Shi, J.; Zhao, X.; Pang, R.; Xue, X.; Ren, X.; Duan, X.; Guo, Z. X.; Li, S. Synergetic Effects of Strain Engineering and Substrate Defects on Generating Highly Efficient Single-Atom Catalysts for CO Oxidation. *J. Mater. Chem. A* **2019**, *7* (15), 9297–9304.

(114) Darby, M. T.; Stamatakis, M.; Michaelides, A.; Sykes, E. Charles. H. Lonely Atoms with Special Gifts: Breaking Linear Scaling Relationships in Heterogeneous Catalysis with Single-Atom Alloys. *J. Phys. Chem. Lett.* **2018**, *9* (18), 5636–5646.

(115) Sahoo, S.; Suib, S. L.; Alpay, S. P. Graphene Supported Single Atom Transition Metal Catalysts for Methane Activation. *ChemCatChem* **2018**, *10* (15), 3229–3235.

(116) Williams, C.; Carter, J. H.; Dummer, N. F.; Chow, Y. K.; Morgan, D. J.; Yacob, S.; Serna, P.; Willock, D. J.; Meyer, R. J.; Taylor, S. H.; et al. Selective Oxidation of Methane to Methanol Using Supported AuPd Catalysts Prepared by Stabilizer-Free Sol-Immobilization. *ACS Catal.* **2018**, *8* (3), 2567–2576.

(117) Li, M.; Wu, S.; Yang, X.; Hu, J.; Peng, L.; Bai, L.; Huo, Q.; Guan, J. Highly Efficient Single Atom Cobalt Catalyst for Selective Oxidation of Alcohols. *Appl. Catal., A* **2017**, *543*, 61–66.

(118) Han, B.; Lang, R.; Qiao, B.; Wang, A.; Zhang, T. Highlights of the Major Progress in Single-Atom Catalysis in 2015 and 2016. *Chin. J. Catal.* **2017**, *38* (9), 1498–1507.

(119) Sharifi, T.; Gracia-Espino, E.; Chen, A.; Hu, G.; Wågberg, T. Oxygen Reduction Reactions on Single- or Few-Atom Discrete Active Sites for Heterogeneous Catalysis. *Adv. Energy. Mater.* **2019**.

(120) Lucci, F. R.; Liu, J.; Marcinkowski, M. D.; Yang, M.; Allard, L. F.; Flytzani-Stephanopoulos, M.; Sykes, E. C. H. Selective Hydrogenation of 1,3-Butadiene on Platinum–Copper Alloys at the Single-Atom Limit. *Nat. Commun.* **2015**, *6*, 8550.

(121) Liu, J.; Lucci, F. R.; Yang, M.; Lee, S.; Marcinkowski, M. D.; Therrien, A. J.; Williams, C. T.; Sykes, E. C. H.; Flytzani-Stephanopoulos, M. Tackling CO Poisoning with Single-Atom Alloy Catalysts. *J. Am. Chem. Soc.* **2016**, *138* (20), 6396–6399.

(122) Giannakakis, G.; Flytzani-Stephanopoulos, M.; Sykes, E. C. H. Single-Atom Alloys as a Reductionist Approach to the Rational Design of Heterogeneous Catalysts. *Acc. Chem. Res.* **2019**, *52* (1), 237–247.

(123) Gates, B. C.; Flytzani-Stephanopoulos, M.; Dixon, D. A.; Katz, A. Atomically Dispersed Supported Metal Catalysts: Perspectives and Suggestions for Future Research. *Catal. Sci. Technol.* **2017**, *7* (19), 4259–4275.

(124) Biffis, A.; Centomo, P.; Del Zotto, A.; Zecca, M. Pd Metal Catalysts for Cross-Couplings and Related Reactions in the 21st Century: A Critical Review. *Chem. Rev.* **2018**, *118* (4), 2249–2295.

(125) Suzuki, A. Cross-Coupling Reactions Of Organoboranes: An Easy Way To Construct C□C Bonds (Nobel Lecture). *Angew. Chem. Int. Ed.* **2011**, *50* (30), 6722–6737.

(126) Heck, R. F.; Nolley, J. P. Palladium-Catalyzed Vinylic Hydrogen Substitution Reactions with Aryl, Benzyl, and Styryl Halides. *J. Org. Chem.* **1972**, *37* (14), 2320–2322.

(127) Eremin, D. B.; Ananikov, V. P. Understanding Active Species in Catalytic Transformations: From Molecular Catalysis to Nanoparticles, Leaching, “Cocktails” of Catalysts and Dynamic Systems. *Coord. Chem. Rev.* **2017**, *346*, 2–19.

(128) Vimont, A.; Thibault-Starzyk, F.; Daturi, M. Analysing and Understanding the Active Site by IR Spectroscopy. *Chem. Soc. Rev.* **2010**, *39* (12), 4928–4950.

(129) Elder, F. R.; Gurewitsch, A. M.; Langmuir, R. V.; Pollock, H. C. Radiation from Electrons in a Synchrotron. *Phys. Rev.* **1947**, *71* (11), 829–830.

(130) Sham, T. K.; Rivers, M. L. A Brief Overview of Synchrotron Radiation. *Rev. Mineral Geochem.* **2002**, *49* (1), 117–147.

(131) Newville, M. Fundamentals of XAFS, 2004.

(132) Yano, J.; Yachandra, V. K. X-Ray Absorption Spectroscopy. *Photosynth. Res.* **2009**, *102* (2–3), 241–254.

(133) Bunker, G. X-Ray Absorption Spectroscopy, 2007.

(134) Shivhare, A.; Chevrier, D. M.; Purves, R. W.; Scott, R. W. J. Following the Thermal Activation of $Au_{25}(SR)_{18}$ Clusters for Catalysis by X-Ray Absorption Spectroscopy. *J. Phys. Chem. C* **2013**, *117* (39), 20007–20016.

(135) Lee, E.-K.; Park, S.-A.; Woo, H.; Hyun Park, K.; Kang, D. W.; Lim, H.; Kim, Y.-T. Platinum Single Atoms Dispersed on Carbon Nanotubes as Reusable Catalyst for Suzuki Coupling Reaction. *J. Catal.* **2017**, *352*, 388–393.

(136) Wang, M.; Árnadóttir, L.; Xu, Z. J.; Feng, Z. In Situ X-Ray Absorption Spectroscopy Studies of Nanoscale Electrocatalysts. *Nano-Micro Lett.* **2019**, *11* (1), 47.

(137) Tsunoyama, H.; Ichikuni, N.; Tsukuda, T. Microfluidic Synthesis and Catalytic Application of PVP-Stabilized, ∼1 Nm Gold Clusters. *Langmuir* **2008**, *24* (20), 11327–11330.

(138) Rasband, W.S. ImageJ https://imagej.nih.gov/ij/.

(139) Fairley, Neal. Copyright © 2005 Casa Software Ltd. http://www.casaxps.com/.

(140) Shen, J.; Scott, R. W. J.; Hayes, R. E.; Semagina, N. Structural Evolution of Bimetallic Pd-Ru Catalysts in Oxidative and Reductive Applications. *Appl. Catal., A* **2015**, *502*, 350–360.

(141) Ravel, Bruce. Demeter: XAS Data Processing and Analysis https://bruceravel.github.io/demeter/.

(142) Villa, A.; Janjic, N.; Spontoni, P.; Wang, D.; Su, D. S.; Prati, L. Au–Pd/AC as Catalysts for Alcohol Oxidation: Effect of Reaction Parameters on Catalytic Activity and Selectivity. *Appl. Catal., A* **2009**, *364* (1), 221–228.

(143) J.F. Moulder, W.F. Stickle, P.E. Sobol, K.D. Bomben. *Handbook of X-Ray Photoelectron Spectroscopy*; Perkin-Elmer Corp: Eden Prairie, MN, 1992.

(144) Triest, A. van; Folkerts, W.; Haas, C. Electronic Structure and Photoelectron Spectra of Calaverite, AuTe2. *J. Phys.: Condens. Matter* **1990**, *2* (44), 8733–8740.

(145) Lee, K. E.; Shivhare, A.; Hu, Y.; Scott, R. W. J. Supported Bimetallic AuPd Clusters Using Activated Au_{25} Clusters. *Catal. Today* **2017**, *280*, 259–265.

(146) Witjens, L. C.; Bitter, J. H.; Dillen, A. J. van; Jong, K. P. de; Groot, F. M. F. de. Pd L_3 Edge XANES Investigation of the Electronic and Geometric Structure of Pd/Ag–H Membranes. *Phys. Chem. Chem. Phys.* **2004**, *6* (14), 3903–3906.

(147) Meitzner, G.; Sinfelt, J. H. X-Ray Absorption Studies of the Electronic Structures of Pd-Ag and Pd-Au Alloys. *Catal. Lett.* **1994**, *30* (1), 1–10.

(148) Huang, D. C.; Chang, K. H.; Pong, W. F.; Tseng, P. K.; Hung, K. J.; Huang, W. F. Effect of Ag-promotion on Pd Catalysts by XANES. *Catal. lett.* **1998**, *53* (3), 155–159.

(149) Liu, C.; Chen, N.; Li, J.; Gao, X.; Sham, T.-K.; Wang, S.-D. Fingerprint Feature of Atomic Intermixing in Supported AuPd Nanocatalysts Probed by X-Ray Absorption Fine Structure. *J. Phys. Chem. C* **2017**, *121* (51), 28385–28394.

(150) Newville, M. IFEFFIT : Interactive XAFS Analysis and FEFF Fitting. *J. Synchrotron Rad.* **2001**, *8* (2), 322–324.

(151) Zhang, L.; Wang, A.; Miller, J. T.; Liu, X.; Yang, X.; Wang, W.; Li, L.; Huang, Y.; Mou, C.-Y.; Zhang, T. Efficient and Durable Au Alloyed Pd Single-Atom Catalyst for the Ullmann Reaction of Aryl Chlorides in Water. *ACS Catal.* **2014**, *4* (5), 1546–1553.

(152) Liu, F.; Wechsler, D.; Zhang, P. Alloy-Structure-Dependent Electronic Behavior and Surface Properties of Au–Pd Nanoparticles. *Chem. Phys. Lett.* **2008**, *461* (4), 254–259.

(153) Christensen, S. L.; Chatt, A.; Zhang, P. Biomolecule-Coated Metal Nanoparticles on Titanium. *Langmuir* **2012**, *28* (5), 2979–2985.

(154) Chen, Z.; Mitchell, S.; Krumeich, F.; Hauert, R.; Yakunin, S.; Kovalenko, M. V.; Pérez-Ramírez, J. Tunability and Scalability of Single-Atom Catalysts Based on Carbon Nitride. *ACS Sustain. Chem. Eng.* **2019**, *7* (5), 5223–5230.

(155) Li, Y.; Liu, Q.; Jin, J.; Ye, W.; Hu, C.; Hu, S.; Qi, Z.; Long, R.; Song, L.; Zhu, J.; et al. Controlling Au–Pd Surface on Au Nanocubes for Selective Catalytic Alkyne Semihydrogenation. *Part. Part. Syst. Charact.* **2017**, *35* (5), 1700377.

(156) Vernuccio, S.; Goy, R.; Rohr, P. R. von; Medlock, J.; Bonrath, W. Hydrogenation of 2-Methyl-3-Butyn-2-ol over a Pd/ZnO Catalyst: Kinetic Model and Selectivity Study. *React. Chem. Eng.* **2016**, *1* (4), 445–453.

(157) Xie, P.; Pu, T.; Nie, A.; Hwang, S.; Purdy, S. C.; Yu, W.; Su, D.; Miller, J. T.; Wang, C. Nanoceria-Supported Single-Atom Platinum Catalysts for Direct Methane Conversion. *ACS Catal.* **2018**, *8* (5), 4044–4048.

(158) Nematollahi, P.; Neyts, E. C. Direct Methane Conversion to Methanol on M and MN4 Embedded Graphene (M = Ni and Si): A Comparative DFT Study. *Appl. Surf. Sci.* **2019**, *496*, 143618.

(159) Harrath, K.; Yu, X.; Xiao, H.; Li, J. The Key Role of Support Surface Hydrogenation in the CH_4 to CH_3OH Selective Oxidation by a ZrO_2-Supported Single-Atom Catalyst. *ACS Catal.* **2019**, *9* (10), 8903–8909.

(160) Keresszegi, C.; Grunwaldt, J.-D.; Mallat, T.; Baiker, A. In Situ EXAFS Study on the Oxidation State of Pd/Al_2O_3 and $Bi–Pd/Al_2O_3$ during the Liquid-Phase Oxidation of 1-Phenylethanol. *J. Catal.* **2004**, *222* (1), 268–280.

(161) Nassiri, H.; Lee, K.-E.; Hu, Y.; Hayes, R. E.; Scott, R. W. J.; Semagina, N. Water Shifts PdO-Catalyzed Lean Methane Combustion to Pt-Catalyzed Rich Combustion in Pd–Pt Catalysts: In Situ X-Ray Absorption Spectroscopy. *J. Catal.* **2017**, *352*, 649–656.

(162) Dessal, C.; Len, T.; Morfin, F.; Rousset, J.-L.; Aouine, M.; Afanasiev, P.; Piccolo, L. Dynamics of Single Pt Atoms on Alumina during CO Oxidation Monitored by Operando X-Ray and Infrared Spectroscopies. *ACS Catal.* **2019**, *9* (6), 5752–5759.

(163) Li, X.; Yang, X.; Zhang, J.; Huang, Y.; Liu, B. In Situ/Operando Techniques for Characterization of Single-Atom Catalysts. *ACS Catal.* **2019**, *9* (3), 2521–2531.

(164) Zlotea, C.; Oumellal, Y.; Provost, K.; Morfin, F.; Piccolo, L. Role of Hydrogen Absorption in Supported Pd Nanocatalysts during CO-PROX: Insights from Operando X-Ray Absorption Spectroscopy. *Appl. Catal., B* **2018**, *237*, 1059–1065.

(165) Tinnemans, S. J.; Mesu, J. G.; Kervinen, K.; Visser, T.; Nijhuis, T. A.; Beale, A. M.; Keller, D. E.; van der Eerden, A. M. J.; Weckhuysen, B. M. Combining Operando Techniques in

One Spectroscopic-Reaction Cell: New Opportunities for Elucidating the Active Site and Related Reaction Mechanism in Catalysis. *Catal. Today* **2006**, *113* (1), 3–15.

(166) Granger, P.; Troncéa, S.; Dacquin, J. P.; Trentesaux, M.; Gardoll, O.; Nuns, N.; Parvulescu, V. I. Peculiar Kinetic Properties of Cu-Doped Pd/Ce_xZr_1-xO_2 in Water Denitrification: Impact of Pd-Cu Interaction vs Structural Properties of Ce_xZr_1-xO_2. *Appl. Catal., B* **2019**, *253*, 391–400.

(167) Panic, S.; Srdić, V.; Varga, T.; Kónya, Z.; Kukovecz, Á.; Boskovic, G. Diversity of Pd-Cu Active Sites Supported on Pristine Carbon Nanotubes in Terms of Water Denitration Structure Sensitivity. *Appl. Catal., A* **2018**, *559*, 187–194.

(168) Zhang, Y.; Zhou, J.; Li, K.; Lv, M. Synergistic Catalytic Hydrogenation of Phenol over Hybrid Nano-Structure Pd Catalyst. *Mol. Catal.* **2019**, *478*, 110567.

(169) Guan, Q.; Wang, B.; Chai, X.; Liu, J.; Gu, J.; Ning, P. Comparison of Pd-UiO-66 and Pd-UiO-66-NH_2 Catalysts Performance for Phenol Hydrogenation in Aqueous Medium. *Fuel* **2017**, *205*, 130–141.

Appendix

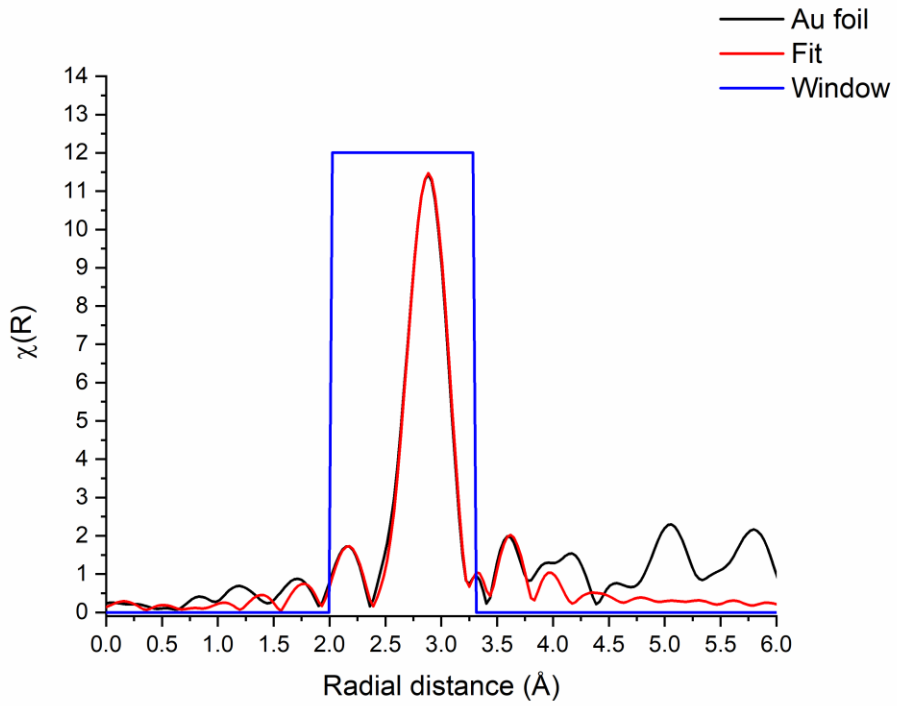

Figure A1. Au L_{III}-edge EXAFS fit for Au foil.

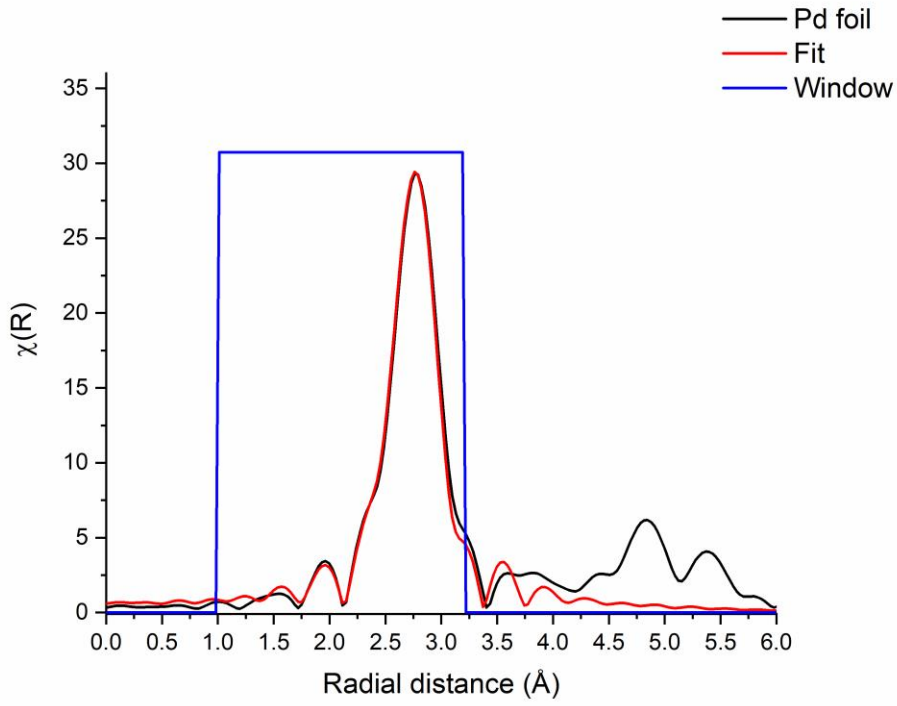

Figure A2. Pd K-edge EXAFS fit for Pd foil.

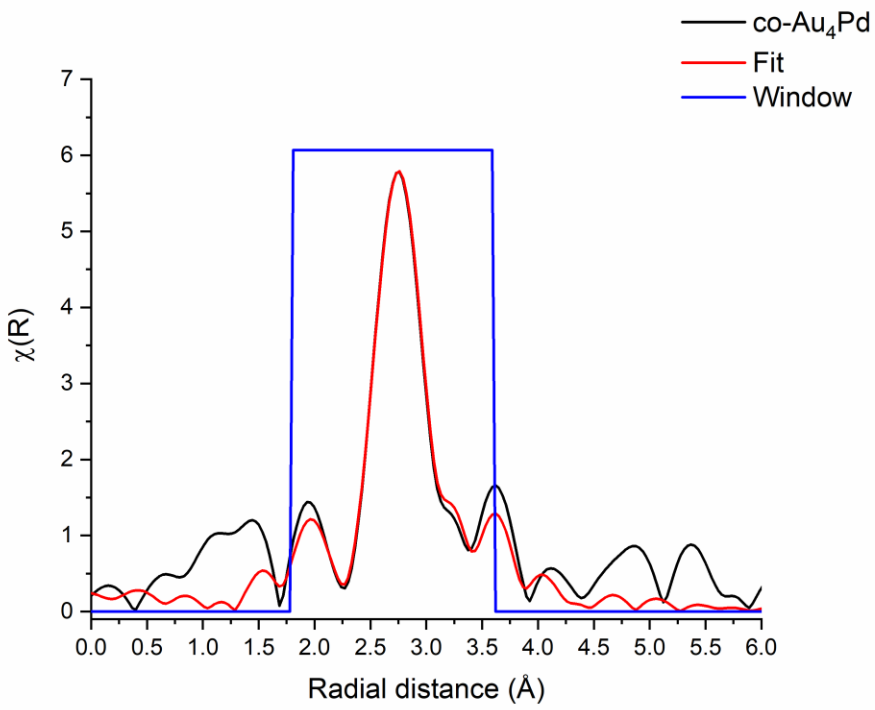

Figure A3. Pd K-edge EXAFS fit for co-Au_4Pd.

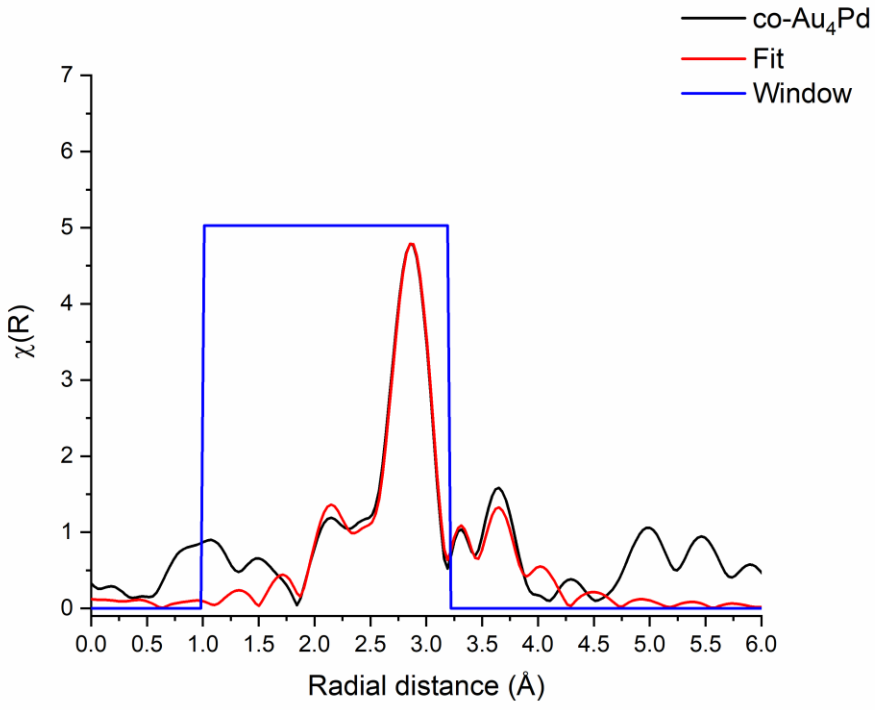

Figure A4. Au L_{III}-edge EXAFS fit for co-Au_4Pd.

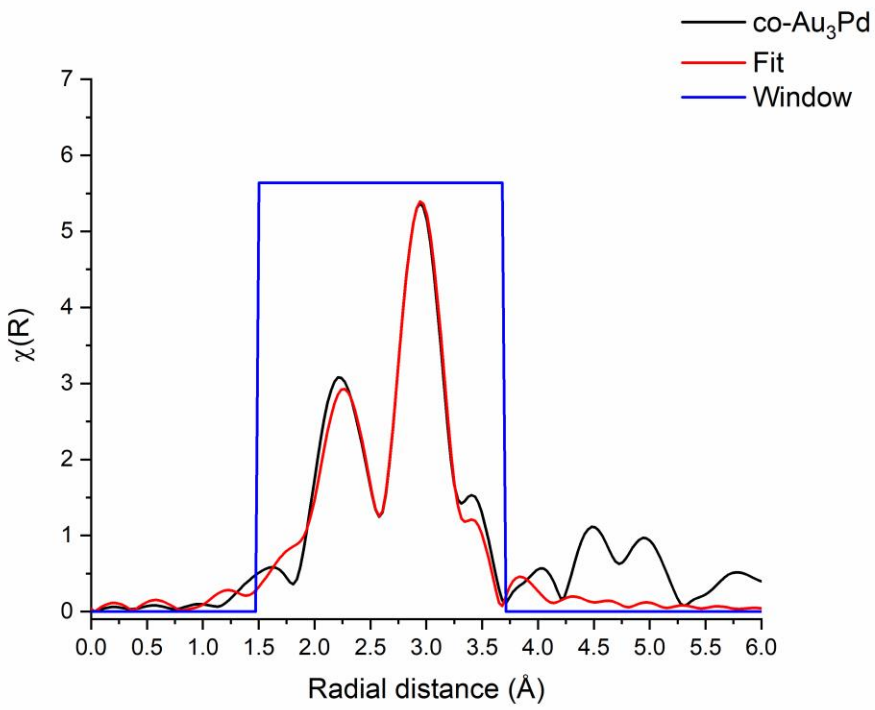

Figure A5. Pd K-edge EXAFS fit for co-Au_3Pd.

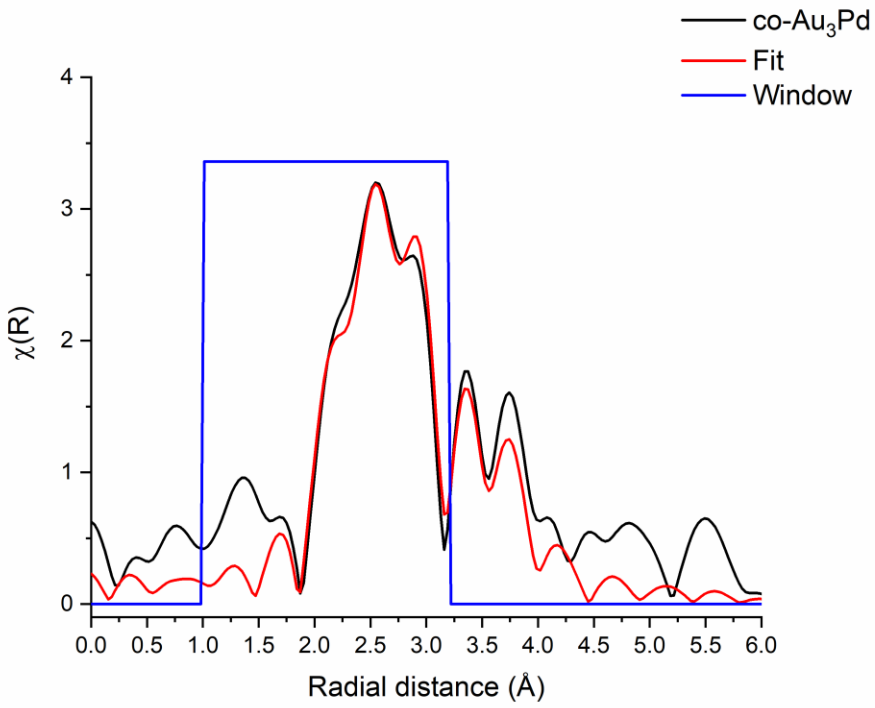

Figure A6. Au L_{III}-edge EXAFS fit for co-Au_3Pd.

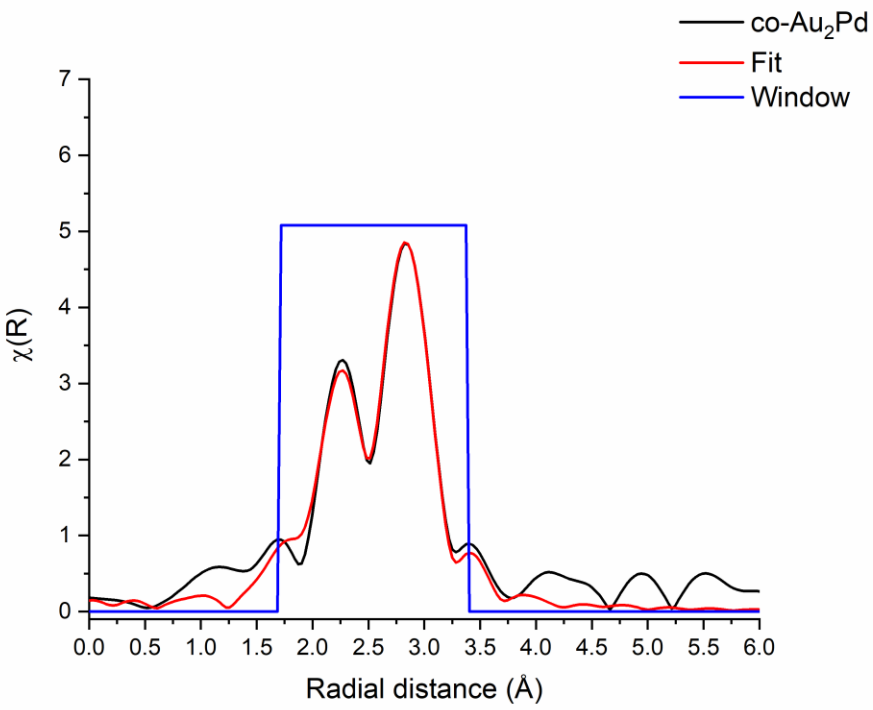

Figure A7. Pd K-edge EXAFS fit for co-Au_2Pd.

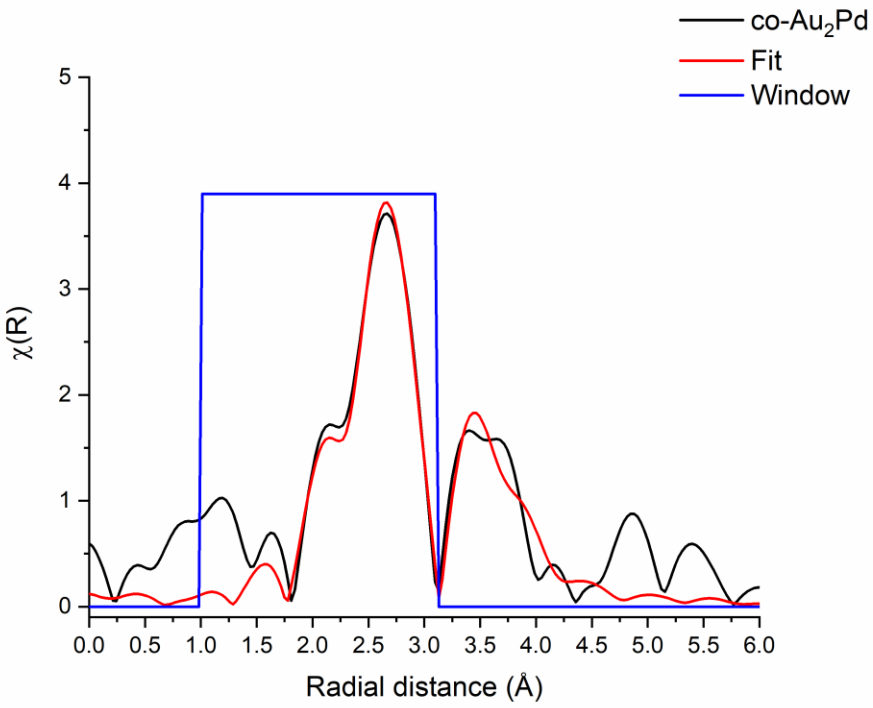

Figure A8. Au L_{III}-edge EXAFS fit for co-Au_2Pd.

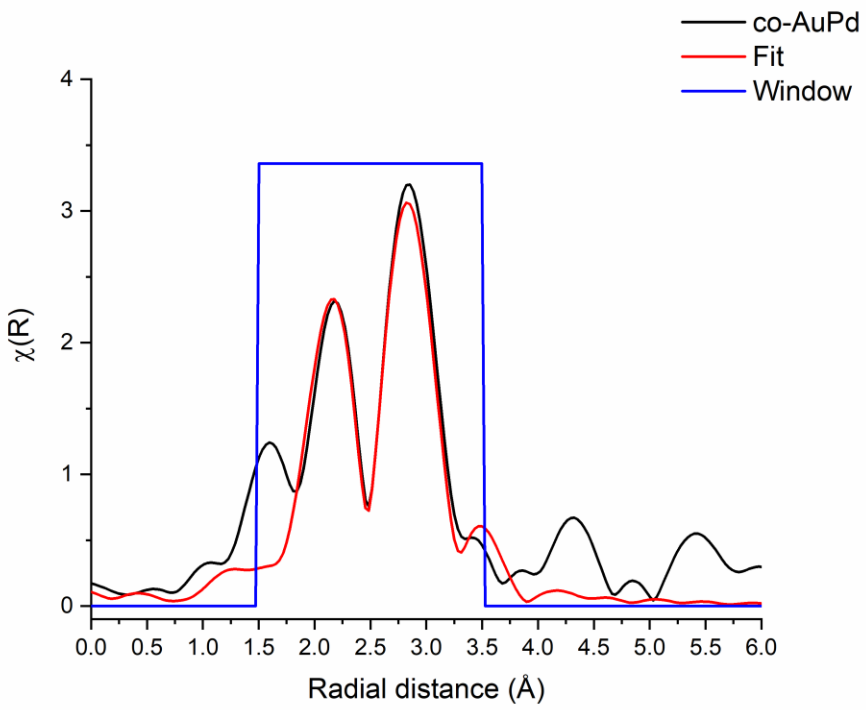

Figure A9. Pd K-edge EXAFS fit for co-AuPd.

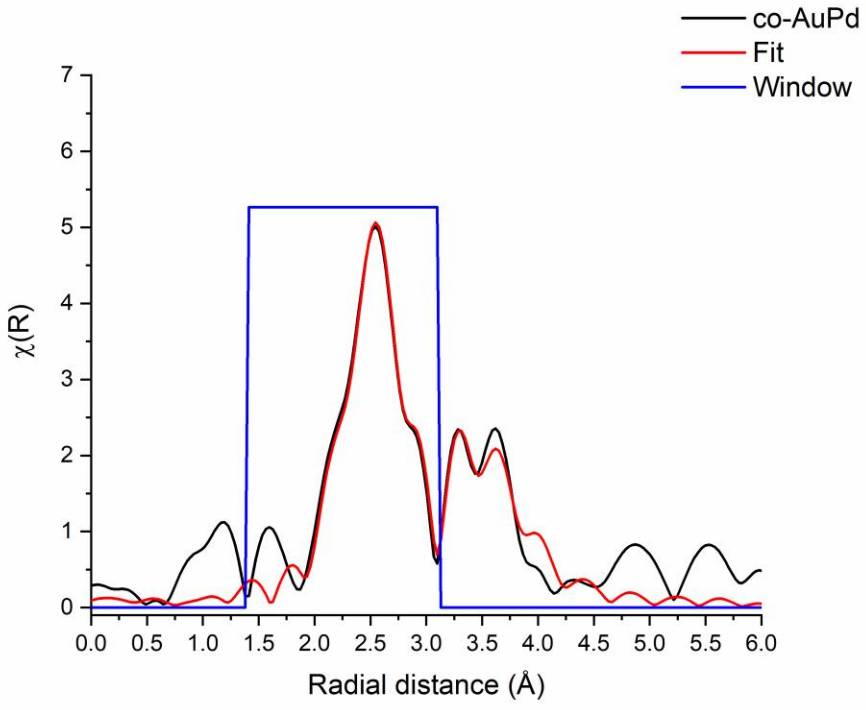

Figure A10. Au L_{III}-edge EXAFS fit for co-AuPd.

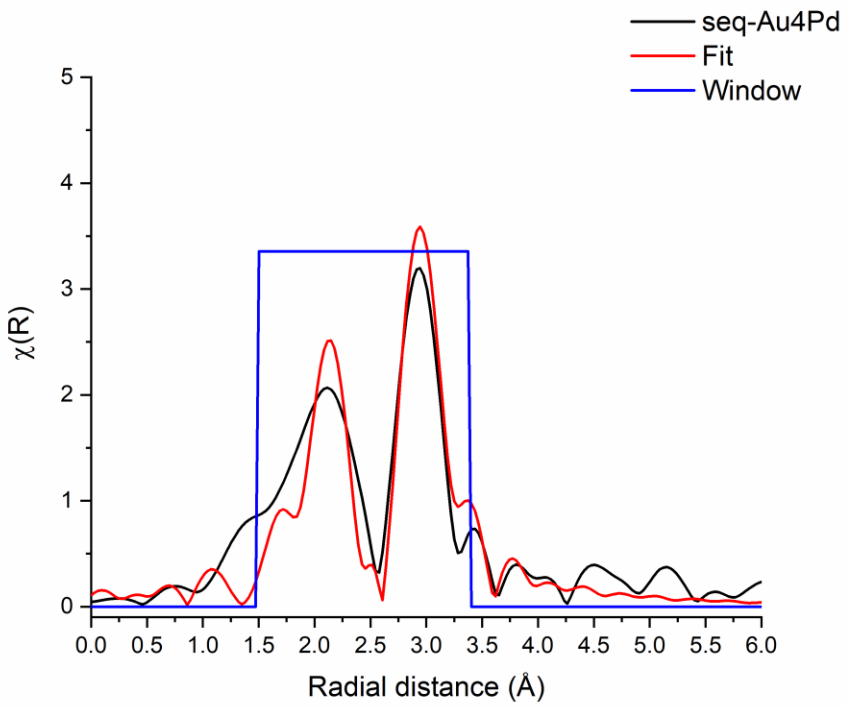

Figure A11. Pd K-edge EXAFS fit for seq-Au_4Pd.

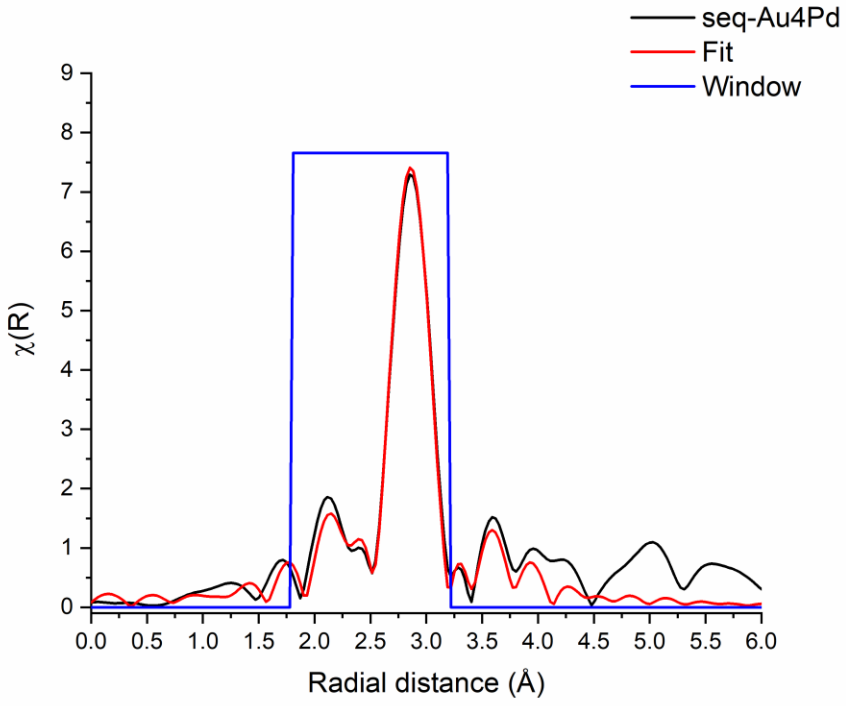

Figure A12. Au L_{III}-edge EXAFS fit for seq-Au_4Pd.

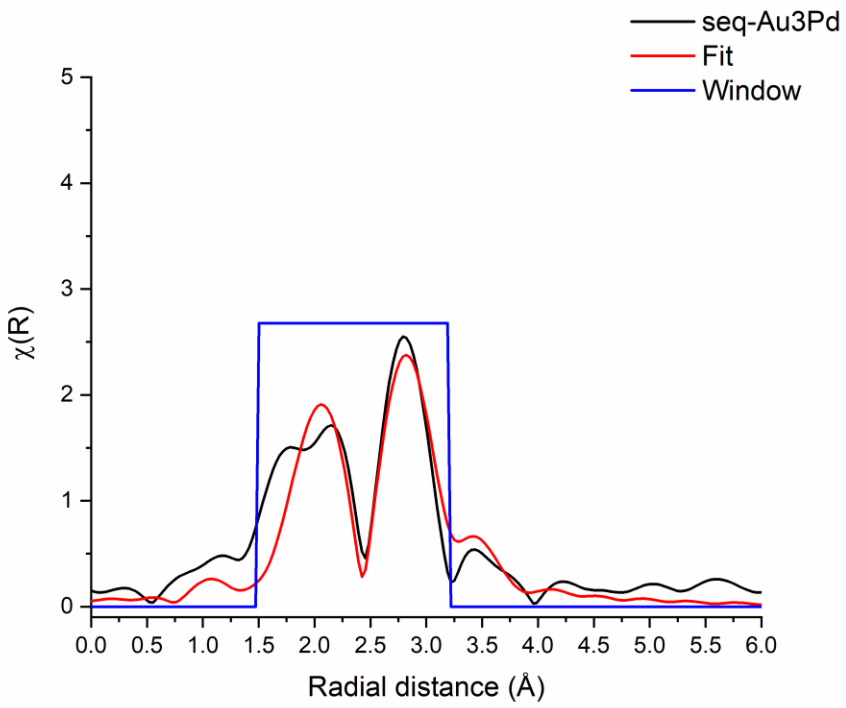

Figure A13. Pd K-edge EXAFS fit for seq-Au_3Pd.

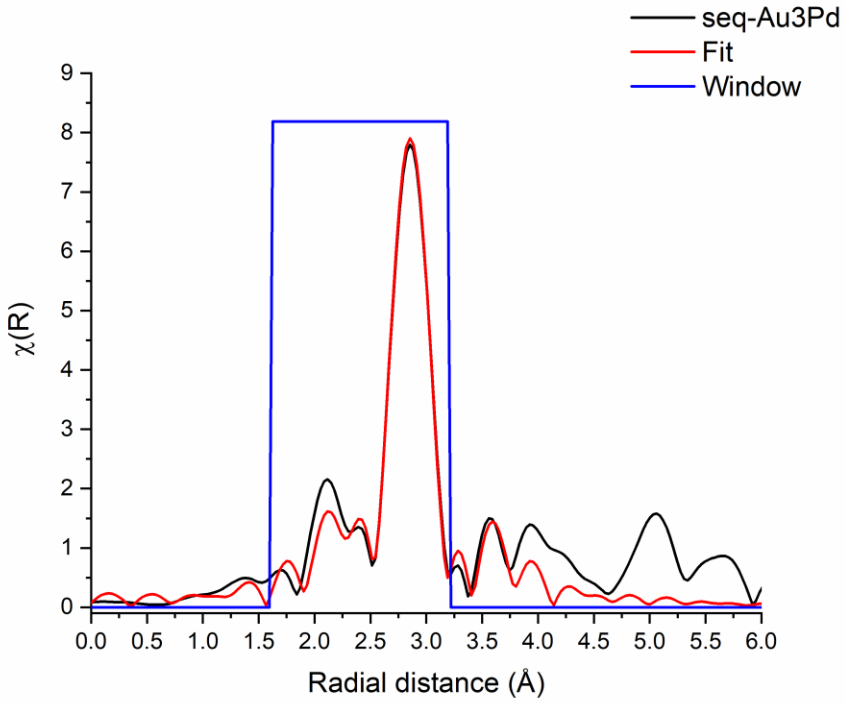

Figure A14. Au L_{III}-edge EXAFS fit for seq-Au_3Pd.

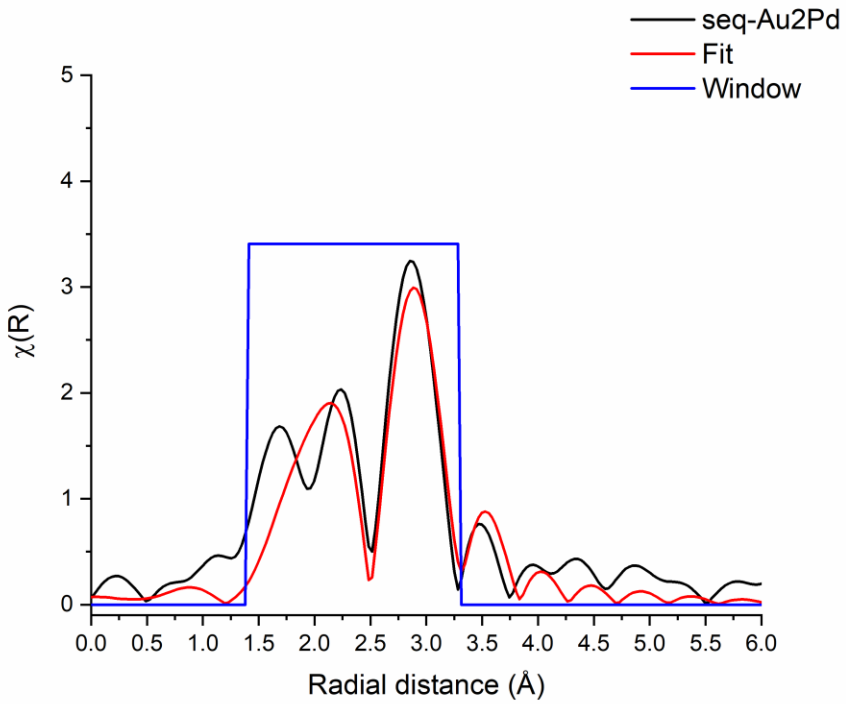

Figure A15. Pd K-edge EXAFS fit for seq-Au_2Pd.

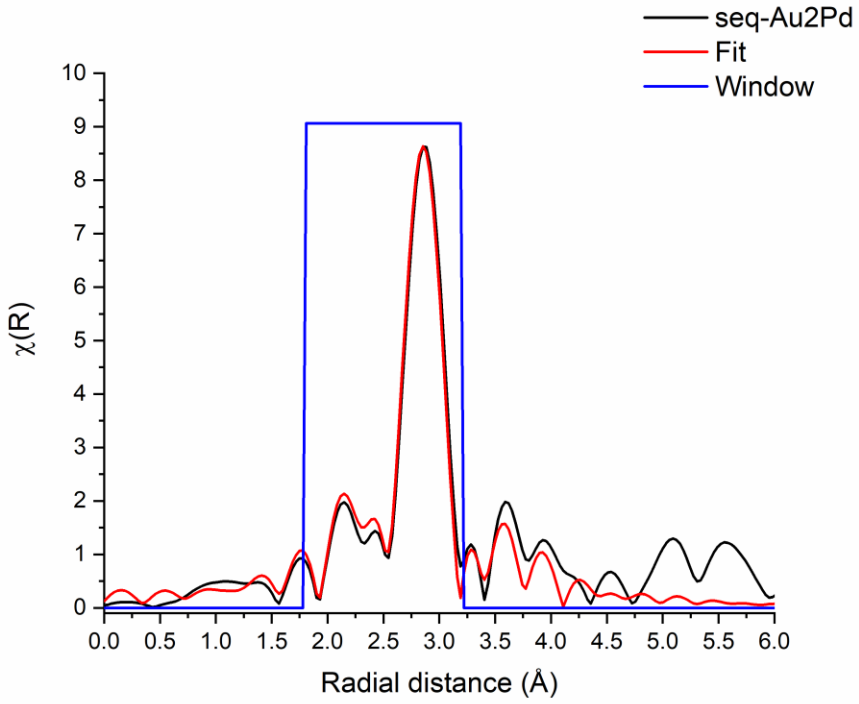

Figure A16. Au L_{III}-edge EXAFS fit for seq-Au_2Pd.

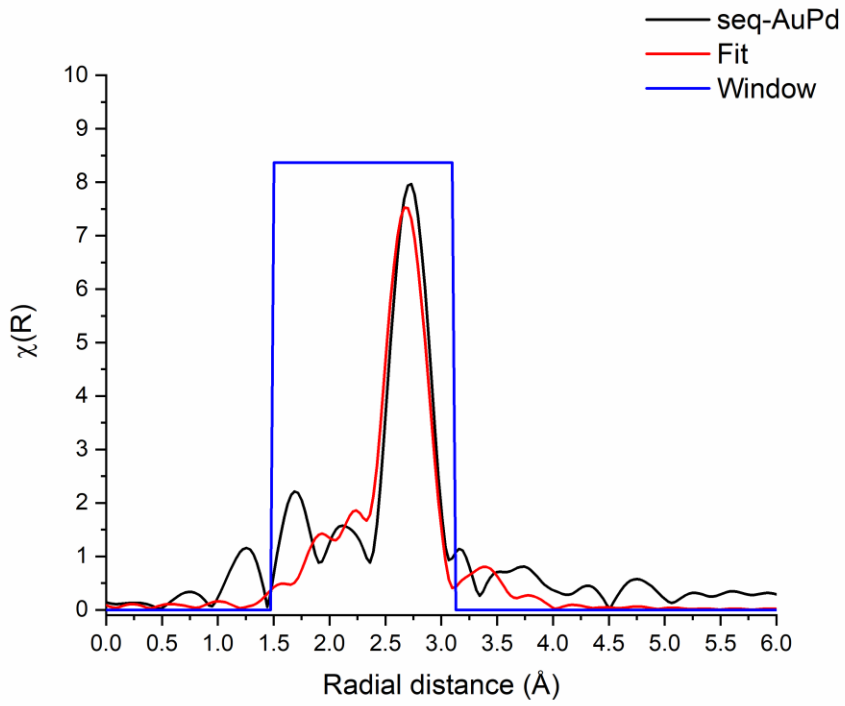

Figure A17. Pd K-edge EXAFS fit for seq-AuPd.

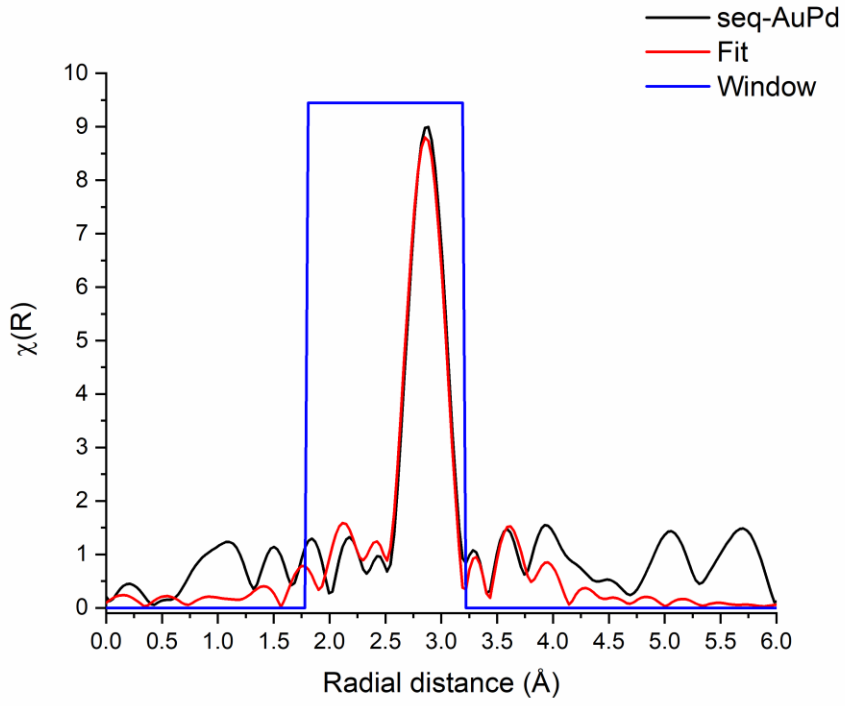

Figure A18. Au L_{III}-edge EXAFS fit for seq-AuPd.

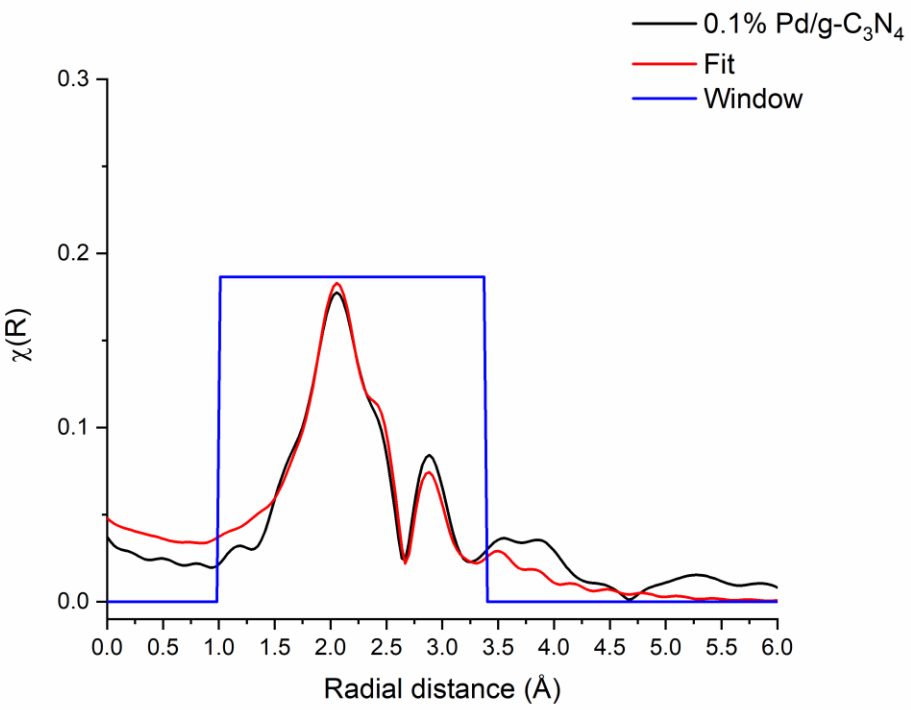

Figure A19. Pd K-edge EXAFS fit for 0.1% Pd/g-C_3N_4.

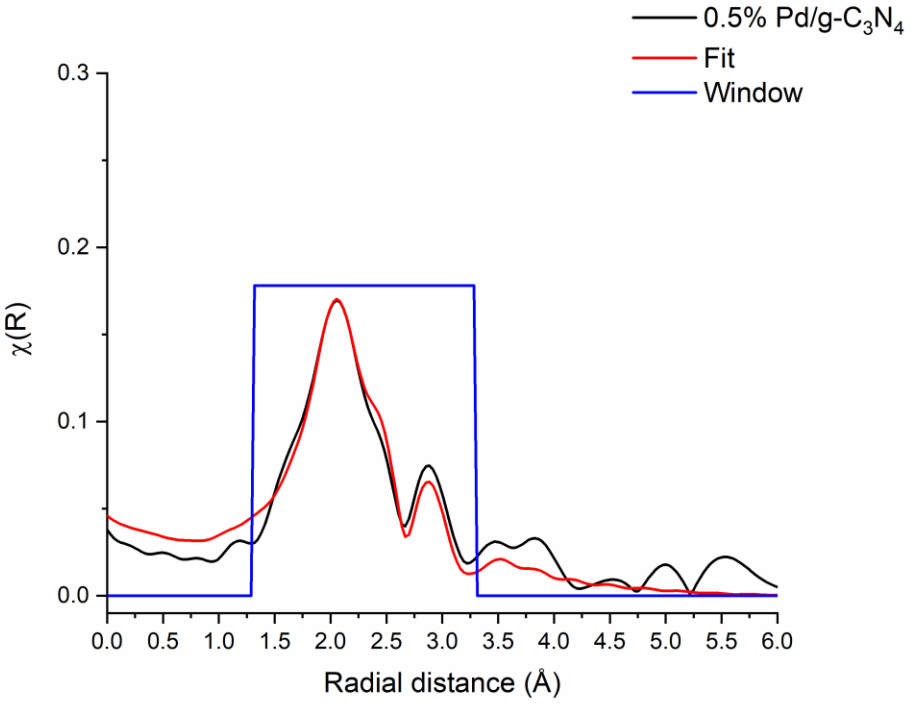

Figure A20. Pd K-edge EXAFS fit for 0.5% Pd/g-C_3N_4.

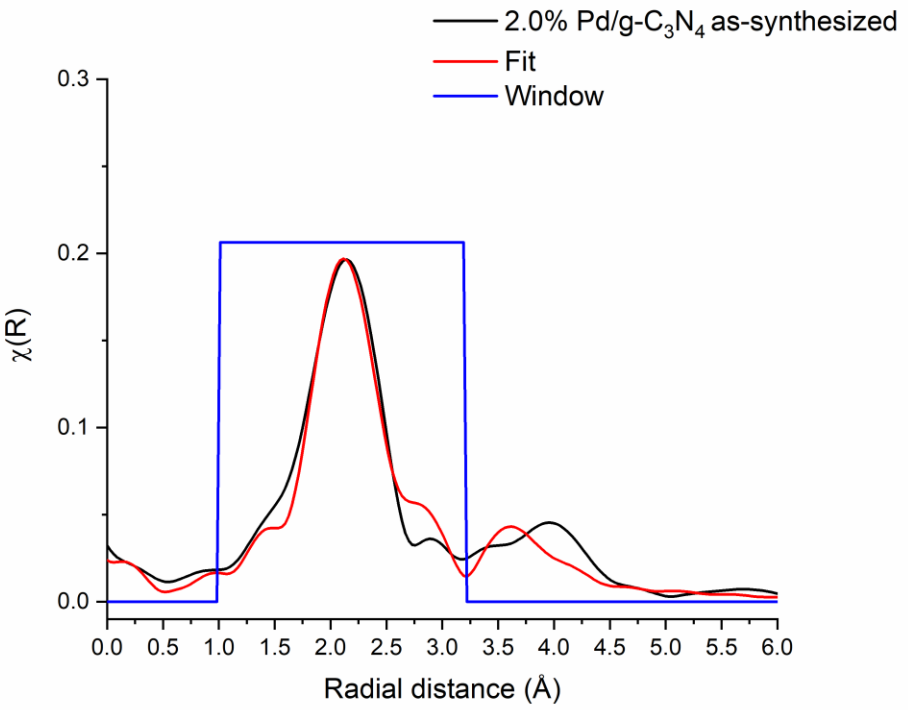

Figure A21. Pd K-edge EXAFS fit for 2.0% Pd/g-C_3N_4 as-synthesized.

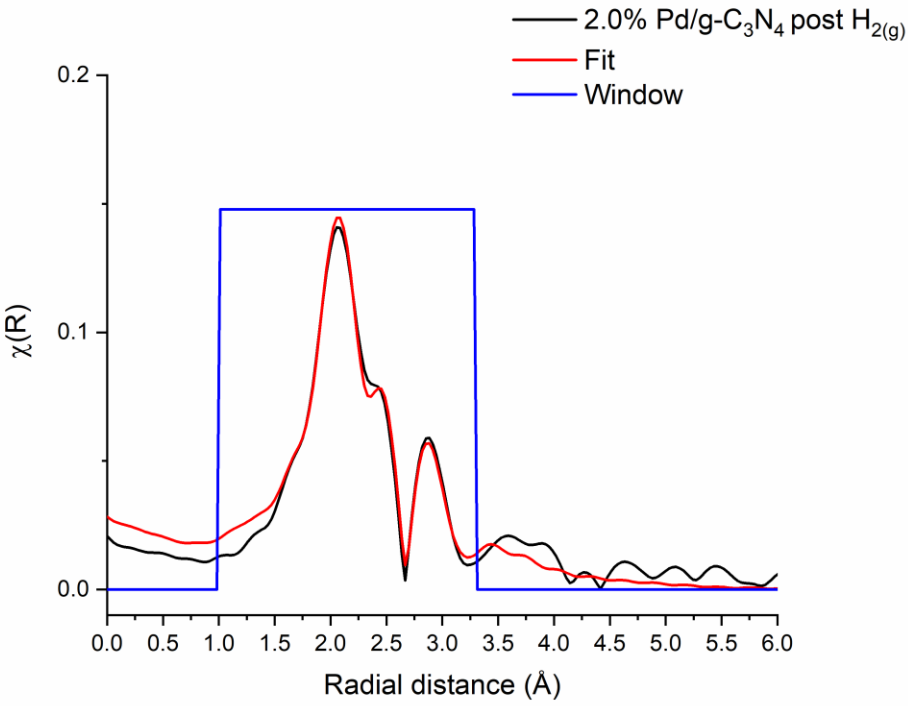

Figure A22. Pd K-edge EXAFS fit for 2.0% Pd/g-C_3N_4 post $H_{2(g)}$ treatment.

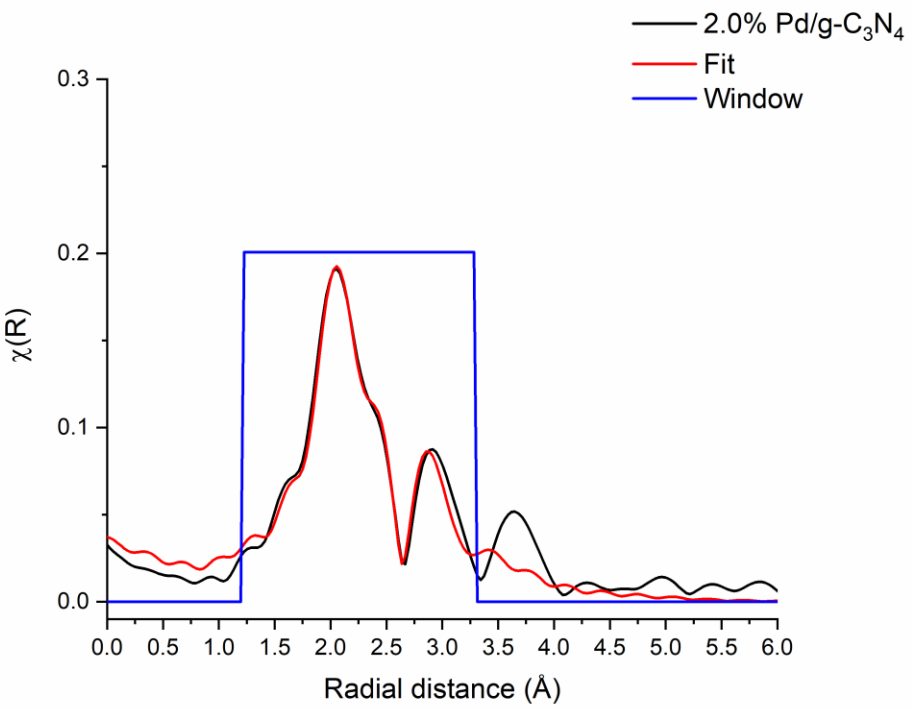

Figure A23. Pd K-edge EXAFS fit for 2.0% Pd/g-C_3N_4.